UNIVERSITÉ DU LUXEMBOURG

PhD-FSTC-2019-25
The Faculty of Sciences, Technology and Communication

DISSERTATION

Defence held on 27/03/2019 in Esch-sur-Alzette

to obtain the degree of

DOCTEUR DE L'UNIVERSITÉ DU LUXEMBOURG

EN PHYSIQUE

by

Shankari NADUPALLI
Born on 21 October 1989 in Hyderabad, India

STRESS – MODULATED BULK PHOTOVOLTAIC EFFECT IN POLAR OXIDE CRYSTALS

Dissertation defence committee:

Dr Torsten Granzow, Dissertation supervisor
Lead R&T Associate, Materials research and technology department, Luxembourg Institute of Science and Technology.

Dr Julia Glaum
Associate Professor, Faculty of Natural Sciences, Norwegian University of Science and Technology.

Dr Susanne Siebentritt, Chairman
Professor, Université du Luxembourg.

Dr Thomas Schmidt
Professor, Université du Luxembourg.

Dr Brahim Dkhil
Professor, CentraleSupélec, Paris.

Comité d'encadrement de thèse

(CET)

Supervisor	Dr. Torsten Granzow Ferroic Materials for Transducers unit Materials research and technology department Luxembourg Institute of Science and Technology.
CET member	Dr. Prof. Susanne Siebentritt Laboratory for Photovoltaics Faculty of Science, Technology and Communication University of Luxembourg.
CET member	Dr. Prof. Thomas Schmidt Faculty of Science, Technology and Communication University of Luxembourg.

Abstract

Light-induced phenomena in ferroelectric materials have been exploited for decades for optoelectronic applications. Homogeneous illumination of a non-centrosymmetric ferroelectric material creates anomalously high voltages exceeding a value which is usually limited by its band gap. This phenomenon is called the bulk-photovoltaic effect (BPVE). Lithium niobate is a prototypical material for BPVE. The only limiting factor in lithium niobate is its low photo-current values, which can be improved by doping the crystal with donor metals.

This study focuses primarily on light induced processes in mono-domain lithium niobate single crystals doped with transition metal ions, particularly the influence of stress on the BPVE. The effect of stress on BPVE is termed the piezo-photovoltaic effect (PPVE). This thesis report is framed to systemically introduce topics which cause, influence and aid in understanding the PPVE. Topics such as the symmetry in crystals, their physical properties, the intrinsic bulk photovoltaic effect (BPVE) are introduced in Chapter-1, where as the structure, defects, light-induced charge transport in donor doped lithium niobate and the reason behind the appearance of BPVE are discussed in Chapter-2. The techniques and experimental arrangements used in this work are detailed in Chapter-3.

A direct evidence of BPVE and the influence of stress is shown in Chapter-4. Transition metal doped lithium niobate crystals are oriented via x-ray diffraction (XRD) and a basic chemical characterization is undertaken using secondary ion mass spectrometry (SIMS) to identify dopant elements. Absorption spectroscopy in the UV/VIS/NIR range revealed windows in the spectra indicating photo-excitation of the donor doped ions. The absorption lines show that a shift in the fundamental band-edge occurs in lithium niobate for different dopant elements. Electron paramagnetic resonance (EPR) spectrometry is performed on the samples to confirm the location of the dopant ion in the crystal matrix by indicating its symmetry. The difference in the dopant concentration and the change in the oxidation state of the dopant ion under light illumination is obtained from EPR study. Direct measurements to obtain bulk photovoltaic current density in iron doped- lithium niobate single crystals are performed at increasing intensities at different wavelengths to determine the BPV coefficients. This study provides a quantitative analysis of different components of the BPV tensor values. The highest BPV component β_{333} is observed when iron doped lithium niobate is illuminated with

light of wavelength 450 nm. Obtained BPV tensor components are corroborated by the influence of the structural environment and the dipole interactions on charge transport mechanism of BPVE. The charge transport mechanism and the obtained values of the BPV tensor components are justified and discussed on the basis of the polaronic charge transport phenomena proposed by Schirmer et.al.[1] The influence of stress on BPVE is measured using a custom-designed set-up. The PPV components in lithium niobate are experimentally investigated for stress levels in the 1MPa - 10MPa range. A detailed discussion on the experimental observations are in Chapter-5.

The prime discovery of this thesis is the intrinsic character of the piezo-photovoltaic effect (PPVE), where increase in the light induced current is observed when the crystal is subjected to uniaxial compressive stress. The Young's modulus of lithium niobate is 202 GPa. Applying 10 MPa compressive stress translates to strain levels of just 50 ppm. 10 MPa of compressive stress along the polar axis of the crystal increased the short-circuit photo-current by 73%. When stress is applied perpendicular to the polar axis, about 370% increase in short-circuit photocurrent was observed with just 50 ppm of strain, which is a drastic for such moderate amounts of stress levels. This study proves the vitality of strain tuning to increase the PV properties in crystalline solar cells. Extrapolating the observed effect, PPVE is envisioned as a phenomenon which could be exploited in other polar oxide ceramics and thin-films where large photovoltaic energy generation can be made possible beating the existing limits.

Acknowledgment

I would like to thank my supervisor Dr. Torsten Granzow for his support, patience and teaching which was very much required to kick start my thesis and to continue it. His presence has been critical to the completion of this work. Thank you very much for proofreading it carefully to make it look like what it is today. Many thanks to Jens Kreisel for his helpful and uplifting discussions, for motivating the research and curiosity. I would also like to thank Dr. Susanne Siebentritt, who is an inspiration when it comes to research, team building and organization. Without you, the project wouldn't have been where it is now.

Thank you Mael Guennou for the much needed lecture sessions. Your support, help, small talk, input and your smile has definitely contributed positively to my being in general.

Thank you Emmanuel Defay for taking care when I needed the most and for bringing fun to the FMT group.

Thank you very much Mathieu Gerard and Olivier Bouton for creating the stress-cell, without which this thesis wouldn't have had new experiments.

I would also like to thank Germain Rey, Yves Fleming, Jerome Guillot and Frederic Addiego for the fruitful discussions and help with the analysis during the course. I frankly enjoyed the interactions. Thanks Nathalie Valle for taking time out even during really tough times to provide input for my thesis. Thanks to Emre Erdem for being kind to let me visit him at the University of Freiburg for EPR measurements. I would never forget the beautiful city.

Thank you my dear friends Alex, Cannon, Connie, Sara, Ingrid, Gaelle, Jan, David, Carlos, Peng, Charlotte, Mauro, Javier, Phillipp, Gael and Mads. Times I had spent with you have been memorable. Thank you Anais for lifting my spirits up when I was low with occasional small talk.

Last but not the least, I would like to thank the ever growing team of FMT for supporting me, caring to listen when I spoke and for being ready for spontaneous coffee/tea breaks. I would like to thank all the happy faces at LIST for sharing a pleasant smile when we bump into each other, it is these little things that make a lot of difference.

I would like to thank Marc Ney for preparing my mind to write, for being there when needed and for bringing me to what I am now.

Last but not the least, I thank my parents for making me what I am today and bearing with all my shenanigans. Thank you Amma, Dr. U Padmavathi for being a constant support and for showing me that service to humanity is greater than any achievement. Thank you Nanna N.V. Satyanarayana for being the hero of my life, for showing me the value in being humble and for all the conversations we had and yet to have about materials, chemistry, philosophy, cuisine and many many more things. Thank you Anna, for cooking delicious meals for me and for cheering me up during rough patches. Really, thank you very much for without you all, I would not be.

Table of Contents

List of Figures

List of Tables

Notations

α	Absorption coefficient
β_{ikl}	Bulk photovoltaic coefficient
χ_{ij}	Dielectric susceptibility tensor
ϵ	Permittivity of a dielectric material
ϵ_0	Permittivity of a vacuum
γ_{iklmn}	Piezo-photovoltaic coefficient
$\hbar$	Planks constant
λ	Wavelength
$\Lambda_{i,z}$	Mean transport length along c-axis
μ	Dipole moment
μ_e	Component of the mobility tensor
ω_o	Longitudinal optical phonon frequency
ϕ_{piezo}	Schottky barrier height due to the piezo charges
ϕ_{SB}	Schottky barrier
ρ_{piezo}	Density of the stress-induced piezo charges
σ_{33}	Stress along the c-axis
σ_d	Dark conductivity
σ_{ij}	Stress tensor
σ_{ph}	Photo conductivity
τ_n	Carrier lifetime
Υ_i	Transition probabilities
ε_k	Component of the light electric field

ϖ	Total absorption probability per unit time
$\widehat{\sigma}$	Conductivity tensor
Δn	Excess electron concentration
Δp	Excess hole concentration
Δt	Change in time
ΔT	Change in temperature
$\vec{\mathrm{M}}$	Matter tensor
$\vec{\mathbf{C}}$	Field tensor
$\widehat{D}$	Diffusion tensor
A	Area of electrodes
a	Distance between hopping sites
B_0	Magnetic field
C	Capacitance
c_S	Concentration of impurity in the crystal
D	Electric displacement
d	Inter-atomic distances
d_{33}	Piezoelectric constant along +c axis
d_{ijk}	Piezoelectric coefficient
E	Electric field intensity
E_{C}	Conduction band energy
E_{f}	Fermi energy
E_{V}	Valence band energy
E_{Fn}	Quasi Fermi level for electrons
E_g	Band gap energy
E_P	Energy of the phonon
E_{sdp}	Strain induced defect potential
G_L	Rate of photon generation
G_T	Thermal generation rate
I	Light Intensity

I_p	Pyroelectric current
j_{sc}	Short circuit current density
j_{s}	Saturation current density
j_{diff}	Diffusion current density
j_{drift}	Drift current density
j_{ph}	Total photovoltaic current density
j_{coh}	Coherent current density
J_i	Transfer integral
$j_{pv,i}$	Bulk photovoltaic current density
k_{B}	Boltzmann constant
k_{eff}	Effective distribution coefficient
L	Thickness of the crystal
l	Distance between electrodes
m_s	Electron spin
n_0	Initial concentration of electrons
P	Polarization
p_i	Pyroelectric coefficient
P_s	Spontaneous polarization
Q	Interaction coordinates
q	Elementary charge
q_{ef}	Quantum efficiency
r_{33}	Electro-optic coefficient
r_l	Transition dipole arm
S	Photon absorption cross section
T_c	Curie temperature
V	Voltage
V_{oc}	Open circuit voltage
V_{ph}	Photovoltage
V_f	Net force on the neighbouring atoms

W_k	Probability of electron transition
W_{piezo}	Width of the piezo-polar charge

Abbreviations

RT	Room temperature
PV	Photovoltaic
BPVE	Bulk photovoltaic effect
DSSC	Dye sensitized solar cells
PPVE	Piezo photovoltaic effect
LN	Lithium Niobate
TM	Transition metal
SCR	Space charge region
APV	Anomalous photovoltaic effect
UV	Ultra violet
SB	Schottky barrier
EO	Electro optic
TO	Transverse optical
LO	Longitudinal optical
LS	Low spin
HS	High spin
IR	Infra red
SIMS	Secondary ion mass spectroscopy
EPR	Electron paramagnetic spectroscopy
XRD	X-ray diffraction

Part I

Fundamentals

Chapter 1

Crystals and their properties

A solid in which the constituent atoms or ions are ordered in a regular manner with a repeating pattern extending in all three spatial dimensions is called a crystal. The study of crystals governing the state, arrangement of atoms, physical and chemical properties, their synthesis and growth is called "crystallography".[2] Crystallography is a subject which is vital in vast varieties of subjects starting from mineralogy, geology, geophysics to organic and physical chemistry, material science, biology and medicine.

Many types of crystals are found in nature. Snowflakes and common salt are well known examples. Various metals extracted from raw minerals, result in crystalline structures. Notable minerals which have crystalline structures are used as gemstones for their aesthetic appeal, for example corundum (ruby), emerald etc.. Quartz is an extremely common mineral, because it is simply silicon and oxygen, which are two most common elements in the crust. Today, crystals are used for different applications in science to make oscillators that provide a stable timing signal for wrist-watches and digital integrated circuits, to stabilise radio transmitter frequencies, manufacturing of capacitors, insulation for high-voltage electrical equipments, in solid state lasers, and depending on the hardness, they are used for cutting, polishing, grinding and engraving tools. Better understanding of the existing minerals and crystals through crystallography, enabled manufacturing of synthetic artificial crystals targeted for specific application.

The structure and symmetry of the crystals is an essential factor which provides information about the properties such as, the electronic band structure and optical properties. Crystal structure is comprised of atoms which are symmetrically arranged, which can be discussed in terms of a unit cell. The unit cell is periodically repeated in three dimensions forming a "Bravais lattice". The angles and distances between the lattice points of a unit cell are called lattice parameters (with distances a, b and c and angles α, β and γ).

1.1 Symmetry

Crystal structures are grouped according to their axial system describing the lattice, termed crystal classes. Crystal classes are termed analogous to the relation between their lattice parameters. For a Cubic crystal class, the distances between the lattice points is a = b = c and the relation between their angles is $\alpha = \beta = \gamma = 90°$. Similarly for orthorhombic crystal class, a ≠ b ≠ c and $\alpha = \beta = \gamma = 90°$ and for hexagonal crystal class, a = b ≠ c and $\alpha = \beta = 90°, \gamma = 120°$. These rules of crystal classes are very popular and are available in almost every fundamental material physics text books.[3–5]

Crystals are classified based on the symmetry. A crystal (a) must have translational symmetry, (b) may have a mirror symmetry and (c) may have rotational symmetry. A combination of translational, mirror and rotational symmetries are also observed in arrangement of atoms, which is termed (d) compound symmetry. In a crystal, a set of atoms are related by one part to another by an operation (translational symmetry operation, mirror symmetry operation and rotational symmetry operation), which act on all of space. An object or a space possess symmetry when there is an operation (or a set of operations) that maps it into congruence with itself.[6]

The point group of symmetry of a crystal is a collection of operations which can be represented by symmetry elements. Hermann and Mauguin provided a notation to the symmetry elements. The meaning, symbol and the total symmetry elements are given in the table 1.1.

Symmetry operation	Hermann-Mauguin symbol	Total
Mirror plane	m or $\bar{2}$	1
Centre of symmetry	$\bar{1}$	1
Rotation axis	1,2,3,4,6	5
Rotary inversion	$\bar{3}$, $\bar{4}$, $\bar{6}$	3

Table 1.1: Hermann-Mauguin notation for symmetry operations.

The number, adjacent to the rotation axis in the table 1.1 provides information about number of rotations possible for a given symmetry (n-fold rotation for n =1,2,3,4 & 6), here a bar on the number representing rotation axes represents roto-inversion ($\bar{n}$). The groupings of these 10 symmetry elements, give 32 combinations. The 32 combinations of these symmetry elements are called points groups of symmetry. Thus, crystal symmetry can be represented by a point group. For ease, these 32 point group symmetries, can be regrouped into 7 different sets each having one common symmetry element. The seven different sets are given in the table 1.2.

Name of the set	Common symmetry	Point-group
Triclinic	1 onefold rotation axis	1, $\bar{1}$
Monoclinic	1 twofold rotation axis	2, m, 2/m
Orthorhombic	3 twofold rotation axis $\perp$ to one another	222, 2mm, 2/m 2/m 2/m
Rhombohedral	1 threefold rotation axis	3, $\bar{3}$, 3m, $\bar{3}$m, 32
Tetragonal	1 fourfold rotation axis	4, $\bar{4}$, 4/m, 422, 4mm, 4/m 2/m 2/m, $\bar{4}$2m
Hexagonal	1 sixfold rotation axis	6, $\bar{6}$, 6/m, 6mm, 622, $\bar{6}$2m, 6/m 2/m 2/m
Cubic	4 threefold rotation axis	23, 2/m $\bar{3}$, $\bar{4}$3m, 432, 4/m $\bar{3}$ 2/m

Table 1.2: 32 classes of point group symmetries.

1.1.1 Introduction to tensors

The physical properties of a crystalline material depend on the composition, symmetry and orientation of the sample with respect to a defined coordinate axis. In this section, the tensor operator method that uses symmetry for treating such properties is given.

The effect of an action on a crystal results in a reaction. The action on a crystal for example could be an applied electric field. This basic concept can be shown as:

$$\vec{\mathbf{E}} = \vec{\mathrm{M}}\vec{\mathbf{C}} \tag{1.1}$$

where $\vec{\mathbf{C}}$ is a tensor representing the physical cause and $\vec{\mathbf{E}}$ is a tensor representing the effect. These are called 'field tensors'. The 'matter tensor ' $\vec{\mathbf{M}}$ constitutes the physical structure of the crystal and its symmetry. This determines if the the crystal is effected by the cause.[7]

A fundamental postulate of crystal physics which relates the structural symmetry to the properties is given by Neumann, which is known as Neumann's principle. It is stated as "*the symmetry of a physical property of a crystal must include the same spatial symmetry characteristics as the crystal structure and thus the symmetry of the matter tensor must include all of the symmetry operations contained in the point group of the crystal*".[7]

1.2 Classification of crystals

The point group of a crystal is the group of macroscopic symmetry elements that its structure possess. This is the basis for the division of crystals into 32 classes. It is important to notice that Neumann's principle does not state that the symmetry elements of a physical property are the same as those of a point group. It merely says that the symmetry elements of a physical property must include those of a point group. [8]

A physical property of a crystal consists of a relation between certain measurable quantities associated with the crystal. When a crystal has symmetry, however, the number of independent components of a tensor representing a physical property is reduced.

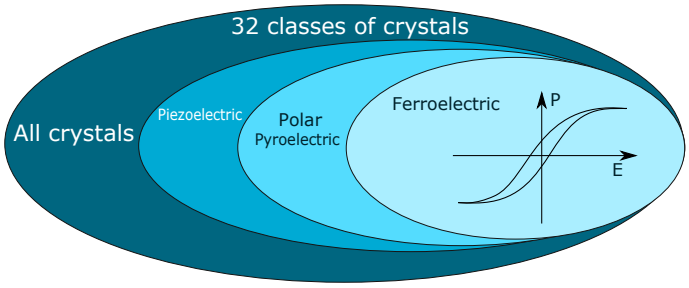

Figure 1.1: Classification of crystallographic point groups by electrical property.

Among 32 crystallographic point groups describing all crystalline systems shown in Fig.1.1:

- 11 are centrosymmetric and contain an inversion centre. In these point groups, polar properties do not exist due to an inversion symmetry. Any polar vector would be cancelled during the symmetry transformation.

- 21 point groups without a centre of inversion can exhibit piezoelectricity (with an exception of one).

- There are 10 point groups with a unique polar axis. This class of crystals show a spontaneous polarization parallel to the polarization axis. These crystals show a pyroelectric effect.

- Ferroelectric crystals belong to this group of materials, but exhibit a polarization reversal when a field is applied. This leads to a hysteresis with a remnant polarization. Hence ferroelectric crystals are pyroelectric crystals that exhibit reversible polarization.

1.3 Crystal properties

1.3.1 Dipole moment and polarization

If two discrete charged particles of opposite charges are separated by a certain distance, a dipole moment arises, which is represented as μ shown in 1.2a.

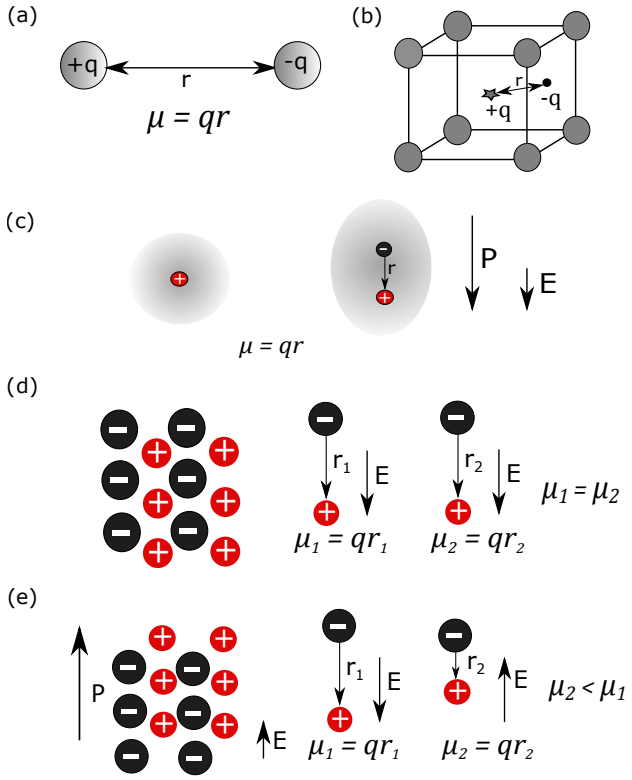

Figure 1.2: Dipole moment and polarization. (a) Appearance of a dipole moment by two discrete particles of opposite charges (b) Dipole moment in a crystal lattice with eight cations and an anion (c) Appearance of a dipole moment in an electron cloud when a field is applied (d) Ordered ionic structure with a combination of anions and cations with a pre-existing dipole moment (net polarization = 0) (e) Change in the dipole moment due to the application of an electric field in an periodic ionic structure.

A dipole moment could be understood as charges belonging an electron cloud that surrounds the nucleus of an atom. Dipole moment could exist across a large area containing many charges to find the net dipolar moment of a material. For example, in Fig.1.2b centre of negative charge is located some distance away from the anion (depicted as the star). Dipole moment is a vector, since r is a vector (r points from −q to +q). Hence, polarization is the net dipole moment per unit volume. When dipole moments in a material cancel out each other, the polarization is zero.

The polarization here is:

$$P = \frac{\text{Vector sum of the dipole moment}}{\text{Volume of the sample}} \tag{1.2}$$

The mechanism of electronic polarization could be understood as follows: In each ion, a positive charged nucleus with a negatively charged electron cloud exists. When an electric field is applied, the electron cloud distorts and the positive charge moves in the opposite direction. Since the electron cloud doesn't have the centred positive charge, a dipole moment arises as shown in figure 1.2c.

In the Fig.1.2d, a typical ionic structure, with a combination of cations and anions of equal and opposite charges is held together by an ionic bond. An ion pair already possess a dipole moment, before application of an electric field. The net polarization may still be zero. With application of an electric field to a material that already possess a spontaneous polarization, the polarization increases by increasing the magnitude of individual dipole moments, as shown in Fig.1.2d. When the applied field is reversed as in Fig.1.2e it causes a compression of the bond decreasing the dipole moment. The electric field leads to an off-centring of the cations with respect to the anions and vice versa. This causes a distortion of the bonds. Hence, the centres of positive an negative charge no longer coincide and a net polarization develops.

1.3.2 Dielectric property

Dielectric properties of a material depends on the frequency of electric field and conforms to the symmetry of the material. The polarisation of a crystal produced by an electric field is an example of an anisotropic crystal property that is represented by a second rank tensor. The electric polarization can be explained by a relation between the electric field intensity (E) polarisation (P) and electric displacement (D).

$$D = \epsilon_0 E + P \tag{1.3}$$

where ϵ_0 is a scalar constant, the permittivity of a vacuum $\epsilon_0 = 8.854 \times 10^{-12} C V^{-1} m^{-1}$
In an anisotropic substance,

$$P_i = \epsilon_0 \chi_{ij} E_j \tag{1.4}$$

where, χ_{ij} is the dielectric susceptibility tensor.

The dielectric constant is a measure of a dielectric material on a capacitor. So it is typically a ratio of the capacitance of a capacitor with a dielectric and the empty capacitor. The dielectric constant even relates to the permittivity of the material. Permittivity is a quantity that describes the effect of a material on an electric field.[8]

$$\text{The dielectric constant } (K) = \frac{\text{Capacitance of a dielectric material}}{\text{Capacitance of an empty capacitor}} = \frac{\epsilon}{\epsilon_0} \tag{1.5}$$

Dielectric constant is sometimes also called relative permittivity, which is the ratio of permittivity of a dielectric material and the permittivity of vacuum.

$$\text{Relative permittivity} = \frac{\text{Permittivity of a dielectric}}{\text{Permittivity of vacuum}} \tag{1.6}$$

1.3.3 Piezoelectric property

All crystalline materials belonging to a symmetry group that does not include a centre of inversion, except those in point group 432, generally display some degree of piezoelectricity. They develop an electric polarization when submitted to mechanical stress or react with a mechanical strain to an external electric field applied in a certain direction. This effect is put to practical use in many applications such as piezoelectric sensors and actuators or ultrasonic emitters and receivers. Ferroelectric perovskite-structured materials are most commonly employed for such applications. Among these, lead zirconium titanate (PZT) is predominant, while barium titanate ($BaTiO_3$) is a common model material.

A state of stress is specified by a second-rank tensor with nine components. Since the polarization of a crystal is a vector, the piezoelectric coefficient is specified by three components. When stress σ_{ij} acts on a piezoelectric crystal, each component of the polarization P_i is linearly related to all the components of σ_{ij}.[8]

In terms of tensors,

$$P_i = d_{ijk}\sigma_{jk} \tag{1.7}$$

where, d_{ijk} is the piezoelectric coefficient.

Piezoelectric tensor conforms to the symmetry of the crystal. Components of the piezoelectric tensor are discussed in appendix A

1.3.4 Pyroelectric property

Of 20 piezoelectric crystal classes, 10 have a unique polar axis. Such crystals are termed polar since they possess spontaneous polarization or an electric moment per unit volume. This spontaneous polarization cannot be detected by the charges on the surface, since the depolarizing field resulting from charge distribution is compensated by the

flow of free charge within the crystal. However, this spontaneous polarization is temperature dependent and its existence could be detected by observing the flow of charge to and from the surfaces with a change in temperature. The 10 polar classes of crystals exhibit the property of developing a change in electric polarization when their temperature is changed which is called the pyroelectric effect.

A change in temperature ΔT results a change in the polarization vector ΔP_i. This is given by,

$$\Delta P_i = p_i \Delta T \tag{1.8}$$

where, p_i is the pyroelectric coefficient.

The pyroelectric coefficient p can be calculated using the relationship:

$$p_i = \frac{\frac{I_p}{A}}{\frac{\Delta T}{\Delta t}} \tag{1.9}$$

where I_p is the pyroelectric current, A is the area of electrodes, $\frac{\Delta T}{\Delta t}$ is the rate of change in temperature.

1.3.5 Ferroelectric property

The defining property of ferroelectrics is a reversible spontaneous electric polarization whose magnitude and direction can be sensitively tuned by varying temperature, electric field, strain or chemical composition.[9,10] A typical ferroelectric possessing a spontaneous polarization P_s decreases with increasing temperature T to disappear at a Curie temperature T_c. What makes ferroelectrics interesting is the effect of electric polarization on other properties. For instance,

1. Ferroelectric – ferroelastic materials present a coupling between electric polarization and mechanical deformation, which can lead to a remarkable piezoelectric response with numerous applications such as, actuators and sensors.
2. Ferroelectric – ferroelastic – magnetic materials, which are termed multiferroics, which present interesting coupling phenomena with high potential for electronic and spintronic applications.
3. Ferroelectric materials which exhibit electro-optic properties due to interaction with light due to photo-sensitivity. Such materials introduced a field that is termed photo-ferroelectrics, which was studied extensively, but has been largely overlooked and is now deserving of renewed attention.[11]

1.4 The photovoltaic effect

The process of converting light to electricity is called the photovoltaic effect (PV effect). The photovoltaic cell consists of a light absorbing material which is connected to an external circuit. The absorption of photons leads to charge carrier generation in the material. These carriers are driven towards a contact. When the resultant charge carriers are separated by an intrinsic barrier, it produces a photovoltage in open circuit conditions, and generates a photocurrent in short circuit conditions. When a load is connected to the external circuit, the cell produces both current and voltage.[12]

The PV phenomenon is initially observed in semi-conducting materials like silicon and germanium. A great amount of research led to understanding the mechanism of charge transport and improving the efficiency of converting light to electrical energy.

The photovoltaic phenomenon in ferroelectric materials such as $BaTiO_3$, $LiNbO_3$, $KNbO_3$ was reported much later. Like in the case of semiconductors, there is generation of photovoltaic current and voltage in ferroelectric materials. But the mechanism of charge generation, transport and recombination in ferroelectric materials is different from that of semiconductors.

1.4.1 PV effect in Semiconductors

Semiconductor materials used for PV energy generation vary from silicon, polycrystalline thin films or single-crystalline thin films.

The PV effect in semiconductors occurs due to a pn junction. A pn junction is created by doping one region with acceptor impurities (p-type region) and the other with donor impurities (n type region) in a single crystalline material. To gain equilibrium, electrons from the n-type donor region try to diffuse into the p-type acceptor region and vice versa. This diffusion process creates a space charge region (SCR) which can be thought of as a mini capacitor with an electric potential V_b. The electric potential opposes any further diffusion. This is depicted in Fig (1.3)a.

The charge transport can be visualised using a band diagram depicting the energy levels for both acceptor and donor regions. For a zero bias voltage, the band diagram in equilibrium conditions is shown in Fig (1.3)b. Here the conduction E_C and the valence bands E_V bend along the SCR. Here the Fermi level E_f exists in between the valance and the conduction bands.

Under illumination with photon energies higher than the band gap, electrons are generated in the n-type region and holes in the p-type region, as shown in Fig (1.3)c. The Fermi level is split into a quasi Fermi level for holes E_{fh} and for electrons E_{fe}. Due to illumination, the intrinsic Fermi level E_f bends at the SCR. The excess amount of electrons and holes diffuse through the SCR. The formed electron hole pairs recombine resulting in photovoltaic currents.

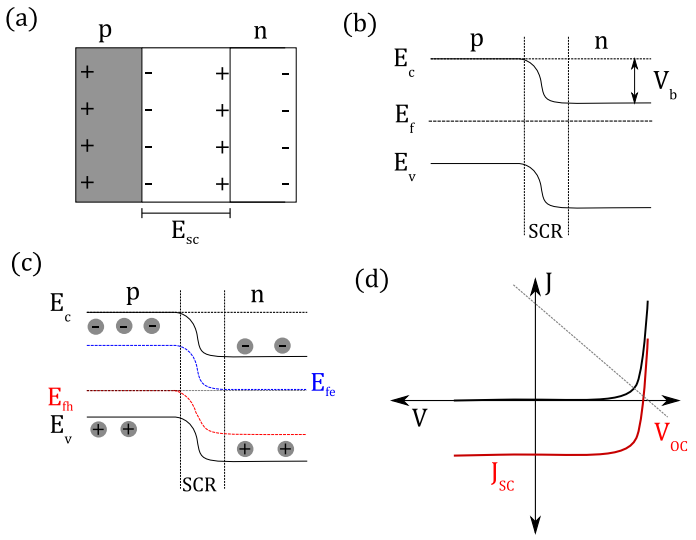

Figure 1.3: A typical pn junction forming a space charge region and its equivalent band diagram. (a) A typical n-type and p-type interface with a space charge region. Diffusion of charge carriers between these regions, and its electric potential V_b. (b) A typical band diagram at equilibrium conditions showing Fermi energy level E_f (c) Under illumination, generation of quasi Fermi levels for holes E_{fh} and electrons E_{fe} for short circuit condition (d) j-V characteristics of the pn-junction.

The current-voltage (j-V) characteristics in Fig 1.3d for non-illuminated pn junction can be expressed by the equation.

$$j_{dark} = j_s \left[exp\left(\frac{qV}{k_B T}\right) - 1 \right] \tag{1.10}$$

Where,

j_s	Saturation current density
q	Elementary charge
k_B	Boltzmann constant
T	Temperature
V	Applied voltage

The I-V characteristics for an illuminated pn-junction is given by:

$$j_{illum} = j_{dark} - j_{ph} \tag{1.11}$$

Where,

j_{ph}	photovoltaic current

1.4.2 Bulk photovoltaic property

The photovoltaic phenomenon in ferroelectric materials is different from that observed in typical pn junction semiconductors. In ferroelectrics a single material is responsible for generation of electron-hole pairs, their separation and recombination. It is important to notice that the efficiency of light to electricity conversion in bulk ferroelectric materials is in no way close to a conventional pn junction solar cells. Most of the ferroelectric materials studied so far for photovoltaic applications have wide band gap which restrain them from visible light absorption. A method to overcome this factor is by doping ferroelectric materials with transition metal ions to enable visible light absorption.

The photovoltaic effect in ferroelectric materials was first reported in single crystals of $BaTiO_3$ below the Curie temperature by Chynoweth in 1955.[13] When illuminated and under short-circuit conditions a constant current was observed. Also, the open circuit voltage exceeded the band gap energy by several orders. This PV effect in ferroelectrics was observed in a variety of single crystalline ferroelectrics[11,14] which do not have any gradient in the concentration of charge carriers. This new PV effect was observed in completely homogeneous ferroelectric single crystalline materials,[15] which contrasts the PV phenomenon in semiconductors (even if it is single crystalline) where illuminating the area with inhomogeneity of excess and deficient charge carries (the pn-junction) leads to a PV effect. One of such important factors which mark the difference of PV effect in ferroelectrics and semiconductors is, in semiconducting materials, the magnitude of open circuit voltage (V_{oc}) cannot exceed the band gap of the material. In ferroelectric materials, the values of open circuit voltage (V_{oc}) exceed the band gap of the material by several orders of magnitude. This huge effect was termed differently by different observers calling it the the anomalous photovoltaic (APV) effect, or photo-galvanic effect,[16,17] or the bulk photovoltaic effect (BPVE).[1] For the sake of consistency, this effect will be called the bulk photovoltaic effect (BPVE) in this thesis.

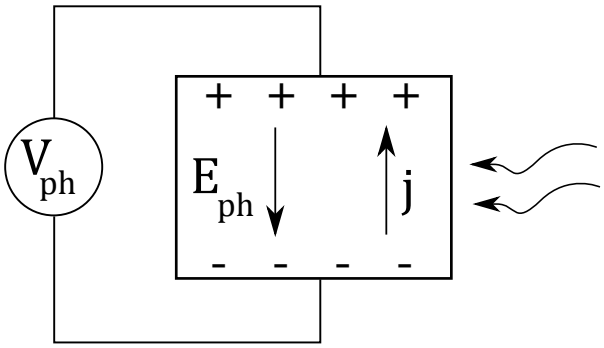

Figure 1.4: Photovoltage V_{ph} generation due to illumination of a crystal under short circuit conditions with a recorded photo current j and a corresponding field E_{ph}. Redrawn from Fridkin V.M (2001)[18]

When crystals are exposed to light with a wavelength in the absorbable range, it gives photo-current and photovoltages. Under short-circuit conditions, short circuit photo

current is generated j_{sc} and under open circuit condition, a photovoltage V_{oc} is generated as shown in Fig (1.4).[15]

Phenomenon of BPVE The photovoltage observed in BPVE can be expressed by the following equation. Here the current j_i generates a photovoltage as,

$$V_{\text{ph}} = \frac{j_i l}{\sigma_d + \sigma_{ph}} \tag{1.12}$$

Where,

σ_d	dark conductivity
σ_{ph}	photo conductivity
l	distance between electrodes

A high voltage is generated if both dark conductivity and photo-conductivity are low. The photovoltage generated is proportional to the distance l between the electrodes. V_{ph} is not limited by the band gap.[15]

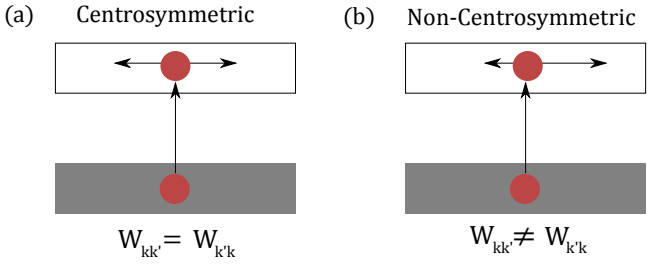

Figure 1.5: Distribution of charge carriers in centro and non-centrosymmetric media. (a) Symmetric distribution of momentum of charge carriers in a centrosymmetric crystal (b) Asymmetric distribution of non-thermalized charge carriers and their momentum in a non-centrosymmetric crystal. Redrawn from Fridkin V.M (2001)[18]

The symmetry of the crystal determines the electronic transitions. Usually in crystals with inversion symmetry, the probability of electron transition and reverse transition is equal to each other which is balanced. BPVE arises when this electron transition and reverse transition are not equal to one other causing an imbalance. When the probability ω of electron transition from the momentum state k to k' is equal to the probability of electronic transition from a state with momentum k' to k which is the reverse transition of the former, the transition is balanced. This can be written as $W_{kk'} = W_{k'k}$ shown in Fig (1.5).[18]

Crystals like germanium and silicon exhibit conventional PV effect and are centrosymmetric crystals, hence, situation of balanced transition occurs.

"*In non-centrosymmetric crystals, $W_{kk'} \neq W_{k'k}$. Here, the violation of this balancing gives rise to an asymmetric momentum distribution for non-equilibrium electrons (or holes),*

which results in the appearance of the photovoltaic current in homogeneously illuminated crystals ".[18]

The asymmetry of the electronic processes can be explained by a particle which is elastically scattered in a media which lacks a centre of symmetry (non-centrosymmetry). The asymmetry of scattering is depicted in Fig 1.6(a) pictorially by showing the elastic scattering of a particle in a wedge shaped potential. It is possible that non-thermalized photo excited electrons travelling in the conduction band with momentum k and $-k$ are scattered differently by scattering centres in the structure, such as local dipoles forming the spontaneous ferroelectric polarization, Fig 1.6(a).[18]

The process of electron excitation itself can be asymmetric, depicted in Fig 1.6(b). The process of photo-ionization in this case depends on the environment of the centre releasing an electron under illumination, it is more possible to excite an electron with momentum k than $-k$.[18]

Fig (1.6)c depicts that there is possibility that electrons do not travel in the conduction band, but by hopping from one centre to another. So different probabilities for transitions in different directions are caused by asymmetric distances to the next available centre. Figure (1.6)d, shows ionic relaxation, this case involves exciting an ion from a trap, which leaves behind an ionized trap. There is a possibility that minor changes in the polarisation are observed in the measurement as electric current. This change in polarization could be due to the ion relaxing in the crystal lattice.[18]

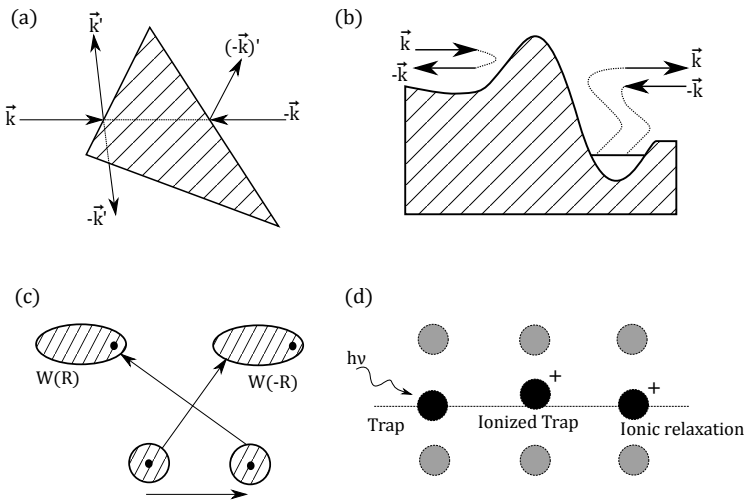

Figure 1.6: Phenomenon of BPVE. (a) Scattering of carriers from asymmetric centres (b) Excitation of defect/impurity centres with an asymmetric potential (c) Hopping mechanism between asymmetrically distributed centres and (d) Ionic relaxation. Redrawn from Fridkin V.M (2001)[18]

In a non-centrosymmetric crystal, the elementary processes like photo-excitation, scattering and relaxation occur with different probabilities. Meaning, the probability of elec-

trons moving in one direction versus the opposite direction are not equal to each other. A closer look into the phenomenon of electron excitation and recombination in such non-centrosymmetric media is discussed above with respect to the Fig (1.6).

If W_k^e is the probability of an electron excited from an impurity centre to the conduction band and W_k^r is the probability of the electron recombining from the conduction band back to the impurity level, then the asymmetry in this process can be seen as:

$$W_k^{e,r} \neq W_{-k}^{e,r} \tag{1.13}$$

Since the recombination processes of charge carriers are different from the excitation, the recombination process would not simply emit a phonon or a photon but progress in other ways. The presence of trap levels just below the conduction band which can trap carriers would change the recombination process. The electron can be excited and recaptured at this trap level. It is due to such trap levels right below the conduction band that make the recombination process different from that of the reverse generation process.[17,19]

For BPVE effect to occur, the two primary requirements are:

1. non-centro symmetric materials which can generate carriers in an asymmetric manner, and
2. the presence of trap levels.

BPVE in non-centrosymmetric media for linearly polarized light electric field, can be described by the following equation:

$$j_{pv,i} = \beta_{ikl}\varepsilon_k\varepsilon_l^* I \tag{1.14}$$

Where,

$j_{pv,i}$	Bulk photovoltaic current density
β_{ikl}	Bulk photovoltaic tensor (third rank tensor)
ε_k	Component of the light electric field
ε_l^*	Complex conjugate of the light electric field
I	Light intensity

The third rank bulk photovoltaic tensor which is given by β_{ikl} determines if current generation exists in a particular direction. ε_k and ε_l are projections of electric field of the linearly polarized light with respect to the plane of measurement. It is obvious from the equation (1.14) current isn't exclusively generated along the polar axis, but also in other directions which would be determined by the bulk photovoltaic tensor β_{ikl}.

1.4.3 Extrinsic effect of stress on BPVE

External stress could alter charge transport mechanism. For this to take effect, it is essential to choose materials which have simultaneously piezoelectric and photovoltaic properties, meaning, a crystal with a non-centrosymmetric structure.

When light illumination couples with piezoelectricity and semiconductor behaviour, "piezo-phototronic" effect arises[20]. This is an interface effect, where the charges generated due to the piezoelectric effect would alter the basic mechanisms such as charge generation during illumination, separation and recombination. A material that simultaneously enables photon excitation and piezoelectric processes, can exhibit a piezo-phototronic effect. The piezo-phototronic effect is to use the piezopotential to tune the charge generation, separation, transport and recombination at an interface for achieving superior optoelectronic processes[20].

In semiconducting materials, the inner crystal's piezo-potential is modulated to control the processes in the p-n junction[20]. This effect can be visualised using the Fig 1.7. The contact between a metal and an n-type semiconductor forms a Schottky barrier ($q\phi_{SB}$) at the interface. Under illumination, electron-hole pairs are generated. These new charge carriers increase the conductance by reducing the Schottky barrier height at the interface. This is shown in Fig 1.7a and b.

When stress is applied to such a contact, a piezo-potential is created. This piezo-potential changes the local contact characteristics by building an internal field (E_{piezo}). This internal field takes its effect in the charge transport process at the metal-semiconductor interface by increasing the height of the local Schottky barrier to ($q\phi\prime$).[20,21] .

If a semiconductor nano-wire is placed instead of an n-type semiconductor, a similar process might occur. This is visualised in the Figure 1.8, where a nano-wire has metal contacts along its polar c-axis. When this nano-wire is illuminated with light energy greater than the band gap of the material, excess charge carriers such as electron-hole pairs are generated. Under steady illumination, the number of excess electrons generated equal the number of holes. This excess concentration of charge carriers is given as:

$$\Delta n = \Delta p = \tau_n G_L(I) \tag{1.15}$$

where,

Δn	Excess electron concentration
Δp	Excess hole concentration with illumination
τ_n	Carrier lifetime
$G_L(I)$	Rate of photon generation as a function of light intensity

When the nano-wire is not illuminated, the Fermi level of the metal and that of the semiconductor nano-wire line up. Under illumination, excess charge carriers are generated which will split the original Fermi level into quasi-Fermi levels for electrons and holes

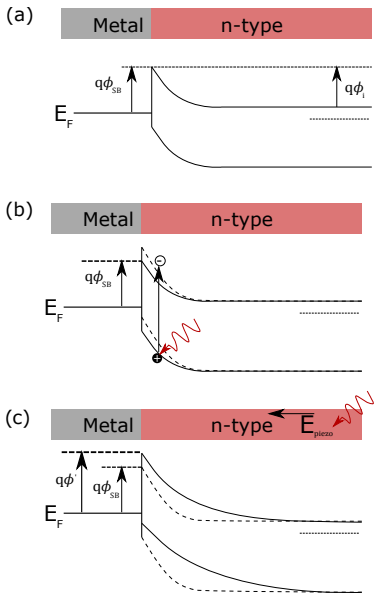

Figure 1.7: Band-diagram of a metal-semiconductor interface. (a) Band-diagram of a Schottky contacted metal-semiconductor interface (b) Band-diagram of an illuminated Schottky contact (c) Band-diagram at the Schottky contact after applying stress depicted by an arrow. Redrawn from Wang Zhong Lin (2012)[20]

respectively, pictorially shown in Figure 1.8(b). The quasi Fermi level E_{Fn} for electrons and E_{Fp} for holes can be described by:

$$E_{Fn} = E_F + k_B T \; ln \left(\frac{n_0 + \Delta n}{n_0} \right) \tag{1.16}$$

$$E_{Fp} = E_F + k_B T \; ln \left(\frac{p_0 + \Delta p}{p_0} \right) \tag{1.17}$$

where,

k_B	Boltzmann constant
T	Temperature
n_0 & p_0	Initial concentration of electrons and holes
Δn & Δp	Excess carrier concentration

When stress is applied, the resultant piezo-potential modulates the Schottky barrier height. The piezo charges can be seen as fixed charges at opposite ends of an anisotropic crystal with opposite signs. This is visualised in the Figure 1.8(a) as piezo charges. The change in the Schottky barrier height due to the piezo charges is given by:

$$\Delta\phi_{piezo} = -\frac{1}{2\epsilon} \; \rho_{piezo} \mathbf{W}^2_{piezo} \tag{1.18}$$

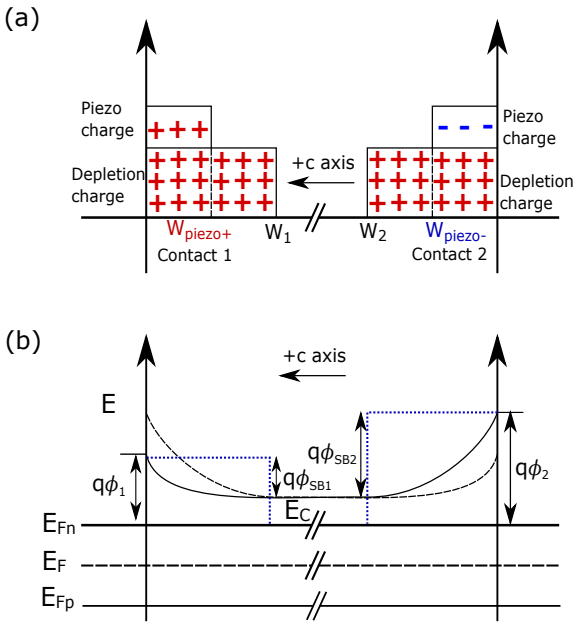

Figure 1.8: Schematic representing interface effect for piezo-phototronic effect and its band diagram. Solid line represents the Schottky barrier without stress and the dotted line depicts the Schottky barrier altered after applying stress. Redrawn from Y Liu, Advanced materials (2012)[22]

Where,

ρ_{piezo}	Density of the stress-induced piezo charges
W_{piezo}	Width of the piezo-polar charge at the interface
ϵ	Dielectric constant of the anisotropic material

If the stress along the nano-wire is along the +c-axis of the semiconductor nanowire, the piezo polarization is given as:

$$P = d_{33}\sigma_{33} = \rho_{piezo^1} W_{piezo^1} = -\rho_{piezo^2} \mathbf{W}_{piezo^2} \tag{1.19}$$

Where,

d_{33}	Piezoelectric constant along +c
σ_{33}	Stress along the c-axis
ρ_{piezo^1}	Density of piezo charges induced due to stress at contact 1
W_{piezo^1}	Width of the piezo-polar charge at the interface 1

Photo-excitation would effectively reduce the barrier height while introducing the piezo charges consequently altering the barrier height, as shown in the figure 1.8(b).

This is explained quantitatively as,

$$\begin{aligned}\Delta\phi_n &= -\frac{1}{2\epsilon}\,\rho_{piezo}\mathbf{W}^2_{piezo} - k_B T\; ln\left(\frac{n_0+\Delta n}{n_0}\right) \\ &= \Delta\phi_{piezo} - (E_F - E_{Fn})\end{aligned} \tag{1.20}$$

The modified barrier height is:

$$\phi_n = \phi_{n0} + \Delta\phi_n \tag{1.21}$$

where ϕ_{n0} is the original Schottky barrier height without stress or illumination.

Chapter 2

Lithium Niobate

Crystals of lithium niobate were first grown from a melt solution in 1949 by Matthias and Remeika.[23] The electro-physical properties of $LiNbO_3$, its crystal structure and growth condition were studied by Nassau and Ballman.[24] Currently, single crystal lithium niobate is grown in air via Czochralski technique. A cylindrical crystal is pulled vertically from a melt from an initial seed crystal. Czochralski grown lithium niobate single crystals are multi-domain. In order to produce single domain crystals, an electric field is applied during the growth process.

Crystallographic properties: Lithium niobate $LiNbO_3$ at room temperature belongs to the rhombohedral (trigonal) space group R3c, with a point group 3m. The centrosymmetric space group R3m occurs above the phase transition temperature. There are three choices of axes for $LiNbO_3$, rhombohedral, hexagonal and orthohexogonal cells. In order to study the properties, the orthohexogonal setting is preferred. Hence, the tensor components of the properties are given with respect to this setting.

The structure of lithium niobate in hexagonal axes is given in Fig. 2.1. Here, the threefold rotational z axis is along the polar c axis, the axis y lies in the mirror plane which is the b axis, and the x axis is orthogonal to the others. The x-axis in this system is non-polar while the y and z-axis are polar. When uniaxial compressive stress is applied along the z or the y-axis, charge appears on these faces showing that these axis are polar piezoelectric. Also, the z-axis produces charge on cooling and heating the crystal exhibiting pyroelectric properties.[25]

Lithium niobate belongs to the pseudoilimenite structure. It is formed with distortion of niobium-oxygen octahedra. Chains of the distorted oxygen octahedra having common faces, are aligned along polar c-axis. In the non-polar centrosymmetric phase at $T > T_c$ the Li^+ ions are localized within the oxygen planes, whereas the Nb^{5+} ions are in the centre of the oxygen octahedra.[31]

In the ferroelectric phase at $T < T_c$, the Li^+ ions are shifted with respect to the centre

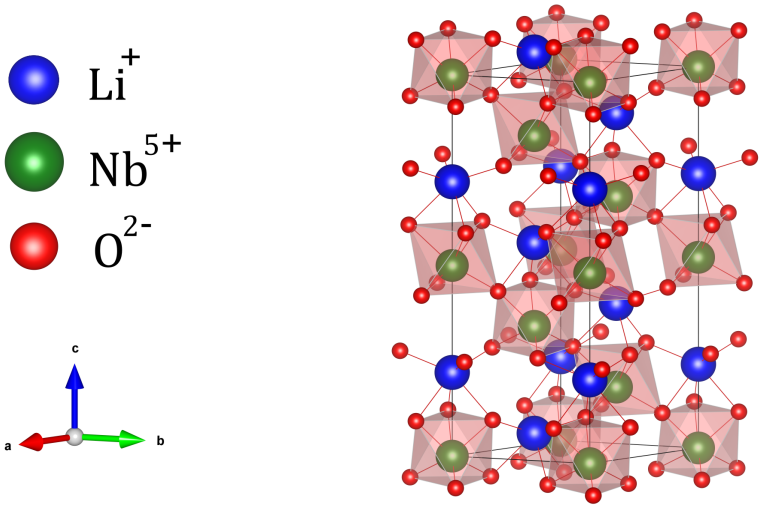

Figure 2.1: A typical structure of lithium niobate in hexagonal axes. This structure is recreated from the crystallographic information obtained from the article by Schirmer O.F (2011)[1] with a 3D visualization program called VESTA.

of the oxygen plane by 44 pm, and the Nb^{5+} ions by 26-27 pm with respect to the centre of the octahedron. As a result, in the polar phase structure, the octahedral interstitials are one-third filled by Li ion and one-third by Nb ions and one-third are empty.[25]

The alternation of the cation sites may be schematically depicted as a chain –Li – Nb – V- – Li – Nb – V– where V is a vacancy or an empty octahedron. The Li octahedron is larger than the Nb octahedron. The distances between the Li and the closest oxygen ions are 206.8 pm and 211.2 pm, whereas those for an Nb ion are 188.9 pm and 211.2 pm respectively. A larger size of the Li octahedron may qualitatively explain a predominant incorporation of impurity ions, either anti-site incorporation or transition metals onto Li sites.

$LiNbO_3$ (LN) crystals are colourless, chemically stable and insoluble in water and organic solvents, and have high melting points. Some of the widely studied properties of congruently melting LN (cLN) are given in the table 2.1. Due to high electro-optic, piezoelectric, and pyroelectric coefficients, LN is exploited for specific purposes in various applications such as electro-optic (EO) modulators,[32] frequency doublers, in volume holographic storage devices,[33,34] in phase conjugated mirrors,[35] optical filters, optical switching devices, acousto-optical actuators and in second- harmonic generation (SHG).[36]

Impurities or doping lithium niobate with transition metals such as Fe, Mn, Cu and Ce in LN increase the photorefractive property and hence improve data storages capabilities. Fe:LN is also used as a pyroelectric infrared sensor and in X-ray generation applications.[37,38]

In integrated Si photonics, stress is applied on a Si waveguide breaking the lattice sym-

Property	c - LN	NSLN
Melting point (°C)	1255 [26]	< 1200
Density (gcm^{-1})	4.643 [27]	4.635
Thermal expansion		
α_a 10^{-6} at 300 K^{-1}	14.1 [28]	14.1
α_c 10^{-6} at 300 K^{-1}	4.1 [26]	6.0
Thermal conductivity		
at RT ($Wm^{-1}K^{-1}$)	3.92 [29]	5.97
Curie Temperature T_c (°C)	1140	1206
Dielectric constants under tension(T)		
and stress(S)		
$\epsilon_{11}^T; \epsilon_{33}^T$	84; 30	54; 42 [25]
$\epsilon_{11}^S; \epsilon_{33}^S$	44; 29	42; 41
Spontaneous polarization		
P_s (μ C cm^{-2})	71	62 [30]
Refractive index		
$n_o; n_e$ at 633nm	2.286; 2.203	2.288; 2.190
EO coefficient under tension (T)		
and stress (S)		
r_{33}^T ; r_{31}^T; r_{22}^T pmV^{-1}	32; 10; 6.8	38; 10.4; - [26]
r_{33}^S ; r_{31}^S; r_{22}^S pmV^{-1}	31; 8.6; 3.8	- ; - ; 4.5 [26]

Table 2.1: Properties of LN. Complied from a book by T.Volk [25]

metry to take advantage of the induced second-order optical non-linearity as well as the linear electro-optic effect (Pockels effect). [39] But the second-order optical non-linearity induced via Si is not high since Si is a non-polar crystal. [40] Lithium niobate with its high non-linear optical coefficients and being a polar crystal, is an ideal material for non-linear integrated photonics. LN has high EO coefficients and are transparent in the μm wavelength range. Hence it is the best material to fabricate waveguides and for EO modulation for analogue, digital data and telecommunication industries. [41]

Lithium niobate is also an ideal acoustic emission transducer or sensor material which can be used in nuclear reactors since it can perform at a broad range of frequencies, can be fabricated into a small size, has a high piezo electric sensitivity, mechanical strength, and stable due to high Curie temperature. Lithium niobate can withstand several megarads of pure gamma radiation (to a limit of 88 MGy) and neutron radiation (to a

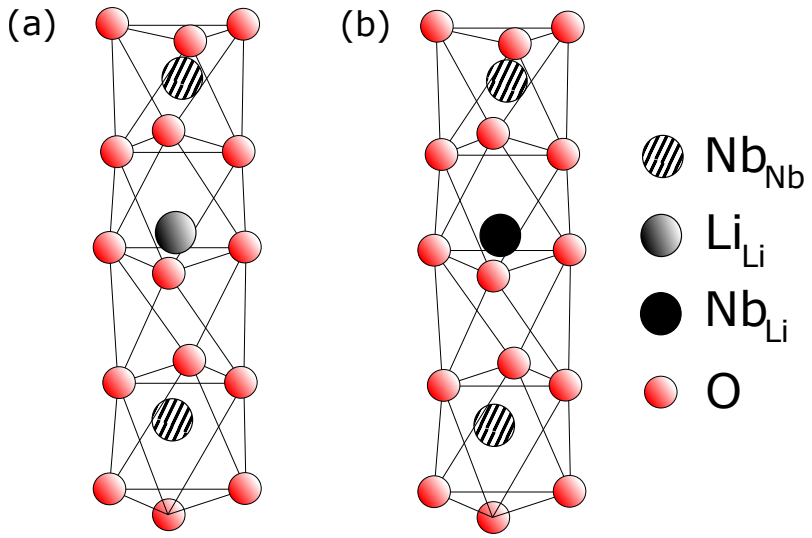

Figure 2.2: Lithium Niobate vacancy model. (a) Chain – Li – Nb – V – Li – Nb – V –, where V denotes a vacancy. (b) Lithium niobate with an anti-site niobium, i.e., Nb on an Li site. Redrawn from a book Lithium Niobate by T. Volk [25]

limit of $2 \times 10^{21} n/cm^2$) before a change in the dielectric constant is observed. [42] Doping LN with Fe or Cu also increases the resistance showing no change or defect up to a total dose of 10^{10}rad making it an ideal material for use in high radiation environments such as nuclear reactors or extra-terrestrial devices. [43,44]

2.1 Point defects in LN

There are several defects in as-grown LN, intrinsic and extrinsic. Intrinsic defects relate to the structure and extrinsic relate to the impurity.

Intrinsic defect structure:

Vacancies and anti-sites c-LN contains about 6% empty Li sites in the lattice, which is denoted by V_{Li}. LN is a unique oxide containing no oxygen vacancies. [31] With decreasing Li_2O content in the melt, there is an increase in V_{Li}. This decrease in the Li content is accompanied by an increasing content of the heavier Nb. Consequently, the density of $LiNbO_3$ increases. The anti-site incorporation of the Nb replacing Li site is very probable, due to the smaller ionic radius (Li^+ ionic radius - 76 pm and Nb^{5+} ionic radius - 64 pm). Therefore, the Li-deficient crystal occur with Nb surplus. This incorporation of a Nb ion onto the Li site is called an Nb anti-site defect and is represented by Nb_{Li}^{5+}. [45–47]

When the anti-site niobium replace the lithium sites excess charge is created. To maintain charge neutrality, niobium vacancies are created which are denoted by V_{Nb}. Hence,

intrinsic defects in c-LN can be summarized as V_{Li}, Nb_{Li}^{4+}, V_{Nb}.

Large and small polarons If an electron is trapped by a cation in its site, a local distortion is created in the ordered lattice structure. Local distortion is a result of self-stabilisation due to the inclusion of an electron. This stabilisation creates a strong interaction between the electron and the neighbouring cationic sites in the lattice creating a quasi-particle called a "polaron". In other words, the deformation induced due to the build up of excessive carriers trapped at a cationic site in the lattice is called a polaron.

If electrons are self-trapped at the regular site Nb_{Nb}^{5+}, it forms "small free polaron" which is Nb_{Nb}^{4+}. If this lattice deformation extends over a distance of the order of inter-atomic spacing, it is called a "small polaron". If this lattice deformation extends beyond the inter-atomic spacing a "large polaron" is formed. Other than size or the scope of deformation in the lattice, small and large polarons differ in their electrical transport mechanisms. Large polarons tend to have band-like transport while small polarons have "hopping" transport. This special type of charge transport will be discussed in the further sections.

The electrons are captured by the pre-existing or newly formed neighbouring complexes $Nb_{Nb} - Nb_{Li}$ to form a diamagnetic bipolaron and a stable bonded electron pair $(Nb_{Nb} - Nb_{Li})^{2-}$. Here, two nearest neighbouring pairs $(Nb_{Li}^{5+} - Nb_{Nb}^{5+})$ bind two electrons forming a bipolaron. The formation of a bipolaron is energetically favourable and qualitatively means a self stabilization of an electron pair.[48]

Extrinsic defects in lithium niobate, the transition metal (TM) impurities: Several extrinsic impurities/defect ions can be incorporated in LN. There is a possibility that these extrinsic defects are incorporated at an empty octahedron. The ionic radii of Li^{+} and Nb^{5+} are 0.76 pm and 0.64 pm respectively, which are similar to each other. Most of the transition metal impurities however, prefer the V_{Li} sites independent of their charge with few exceptions for ions such as Mg which replace V_{Nb} sites with increasing dopant concentration.

The distribution of the impurity sites in LN is mathematically described by the effective distribution coefficient (k_{eff}) as:[25]

$$\frac{c_S}{c_M} = k_{eff}\left[(1-g)^{k_{eff}}\right] \tag{2.1}$$

where g is the solidification fraction and c_S and c_M are the concentration of impurity in the crystal and the melt respectively.

Photorefractive centres/impurity ions in lithium niobate: Dominant mechanism in lithium niobate is photorefraction which leads to the bulk photovoltaic effect. The

photorefractive centres in lithium niobate are defined by the presence of ions belonging to the multi charge transition metal (TM) impurities. One of the TM impurity ions studied heavily for bulk photovoltaic charge transport is Fe.[1,16,49] Other common TM impurities are Mn, Cu, Ti, Ni, Co, Cr, Rh, Mg.[50,51] Table 2.2 shows the ionic radii of some TM impurities in lithium niobate along with the electrons which occupy the outermost orbitals.[52]

Ion	Last orbitals	Ionic radii
Fe^{2+}	$3d_6$	0.6 (LS);0.77 (HS)
Fe^{3+}	$3d_5$	0.55 (LS);0.645 (HS)
Cu^{+}	$3d_{10}$	-
Cu^{2+}	$3d_9$	0.73
Mn^{3+}	$3d_4$	0.58
Mn^{4+}	$3d_3$	0.54
Co^{2+}	$3d_7$	0.735
Co^{3+}	$3d_6$	0.61
Ti^{3+}	$3d_1$	0.67
Ti^{4+}	$3p_6$	0.605
Mg^{2+}	$2p_6$	0.72
Nb^{4+}	$4d_1$	0.69
Nb^{5+}	$4p_6$	0.64
Li^{+}	$1s_2$	0.74

Table 2.2: Common transition metal impurities in LN and their outermost orbitals and corresponding ionic radii. Taken from Shannon (1976)[52]

Most TM impurities induce colour to the cLN crystals, which show strong optical absorption bands from UV up to near-infrared wavelengths. Extrinsic doping of TM impurities could (a) alter the phase transition temperature, (b) increase the density of the crystal and (c) shift the band edge. Transition metal impurities are incorporated in different valence states, for example iron is incorporated as Fe^{2+} or Fe^{3+} states whereas, copper is incorporated as Cu^{+} and Cu^{2+} and manganese as Mn^{3+} and Mn^{4+}.These multi-valence impurities can be reduced or oxidised by post-growth annealing treatments to either add or remove electrons.

2.2 Band formation in LN

The band gap of LN is a speculative topic. The large band gap values of LN are usually from optical measurements.[53] Doping LN with transition metal impurities and electron-hole attraction effects might reduce the actual band gap via band bending or band tailing due to minor changes in ionization energies and electron affinity. Band gap of lithium niobate was however calculated taking into consideration the phase, dielectric screening and electronic excitations using the Density Functional theory - Generalized Gradient Approximation (DFT-GGA) to determine the structurally relaxed ground state of the ferroelectric LN phase.[54] The band gap calculated from this approximation gives a band gap (E_g) value around 3.78 eV.[55]

The valence electron configurations of the atoms comprising in the crystal are as follows:

1. For Li $\longrightarrow 2s^1 2p^0$
2. For Fe $\longrightarrow 3d^7 4s^1$
3. For Nb $\longrightarrow 4p^6 4d^4 5s^1$
4. For O $\longrightarrow 2s^2 2p^4$

The conduction band is mainly composed of the Nb $-$ $4d$ band. The contribution of O $-$ $2p$ band which creates the valence band, is substantial because of the hybridization between the Nb $-$ $4d$ and O $-$ $2p$ bands. Between the valence band formed by O^{2-} ions and conduction bands formed by Nb^{5+}_{Nb} ions, a defect centre may probably exist for a possible electron transfer due to excitation from a defect centre to the conduction band.[56] However, due to the anisotropy of the crystal structure, it is not necessary that the charge transfer to the conduction band occurs equivalently in all directions. This requires speculation on a few issues such as:

1. The unequal inter-ionic distances between the defect centre and the neighbouring ions (asymmetry/anisotropy).
2. The ionic state of the defect centre - creating orbitals which interact with the conduction band orbitals.
3. The position of the defect centre in the band structure.
4. The amount of V_{Li}, V_{Nb}, Nb_{Li} already in the crystal and concentration of the defect ion.

Issues 1 and 2 can be studied with a closer look at the structure of lithium niobate which furnish better understanding over the bonding, atomic interactions and orbital formation. The structure of LN with an extrinsic impurity Fe replacing the Li site is shown in the Fig. 2.3.[1] Issues 3 and 4 could be investigated with light-induced measurements and other spectroscopic techniques, which would be introduced in the experimental section.

2.3 Structure of TM:LN

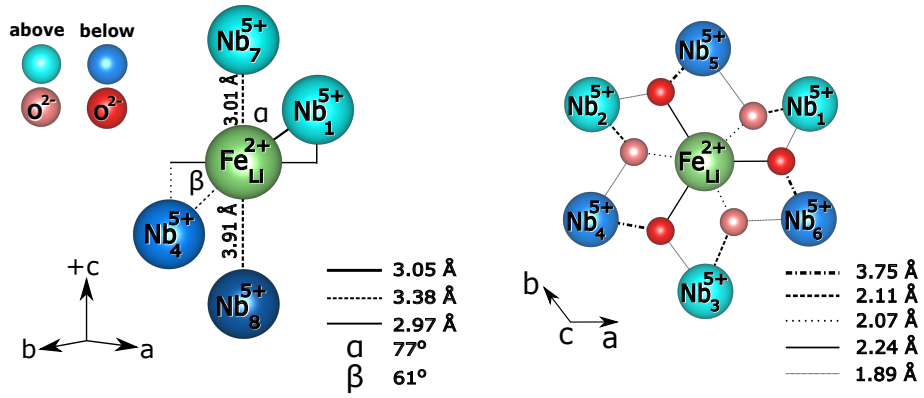

Figure 2.3: Structure of Fe:LN with interatomic distances where the arrangements of Fe_{Li}^{2+} and the neighbouring Nb_{Nb}^{5+} ions are depicted. Inter-ionic vectors connecting the ions are given in Å. Numbering of the Nb_{Nb}^{5+} ions would provide ease in understanding the location of a specific niobium ion, while discussing the charge transport. The ions, Nb and O positioned above and below the plane are colour coded with respective shading as shown in the legend. The figure towards left - is the structural diagram when the crystal is cut along the yz glide mirror plane. The figure to the right - is a schematic projection on a xy plane, which is perpendicular to c-axis. Redrawn from Schirmer O.F (2011)[1]

The relationship between the electron configuration of TM ions and their interaction between the neighbouring ions in a crystal is complex. In the table 2.2 the outer most electrons in their respective orbitals are given for each ion. Example, the complexes formed for Fe are Fe^{2+} and Fe^{3+}. Electrons are removed from the valence *s* shell orbital before they are removed from the valence *d* orbitals when a TM is ionized. A change in the oxidation state of TM ions results in a change in colour even for complexes, due to formation of a coordinate compound. For example, the electron orbital of the TM ion Fe^{2+} forms a diffused coordination complex of d_{z^2} which interacts with an already existing degenerate principle orbital p_z formed by an Nb_{Nb}^{5+} ion or a diffused degenerate d_{z^2} formed by Nb_{Nb}^{4+} small free polaron. A pictorial depiction of such orbitals which represent the probability of existence of electrons in such regions is shown in the Fig. 2.4.

In the ferroelectric phases LN is iso-structural, differing in small changes in atomic co-ordinates not fixed by symmetry.[57] The ligand fields at the cation sites formed with regard to the symmetry of LN are not strong and most $3d^n$ ionic impurities adopt high spin configurations.

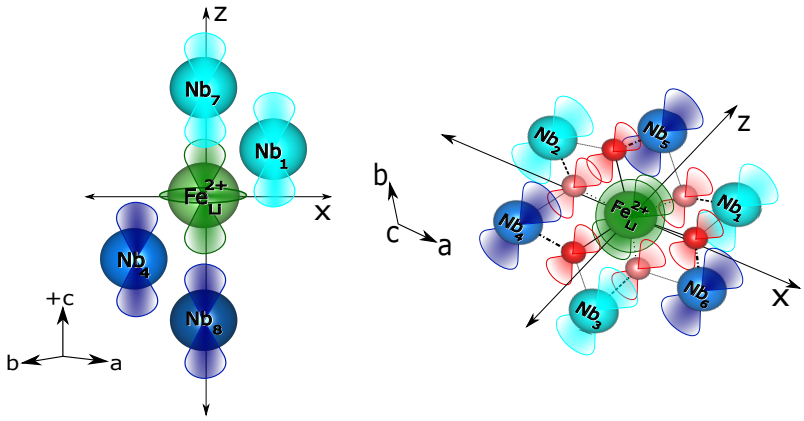

Figure 2.4: Structure of LN with Fe replacing the Li site - showing orbital interaction. Idea taken from Schirmer O.F (2011)[1]

2.4 Light induced - charge transport mechanism in LN

Charge generation and transport in LN can be explained according to photo-induced current generated by processes such as initial excitation, transport of charge and recombination mechanisms.[25,48]

Driving forces of photo induced current: The movement of free charge carriers give rise to drift, the bulk photovoltaic effect and diffusion currents. The total photovoltaic current density j_{ph} is a cumulative of them.

$$j_{\text{ph}} = j_{\text{drift}} + j_{\text{pv}} + j_{\text{diff}} \tag{2.2}$$

The drift current arises due to the coulomb interaction of an electric field with the charge carriers, and obeys Ohm's law.

$$J_{\text{drift}} = \widehat{\sigma} E \tag{2.3}$$

where,

$\widehat{\sigma}$	Conductivity tensor
E	Electric field

If the electric field is not aligned along one of the main axes of the crystal, a current in the direction perpendicular to E can still arise. Mobility of the charge carriers differ for different crystal directions.

The diffusion current arises due to inhomogeneity in illumination which create spatially varying concentrations of free charge carriers.

$$j_{\text{diff}} = -Q\widehat{D}N_{e,h} \tag{2.4}$$

where,

Q	-q for electron and +q for hole conductivity
$\widehat{D}$	diffusion tensor

The photovoltaic current density j_{pv} is discussed in section 1.4.2 and the relation to the light intensity and the light electric field polarization is given in the equation 1.14.

The models concerning the charge transport mechanism for light induced processes of photorefractive crystals, would be discussed below.

2.4.1 One centre model of charge transport

Assuming that the crystals are homogeneously illuminated, a model concerning charge transport which was extensively researched is the one-centre charge transport.

Charge transport model without electron-hole competition: The origin of free charge carriers and their recombination mechanism are the basis of light induced charge transport in non-centrosymmetric crystals.

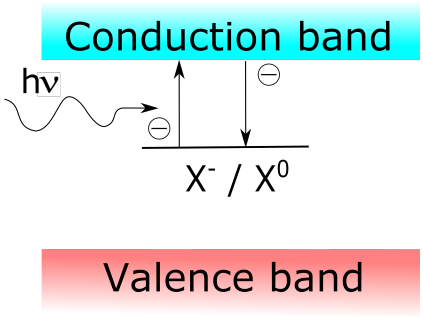

Figure 2.5: Band-diagram depicting one centre excitation and recombination charge transport without e-h competition. Redrawn from Buse. K (1997).[48]

Electrons are excited by light from filled traps/donors X^- into the conduction band and free electrons recombine from the conduction band with empty traps X^0.[48]

$$\frac{d[X^-]}{dt} = -(G_T + q_{\text{ef}}SI)[X^-] + r[X^0]N_e \tag{2.5}$$

$$N = [X^-] + [X^0] \tag{2.6}$$

where,

$[X^-]$	Concentration of X^- centres
$[X^0]$	Concentration of X^0 centres
G_T	Thermal generation rate
q_{ef}	Quantum efficiency for excitation of a free electron on absorption of a photon
S	Photon absorption cross section
I	Light intensity in photons per square meter and second
r	Recombination coefficient
N_e	Concentration of electrons in the conduction band
N	Total concentration of the photorefractive centre

In Fig. (2.5) we see only one level for X^- and X^0. This X^-/X^0 energy level corresponds to the thermal excitation energy required to excite an electron from X^- into the conduction band creating X^0. However, the optical excitation energy required to excite an electron from X^- to the conduction band can be huge because of the difference in the momentum of valence electron for X^- and the electron in lowest energy state of the conduction band.

Under homogeneous illumination, the conductivity in a steady state situation is,

$$\sigma = q\mu_e N_e \tag{2.7}$$

$$N_e = \frac{G_T + q_{\text{ef}} SI}{r} \frac{[X^-]}{[X^0]} \tag{2.8}$$

σ	Conductivity in the steady state situation
μ_e	Component of the mobility tensor

The photo-conductivity increases linearly with light intensity, for low thermal excitations where, $G_T < q_{\text{ef}} SI$. Hence the photo-conductivity is proportional to the ratio of concentration of filled and empty electron traps.

The absorption coefficient α is equal to $S[X^-]$. For homogeneous illumination changes occur only because of excitation of electrons into the conduction band. Thermal reduction of the crystals decreases the concentration of empty traps. This enables a comparison of N_e to $[X^0]$. By homogeneous excitation of electrons, the density of filled traps become constant and the bulk photovoltaic current is proportional to light intensity.

$$J_{\text{pv}} \propto I \tag{2.9}$$

2.4.2 Appearance of PV current in LN

The appearance of the photo-induced charge discussed in the model above can be explained via an atomic basis. This requires to take into consideration the structural environment and the polaronic features in the first coordination sphere around the TM ion. For better visual understanding of the transfer probabilities due to the anisotropy of the crystal structure, the structural model shown in Fig. 2.3 is referred. The figure representing the inter-atomic distances for LN cut along yz glide mirror plane shows the axial/rotational symmetry of the 3m point group. The orbitals involved in this particular orientation, Fe^{2+}_{Li} ($3d^6$) creating the orbital ($3z^2$) are shown in the Fig. 2.4.

Light absorption in Fe:LN originates due to photo-excitation of an electron from the outer most orbital of Fe^{2+}_{Li} to the neighbouring Nb^{5+}_{Nb} site creating a Fe^{3+}_{Li} trap and Nb^{4+}_{Nb} small free polaron.

$$Fe^{2+} + h\nu \longrightarrow Fe^{3+} + e^{-} \tag{2.10}$$

where Fe^{2+} ions are donors and Fe^{3+} ions are traps.

"*The total optical absorption essentially results from a superposition of electron transfers from the TM ion to eight surrounding* Nb *ions*".[1] The light-induced local current is a net of each transfers which is a time dependent change of Fe − Nb dipole. A total of all the relative projections of the individual dipolar currents in all the directions gives a net current in the +c direction. In a centrosymmetric crystal the total dipolar current projections would add up to zero. However, in a structure such as LN, it would not add up to zero. The probability to create small polarons would depend on the inter-atomic distances of $Fe^{2+}_{Li} - Nb^{5+}_{Nb}$ distances.

In the +c direction, there is an asymmetry in the inter-atomic distances between Fe and the neighbouring Nb ions. The distances of the inter-atomic bonds projecting in specific directions are not equal to one another. These unequal distances give rise to dipolar currents which are different from one other giving rise to a sizeable net current along the +c direction. The tensorial characteristics of the current density j_{pv} in a particular direction, is a result of a net current generated via contributions from multiple dipoles interacting under specific conditions of the light electric field.

The transition probability hence would depend on:

1. Inter-atomic distances.
2. Polarization direction of the light electric field.
3. No. of Nb_{Nb} disposing to turn into Nb^{4+}_{Nb} small free polarons.

Theoretical understanding of charge transport in LN:

In order to interpret the photovoltaic tensor, it is needed to analyse the anisotropic properties of the dipole interactions. "*These dipole interactions would then be viewed as transitions to the conduction band, which would be: (a) Transitions to low lying Franck-Condon* [1] *excited small polaron states which are resonant with the conduction band states - determined by the defect potential, and (b) Contributions arising from the admixture of band states which are governed by the periodic lattice potential, which dominate with rising photon energies* ".[1]

The starting process kicking off the photovoltaic current j_{pv} is the initial coherent charge transport before being randomized by scattering. This coherent charge transport is a band like motion from the TM centre to the Nb_{Nb}^{5+} creating an Nb_{Nb}^{4+} small free polaron and very fast relaxation to one of the Fe_{Li} dopants via incoherent diffusive hopping motion, and recombination.

Influence of polarons: Electronic conduction in crystalline oxides can occur by motion of free charge carriers in a band or by diffusion-like motion called "hopping" process. The mobility of the small polaron however depends on the how far through the lattice it would carry its induced lattice deformation.[58,59]

The hopping process can be explained as follows. At a particular moment, a crystal lattice may have equal distortions at the electron occupied site and its neighbouring site. This enables the electron to tunnel since the energy of both the sites become equal. When the electron tunnels or moves from one site to the other it creates a polaron with every move. The momentary occurrence of equal energy is called a 'coincidence event '.

"*Electrons self trapped at the regular* Nb_{Nb}^{5+} *($4d^0/3p^6$) ions of the LN lattice form the most simple polaron species, the free polarons* ".[60] In such cases the optical absorption spectra would be a cumulative of the absorption due to niobium polarons and absorption caused by extrinsic dopant defects.

A polaron and its effect on its neighbouring lattice sites can be visualised as shown in the Fig. (2.6). Successful transfer of a local distortion through the lattice can occur at high probability. This is because the distortion at the initial site has little effect on the electron energy at the final site.

The shape of the absorption band of a small polaron is also determined by the coupling of

[1] The Frank-Condon principle describes the vibronic transitions or absorption/emission of a photon. During an electronic transition such as ionization no change occurs to the nuclear configuration of the crystal instead it realigns with the new electronic configuration and undergoes a vibration. In a quantum picture, the small polaron excitation occurs by changing its vibronic states from ground to a higher state. This new oscillating state of the small polaron causes a localised distortion which is compensated by neighbouring sites. When this distortion or vibronic oscillation of a small polaron equals to the oscillations of a neighbouring polaron (in resonance), tunnelling of an electron occurs resulting in conduction. This is termed the hopping mechanism.

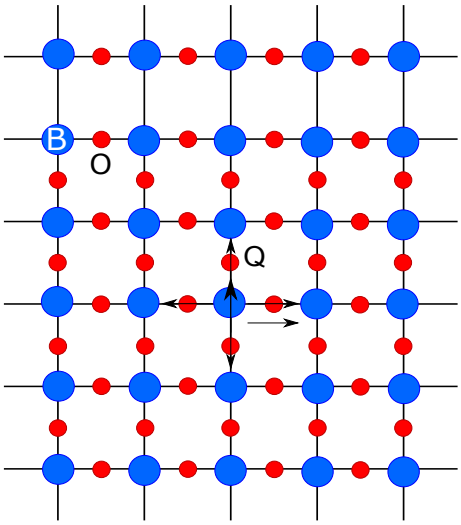

Figure 2.6: Visualisation of a polaron such as Nb^{5+}_{Nb}. For example, in an ABO_3 perovskite structure, a polaron at a B cation is visualised in a BO plane. The electron is symbolized with a spin-up (an arrow). In order to stabilise, the extra electron causes a local distortion in its neighbouring lattice sites. The distortion here is mainly caused by repulsion of its neighbouring ions. Interaction coordinate Q and the arrows describe this distortion or the repulsive forces. Redrawn from Schirmer O.F (2009).[60]

the charge carrier to the lattice. Let the vibrational functions at the initial site be $|\lambda\rangle$, and the ones at the final state be represented as $|\rho\rangle$. The vibrational function at the ground state at the initial site could be represented as $|\lambda_g\rangle$ and the light induced transitions to the final site at any given state could be represented as $|\rho_n\rangle$ where n could be any of the vibrational quantum states the small polaron could reach. This two well system, where the small polaron light induced transition occurs is visualised in Fig. 2.7.[60]

The combination of electronic transitions as wave-functions for both the initial and the final sites results in a finite dipole moment. This is given as a Hamiltonian H as:

$$H = \begin{bmatrix} -V_f Q & J \\ J & 0 \end{bmatrix} \tag{2.11}$$

Where,

V_f	net force on the neighbouring atoms
Q	interaction coordinates
J	transfer energy

The distortion induced electronic energy difference between the initial and the final sites is $\Delta E = -J^2$ which is the difference between the diagonal elements in equation 2.11.

Assuming $J \ll V_f Q$, leads to the first -order perturbed states:

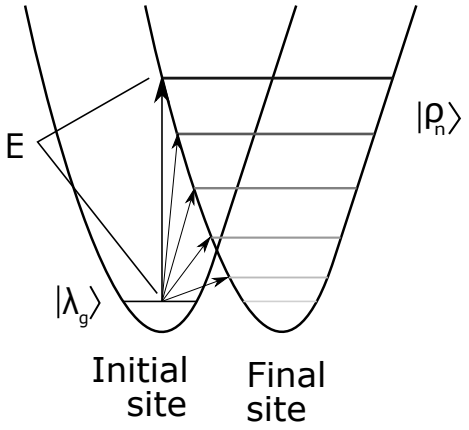

Figure 2.7: Two wells exemplifying light induced transitions from a vibrational ground state at the initial site to any of the vibrational states at the final site. Redrawn from Schirmer O.F (2009)[60]

$$\text{The initial } |I'\rangle = |I\rangle + (\frac{J}{\Delta E})\,|F\rangle$$

$$\text{The final } |F'\rangle = |F\rangle - (\frac{J}{\Delta E})\,|I\rangle$$

In a classical picture, ΔE represents the amount of photon energy required for the transfer to take place from the the initial $|I'\rangle$ to the final $|F'\rangle$ state. The amount of absorbed photon energy for the transfer can be $\hbar\omega$ where, ω angular phonon frequency. The polarization of the absorbed band is represented by the direction of the transition dipole moment $\vec{\mu}$, which is evaluated by the initial $|I'\rangle$ and final $|F'\rangle$ states. The value of the transition dipole $\vec{\mu}$, $|I'\rangle$ $|\vec{\mu}|$ $|F'\rangle$, is approximately $J\mu/\hbar\omega$. So the total absorption band is proportional to the energy of the phonon and to the transition dipole moment.

The total absorption band is given by:

$$\alpha(\omega) \propto \frac{J^2\mu^2}{\omega}\, exp(-\varpi(\hbar\omega - 2E_P)^2) \tag{2.12}$$

Where,

$\alpha(\omega)$	small polaron absorption as a function of the angular frequency of vibration ω
J	transfer energy
μ	dipole moment
ϖ	total emission/absorption probability per unit time
E_P	energy of the phonon
ω_o	longitudinal optical phonon frequency

2.4.3 Components of BPVE

To better understand the tensorial property of the BPVE charge transport in LN, it is essential to look into the point group symmetry tensors in relation to the BPVE tensor (β_{ikl}). The point group symmetry tensors/ matrices are given in appendix B.

Matrices from appendix B are in accordance with the 3m point group symmetry of LN to deduce the independent, dependent and zero values of the BPVE third rank tensor β_{ikl}, where the first index i represents the direction of charge being measured which is given in the equation 1.14 as $j_{pv,i}$ and the indices k, l represent the direction of the light electric polarization $\varepsilon_k \varepsilon_l$.

The point group symmetry containing matrices in B.1 are used to deduce the third rank tensor BPVE, from the equation A.14. A solution from the resultant equations provide the independent tensor components. These are given in the Fig. 2.8, which represents a Voigt's notation of the BPVE matrix which has three indices (1,2 & 3). Here, the last indices of the BPV tensor are combined to create one index (11 to 1, 22 to 2, 33 to 3, 23 & 32 to 4, 31 & 13 to 5 and 12 & 21 to 6), which makes a 3×6 matrix. A complete list of independent, dependent and zero value components can be seen in the table B.2.

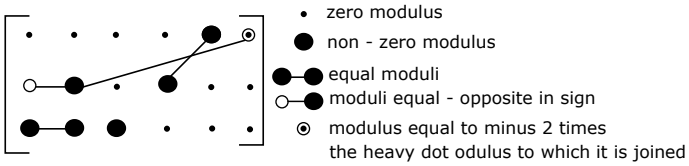

Figure 2.8: Independent, dependent and zero value components of a third rank tensor for point group symmetry 3m. Taken from the book JF Nye (1985)[8]

From Fig. 2.3 we notice the relative atomic positions of Fe_{Li}^{2+} and its eight neighbouring Nb_{Nb}^{5+}. The distance from $Fe_{Li}^{2+} - Nb_7$ is less than that between Nb_8 and distance $Fe_{Li}^{2+} - Nb_1$ is less than that between Nb_4 along the c axis. Assuming that Fe exactly replaces Li site of the defect free crystal,[57] the structural positions remain unchanged with respect to the defect free crystal. An electron being transferred from the $Fe_{Li}^{2+} - Nb_{Nb}^{5+}$ could be considered as an elementary unit where absorption process can be elucidated. In the projection along xy glide plane, there is a probability that electrons in the outer most orbitals in Fe_{Li}^{2+} are linked via indirect coupling by O^{2-} ions (2.4) which surround the Nb_{Nb}^{5+} ions.

Absorption induced charge transfer to each of the niobium ions could thus be studied by the effective transfer integrals J_i where index $i = 1, ..., 8$ represent the eight neighbouring Nb_{Nb}^{5+} as labelled in Fig. 2.3.

The transition dipole vector discussed in the section 2.4.2 is related to the projections of Fe_{Li}^{2+} to its neighbouring Nb_{Nb}^{5+} ions. Hence the arrangement of Nb_{Nb}^{5+} ions and the distances contribute to individual transitions of an electron excited from the defect site

to the final site and consequently to the transfer integral J_i. So, the transfer integral J_i as given in the equation 2.12, typically decreases with rising μ_i in an exponential manner.

In Fig. 2.3, the structural projection to the right is the view along xy plane. This projection shows the view which is perpendicular to c-axis. Here, Nb_1, Nb_2 and Nb_3 are lying above the plane with respect to Fe_{Li} and Nb_4, Nb_5 and Nb_6 are below. The bonds $Fe_{Li} - Nb_1$, $Fe_{Li} - Nb_2$ and $Fe_{Li} - Nb_3$ enclose at an angle 77° from c-axis and the set of bonds $Fe_{Li} - Nb_4$, $Fe_{Li} - Nb_5$ and $Fe_{Li} - Nb_6$ enclose at an angle 61° from c-axis. The former set of Nb ions (Nb_1, Nb_2 and Nb_3 to Fe_{Li} is 3.05Å) have bond lengths shorter than the latter set of Nb ions (Nb_4, Nb_5 and Nb_6 to Fe_{Li} is 3.38Å) hence the ions closer to Fe_{Li} with shorter bond lengths contribute more to the total absorption. If we look at the structural projection to the left in Fig. 2.3, we see the bonds extending along the polar c-axis. The bond length $Fe_{Li} - Nb_7$, which is 3.01Å is shorter than the bond length $Fe_{Li} - Nb_8$, which is 3.91Å. Hence, $Fe_{Li} - Nb_7$ would contribute more to the total absorption. The ions $Nb_{1,2,3,4,5,6}$ have projections perpendicular to the c-axis. The transitions along these bonds are dominated by ordinary polarized light, where as, their projections on the c-axis are rather small and hence extraordinary polarised light drives the transitions along $Fe_{Li} - Nb_7$.

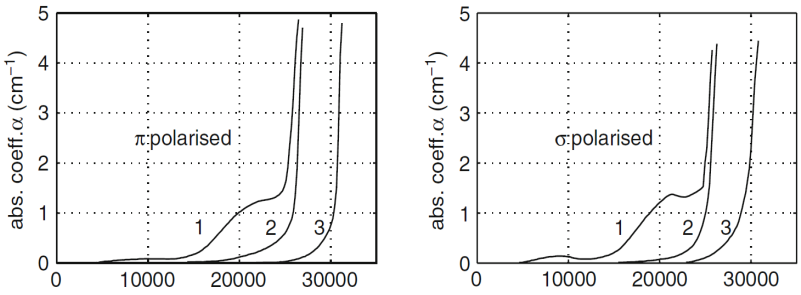

Figure 2.9: Polarized absorption spectra of $LiNbO_3$ + $0.045 wt.\% Fe_2O_3$. For, (1) Crystal quenched from $1100°C$ (2) Slow cooled and annealed at $600°C$. (3) Un-doped $LiNbO_3$ [Taken from Lithium Niobate - Defects, Photo-refraction and Ferroelectric switching. By, Tatyana Volk and Manfred Wohlecke. Redrawn from[25]

But the polarized absorption spectra shown in 2.9 is noticeably isotropic, with the ordinary line being slightly intense of about 10% than the extraordinary one.

However, the transfer integrals do not only depend on the distances, but also the orbitals of the ions in the crystal. The arrangement of the orbitals is visualised in the Fig. 2.4, where the axial and non-axial neighbours of the TM centre are visualised. So it is not merely the inter-atomic distances between the TM centre and its surrounding niobium ions, but the relative orbital orientations would also influence the transfer integrals J_i. Furthermore the positions of the O^{2-} ions forming indirect bonds to the TM centre via the Niobium ions need to be taken into account.

Light-induced changes of the Fe-Nb dipoles Light-induced excitations will trigger all the subsequent processes such as (*i*) the coherent band transport as well as (*ii*) the incoherent hopping movements for charge transport.

The total optical absorption can be described as:

$$\begin{aligned} \alpha_{tot} &= \sum_i \alpha_i \\ &\propto \sum_{i=1,....8} \langle I'|r_l|F_i'\rangle \, \langle F_i'|r_k|I'\rangle . \varepsilon_l \varepsilon_k^* I \end{aligned} \tag{2.13}$$

The matrix elements $\langle I'|r_l|F_i'\rangle$ and $\langle F_i'|r_k|I'\rangle$ represent values expected for the respective transition dipole arms r_l and r_k which are multiplied with the related components of the unit vectors of photon electric fields ε_l and ε_k^*. Here the terms $i = 1, ...8$ represent the time dependent change of the related dipoles of the eight neighbouring Nb_{Nb} ions creating a local current. These transition dipoles are also discussed in section 2.4.2.

The net electronic current can be discussed in two separate cases:

Case a: The net current j following the direction c, $j \parallel c$.

Case b: The net current j following the direction perpendicular to c, $j \perp c$.

Case a: All the transitions to the Nb ions lying above Fe in Fig. 2.3, Nb_1, Nb_2, Nb_3 and Nb_7 have positive projections on the +c direction and those lying below Fe which are Nb_4, Nb_5, Nb_6 and Nb_8 would have negative projections.

The net current j following the direction c, $j \parallel c$ would be:

$$\begin{aligned} j_z &\propto \left[\sum_{1,2,3,7} \langle I'|r_l|F_i'\rangle \, \langle F_i'|r_k|I'\rangle - \sum_{4,5,6,8} \langle I'|r_l|F_i'\rangle \, \langle F_i'|r_k|I'\rangle \right] \times \varepsilon_l \varepsilon_k^* \, . \, I \\ &= j_+ - j_- \end{aligned} \tag{2.14}$$

Equation 2.14 is similar to the equation 1.14. In the experimental section the importance of having a tensorial form of the BPVE coefficient as described in the equation 1.14 would be noticed. In order to treat currents parallel to c-axis, (*i*) it is needed to consider the differences of the dipole changes along the positive and negative axes instead of their sums, and (*ii*) the dipole changes now have to be projected along the c-axis to lead to j_z. When the light electric field is oriented along the c-axis, meaning, extraordinarily polarised light, (a) the photon will activate transitions along the bonds $Fe_{Li} - Nb_7$ and $Fe_{Li} - Nb_8$, and since the bond length of the former is shorter than the latter, it yields a larger values of $J_i^2 \mu_i^2$ and (b) also, the orbitals of Nb_7 and Nb_8 and that of Fe_{Li} have

the same axial symmetry and extend along the same axis. Hence, the mere treatment of transfer integrals w.r.t distances would suffice in this case.

Case b: In the case of contributions of local dipole currents perpendicular to c-axis, the projections of all $Fe_{Li} - Nb_i$ distances in the plane perpendicular to c-axis are equal. Thus the contribution of the bond distances to analyse the the net current or the transfer integrals cannot be made. Instead, the local currents arising in this orientation can be attributed to the indirect coupling of Fe_{Li}^{2+} and Nb_i^{5+} ions, mediated by the O^{2-} ions. From the structure in Fig. 2.3 which is projected perpendicular to c-axis, we notice that the Fe_{Li}^{2+} ions form indirect bonds to the neighbouring Nb_i^{5+} ions with O^{2-} ions. The bond distances in this case are different for Nb_i^{5+} in the positive y direction to the negative y direction. Looking the indirect bond in the case of $Fe_{Li} - Nb_1$, the Nb_1^{5+} ion is indirectly coupled to two O^{2-} ions one projecting up from the plane and one projecting downwards. The bond lengths for the $Fe_{Li} - Nb_1$ could be seen as a sequence 1.89Å $\leftrightarrow$ 2.24Å and 2.07Å $\leftrightarrow$ 2.11Å. If the coupling between $Fe_{Li}-Nb_4$ is taken, the intercalation between the O^{2-} ions with Fe_{Li}^{2+} and Nb_4^{5+} ions is a sequence of 2.07Å $\leftrightarrow$ 1.89Å and 3.75Å $\leftrightarrow$ 2.24Å. Here the former bond lengths are shorter than the latter which is as long as 3.75Å, where a probable weak coupling could persist. The local currents projected along $Fe_{Li} - Nb_1$ are towards the $+y$ direction and the local currents projected along $Fe_{Li} - Nb_4$ are towards the $-y$ direction, the weak coupling in the latter case gives unequal bonding conditions providing asymmetry, and a net current j_y could arise as well.

I. The coherent charge transport: Photon absorption by Fe_{Li}^{2+} induces a current in a coherent manner, j_{coh}, initially keeping its directional properties, extending further into the crystal, before being randomized by interaction with the lattice. j_{coh} corresponds to a ballistic motion before relaxation of the initial momentum.

Concentrating on the $j \parallel c$ case, the local currents along the c-axis are essential. The transition probabilities Υ_i resulting a current $j_{i,c}$ leads to the initial j_{coh} along c. The electron in this case after absorbing a photon, is displaced by a projected transport length $l_{i,z}^{coh}$. Since the light induced dipole changes depend on the index i, the related transport lengths ($\Lambda_{i,z}^{coh}(\hbar\omega)$)could also be indexed by i.

The mean transport length along the c-axis, is given by:

$$\Lambda_{i,z}^{coh}(\hbar\omega) = \frac{\sum_{1,2,3,7} \Upsilon_i(\hbar\omega) l_{i,z}^{coh} - \sum_{4,5,6,8} \Upsilon_i(\hbar\omega) l_{i,z}^{coh}}{\sum_{i=1,\ldots,8} \Upsilon_i(\hbar\omega)} \tag{2.15}$$

II. Incoherent charge transport: A coherent current turns into an incoherent one j_{incoh}, which is termed thermally activated hopping transport.

Transfer integrals relating to small polaron charge transport without the presence of Fe as a defect centre has been discussed in the section 2.4.2. Apart from the transfer

integrals J and frequency ω, it is essential to look into the dependency of the $Fe^{2+}_{Li} - Nb^{5+}_{Nb}$ dipole and the distance d of the Fe_{Li} centre to its neighbouring Nb_{Nb} ions. The shape of the curve $\alpha(\omega)$ in the equation 2.12 is determined by the distribution of probabilities $P(\omega)$ that photons of energy $\hbar\omega$ promote an electron from its initial energy at the Fe^{2+}_{Li} site to Nb^{5+}_{Nb}. The strain induced distortion in the lattice as shown in the Fig. 2.7 reduces its potential energy by $-2E_P$ and by the defect potential E_{sdp} caused by the transition metal defect Fe^{2+}_{Li}. The mean electronic energy change accompanying the excitation of the electron under Frank-Condon conditions is

$$E = 2E_P + E_{sdp} \tag{2.16}$$

And the distribution probability:

$$P(\omega) \propto exp(-\varpi(\hbar\omega - 2E_P)^2 - E_{sdp})^2 \tag{2.17}$$

With the inclusion of the defect potential, equation 2.12 would then become:

$$\alpha(\omega) \propto \frac{J^2 d^2}{\omega}\, exp(-\varpi(\hbar\omega - 2E_P - E_{sdp})^2) \tag{2.18}$$

It is eventually the incoherent part which is measured at the ends of the crystal when BPV current is measured.[1]

Background and Motivation

Solar energy harvesting through photovoltaics (PV) has been recognised globally and is well known. A promising alternative to the traditional energy resources like fossil fuels, hydro-electric and wind, along with exploitation of materials and studying their mechanisms and energy conversion efficiencies gave rise to PV solar cells.[61,62] The PV cells currently available in the market are mostly first generation solar cells. These are based on a p-n junction based devices. Efficiencies of such solar cells currently reach up to 20% depending on the concentration of solar light.[63,64]

Thin film designs[65] based on amorphous silicon,[66,67] polycrystalline silicon (p-Si), cadmium telluride (CdTe)[68,69] and copper indium gallium selenide (CIGS)[70,71] are single junction or multi junction devices. These materials are designed to be deposited on low cost substrates like glass.[72] All these above mentioned solar cells do not reach the so-called Shockley- Queisser limit. The Shockley- Queisser limit is the maximum theoretical efficiency of a solar cell using a p-n junction.

Solar cells which are manufactured in the lab constitute various semi-conducting layers where each layer is made up of a unique semi-conducting material with different band gaps. The difference in the band gaps of the semiconducting layers enable absorption of photons which belong to a section of the solar spectrum. These multi-junction solar cells absorb light from different portions of the solar spectrum to convert light into electricity. Such multi junction solar cells are also called tandem solar cells and are said to improve the solar cell performance to beat the existing Shockley- Queisser limit. Since fabrication and deposition of several semiconducting layers increases the complexity of the process, there is a huge increase in the production cost.[73]

In order to over come the rigidity of the solar cells and to venture into other possible materials for PV energy generation, a third generation of solar cells emerged. These type of solar cells are organic/polymeric/plastic solar cells,[74–76] dye sensitized solar cells (DSSC),[77] nanocrystal based solar cells,[78] quantum dot solar cells,[79] perovskite based solar cells etc.[80] Introducing such materials into solar-cell research was made to make the best of both first and second generation solar cells to gain high conversion efficiencies and low fabrication costs.

In 1977, V.M Fridkin proposed ferroelectrics as suitable materials for photovoltaic en-

ergy conversion by exploiting crystals which exhibit photo-ferroelectricity.[11,19] Photovoltaic effect in bulk polar materials, especially ferroelectrics has been discovered experimentally few decades ago,[13,81,82] and the interest revived after the discovery of large photovoltages in BFO thin films.[83,84] It was termed bulk photovoltaic effect (BPVE). Few ferroelectric and multiferroic materials like $Pb(Zr, Ti)O_3$ (PZT), $BiFeO_3$ (BFO) and $LiNbO_3$ gave large voltages when exposed to light which lead to renewed interest in photo-ferroelectrics providing a replenished momentum to the growing field of third generation solar cells.

Development of ferroelectric based photovoltaic devices has mostly been a topic for academic research.[85] High energy band gaps of ferroelectrics lead to low energy conversion efficiency. Due to this, industrial viability was not foreseen and the eventual decrease in interest over BPVE in ferroelectrics occurred. The observation of BPVE in ferroelectrics, with band gaps in the visible range was recently envisioned.[86,87] This renewed interested in this topic. Also, the physical origin and phenomenon in BPVE was recently investigated.[1,51] Hence, it is indeed the best time to study ferroelectric photovoltaics and to further understand and exploit the phenomenon.

The BPVE effect in ferroelectrics arises due to the inherent non-centrosymmetric property. The developed photovoltage is proportional to the magnitude of electric polarization and separation between electrodes, meaning the thickness of the material. It is however possible to generate large photovoltages in ferroelectrics though the photocurrent is low. New ideas like, above band gap large photovoltages,[83,84] role of domain walls,[88] effect of thin films,[89] tip enhanced PV effects[90] are being developed and the low generation of photocurrent is no more a dire concern.[9]

In this perspective, we chose lithium niobate to be the material of interest. This thesis will focus on studying the light induced phenomenon in lithium niobate and the influence of mechanical stress on its properties. Better understanding of this mechanism can provide novel ideas to improve the efficiencies of the existing solar cells and the open new windows towards better photovoltaic materials.

Part II

Experiments

Chapter 3

Experimental Details

Single crystals of lithium niobate were acquired from Deltronic Crystal Industries, Dover, NJ, USA. The samples were cubes with an edge length of 10 mm or 5 mm, with one edge parallel to the crystallographic c-direction (polar axis), and one edge parallel to the crystallographic a-direction. All the samples obtained from Deltronic were mono-domain single crystals. The crystals were grown using the Czochralski method. A photograph of the obtained single crystals is shown in Fig. 3.1.

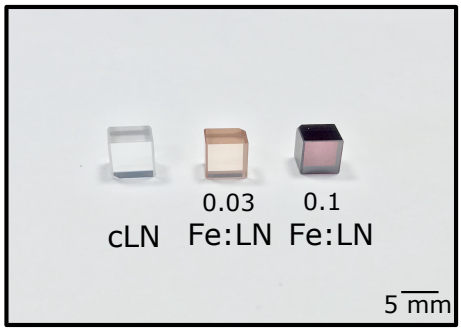

Figure 3.1: Photograph of Fe doped LN samples in with different doping concentrations given in mol %.

Mono-domain, single crystal lithium niobate samples with various metal dopants were acquired from University of Osnabrück. Similar to the iron doped samples, the dopant metal induces a colour to the transparent LN crystal. A photograph of the obtained samples is shown in Fig. 3.2

Samples doped with Fe would be mentioned from here on as Fe:LN0.03 and Fe:LN0.1 for 0.03 mol % Fe doped in LN and 0.1 mol % doped in LN respectively.

The Fe:LN cubic crystals were cleaned with an optical tissue dipped in iso-propyl alcohol (IPA) to remove any grease stains, fatty acid residues or dust which might adhere to the

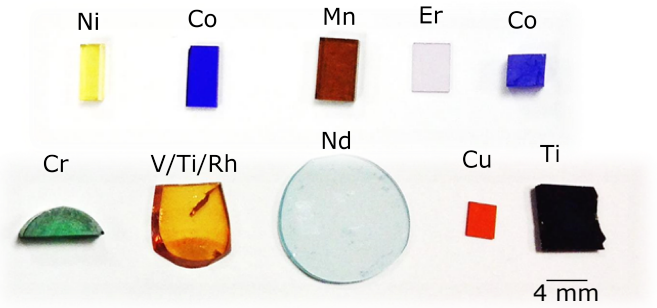

Figure 3.2: Photograph of lithium niobate crystals with various TM dopants.

sample while handling. Cleaning is performed prior to each measurement.

Samples of TM:LN were cut and polished to form a cuboid, avoiding any excess material wastage. The samples were cleaned in warm baths of IPA and washed with distilled water to remove any fatty acid residue left due to polishing and handling. Care was taken not to thermally shock the samples while cleaning which might often lead to cracking and breakage.

LN samples were electroded via different techniques. Silver particles suspended in a volatile solvent were pasted over opposite sides of the samples for electrical measurements. Gold (Au) was thermally evaporated on to the opposite sides of the crystal while masking the other sides of the sample with a Kapton (Polyimide film) tape. The Kapton tape was removed after thermal evaporation and a Q-tip dipped into IPA was used to clean the residue from the un-electroded sides of the crystal. Different electrode metals were chosen to verify if the work-function of the metal influences the generated photovoltaic current density.

3.1 Absorption spectroscopy

Optical absorption of a photon by a defect is the primary step in triggering the photorefractive effect.

The absorption coefficient $\alpha(\lambda)$ is related to the initial light intensity and transmitted intensity by:

$$I(\lambda, L) = I_0 \; exp(-\alpha(\lambda)\, L) \tag{3.1}$$

where,

λ	wavelength
L	thickness of the medium or crystal
I_0	initial light intensity
I	intensity of the transmitted beam

The absorption measurements of the crystals are of high importance. Change in the donor dopant concentration can be observed in the absorption spectra. Measurements for undoped cLN and TM-doped LN with different dimensions were conducted on a Lambda 950 UV/VIS/IR spectrometer by Perkin Elmer. Corrections for reflection were made to transmission spectra. The reflection of each sample was measured using the Universal Reflectance Accessory (URA) by placing the sample at an angle where the reflected beam aligns with the detector. The incident light intensity was kept low to avoid light-induced absorption losses of any kind. The absorption coefficients were deduced keeping in mind the dimensions of the crystal. The spectra is taken for the wavelength range 250 nm - 2500 nm with 2 nm step increase in wavelength. All the measurements were conducted at room temperature.

3.2 Secondary Ion Mass Spectrometry

The depth profiles and the elemental characterization of TM dopants in LN were obtained by Secondary Ion Mass Spectrometry (SIMS) in a CAMECA SC-Ultra under a high impact energy Cs^+ bombardment (5 keV) with beam intensity of 10 nA on a surface scan area concentrating on a spot with diameter 60 μm. Different elements of interest were measured as SIMS intensity (counts/s) over sputtering time. Identification of dopant element was retrieved as intensity and was comparable for different dopant concentrations in the sample.

3.3 X-ray diffraction

XRD measurements were performed on Bruker D8 discover (series II) diffractometer comprising a 4 - axis Eulerian cradle. It is configured to be used in parallel beam configuration due to the use of a Goebel mirror. The emitted beam height is set to 1.2 mm. The sealed tube comprises of a Cu anode emitting k_α x-rays. The tube - sample distance in this case was fixed to 300 mm. The detection system consists of a 0-dimensional scintillator detector. The $\theta/2\theta$ symmetrical measurement was performed from 5° to 80° in 2θ, with a scan step size of 0.05° and an acquisition time of 5 s per step.

10 mm^3 samples were placed on the sample holder. The crystal was turned before each measurement to retrieve a diffractogram for each face of the crystal.

3.4 Electron Paramagnetic Resonance

The following description of EPR is based on the book by Eaton G R on Quantitative EPR.[91]

The principle of EPR is based on the interaction of an unpaired electron in the sample with the external magnetic field applied B_0. The effect is famously called the Zeeman effect. A single unpaired electron has only two unpaired electron states. When the moment of the electron μ is aligned with the magnetic field, it would be in a state of lower energy or a higher energy. The two states are designated by the projection of the electron spin, m_s on the direction of the magnetic field. Since an electron is a spin $1/2$ particle (the parallel state as $m_s = -1/2$ and the anti-parallel state has $m_s = +1/2$), the difference in energies ΔE is

$$\Delta E = g\mu_B B_0 \Delta m_s = g\mu_B B_0 \tag{3.2}$$

where g is the g -factor and μ_B the natural unit of the electrons magnetic moment of the Bohr magneton, Δm_s is the change in the spin state.

The lines in the EPR spectra are essential to quantify the spin order of a metal ion. The general rule is that the number of lines is equal to $2n + 1$, where n is the number of symmetry equivalent nuclei. If for an ion, $n = 5/2$ the coupling to this ion gives six hyperfine lines. However, the size of the EPR signal is important for measuring the concentration of EPR active species in the crystal. The size of the signal, is defined as the integrated intensity, which is the area beneath the absorption curve. The integrated intensity of an EPR signal is proportional to the concentration of unpaired electrons in the sample.[91]

EPR measurements were performed using a continuous-wave EPR spectrometer EMX, Bruker, equipped with a cylindrical TE112 resonator. These measurements were conducted at continuous wave X-band 9.8 GHz frequency. All EPR measurements were performed at room temperature. A schematic set up of the EPR spectrometer is shown in the Fig. 3.3.

A typical Bruker EPR spectrometer contains a microwave source, an attenuator or a modulation input, a phase-sensitive detector, a diode detector, and a sample cavity surrounded by an electromagnet as shown in the Fig. 3.3. EPR reflection spectrometer measures changes due to transitions in the amounts of radiation reflected back from the cavity which contains the sample. The diode detects the microwave radiation reflecting back from the cavity. Bruker spectrometers use a Schottky barrier diode to detect the reflected microwaves, which is converted into a DC electric current. To ensure optimal sensitivity and excellent signal intensity, this diode operates in a linear region, where the microwave power is proportional to the square root of the voltage or current. To ensure that the detector also operates in the linear region, a reference arm has some

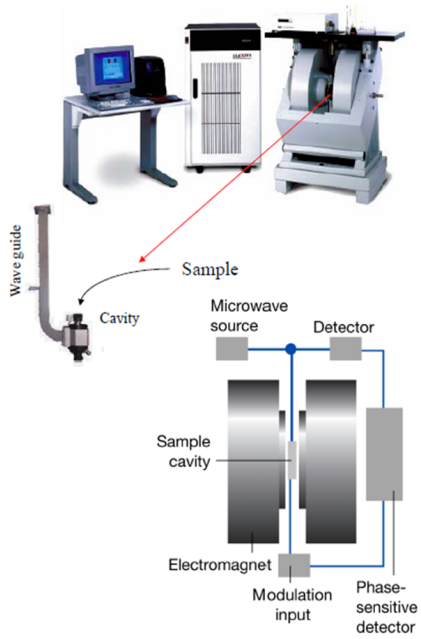

Figure 3.3: Schematic set-up of the EPR spectrometer.

of the source power tapped off where an attenuator controls the power level. A phase shifter ensures that the reference wave is in phase with the reflected signal. The detector diode hence combines both the reference wave and the wave which passed the cavity containing the sample to provide an EPR signal. The resultant spectrum is hence EPR intensity over increasing magnetic field. EPR technique was employed in this case to detect unpaired electron spins of transition metal ions doped in the crystals, to examine the site symmetry of the transition metal complex Fe^{3+} and light induced centres.

The Fe:LN samples with different dopant concentrations were chosen and were cut into 1 mm^3. The samples were cleaned and were placed in a quartz tube with a diameter of 1.3 mm which was then carefully placed in the cavity which is surrounded by an electromagnet. In order to measure for axial symmetry of EPR active Fe^{3+} ions in the spectra, the quartz tube was gently rotated to match the angles marked on a plate attached to the cavity. The crystal was placed such that the polar c axis coincides with the z axis of the lab, and the a axis to the x axis of the lab. The rotation patterns of the resonance fields for Fe^{3+} ion in LN were obtained on zx - (crystallographic ca) planes. In order to measure light-induced EPR, direct illumination of the sample was achieved by placing a 532 nm continuous wave laser in front of the cavity. The beam diameter from the laser covered the entire sample surface. A hand held photo-diode was used to measure the power which was in the range of 13 to 17 mW, which was then converted to intensity by noting the area of illumination. EPR spectra with and without illumination is taken to determine light-induced increase of trap levels in Fe:LN.

3.5 Dielectric Spectroscopy

Dielectric spectroscopy was conducted on 0.01 mol% Fe:LN and 0.03 mol% Fe:LN using a Novocontrol Concept 40 Dielectric Spectrometer with a ZGS alpha active sample cell. Preliminary measurements indicated that it did not matter if or with what material the sample was electroded for the dielectric measurements. Therefore, the samples were typically measured without applying any additional electrode. For the measurement, the samples were placed between two gold-plated brass discs that served as sacrificial electrodes to avoid contamination of the sample holder. A spring ring was placed between the top brass plate and the upper plate of the sample holder to compensate sample expansion due to piezoelectricity or thermal expansion. This was necessary, as a stress exerted by an expanding sample of high stiffness onto the measurement setup might damage the insulating silica parts in the active sample cell, destroying the electrical insulation and making measurements at high impedance impossible. As all samples were smaller than the diameter of the electrode discs of 20 mm, the sample diameter entered into the analysis software was always set to 20 mm, i.e., the diameter of the disc. The difference between sample surface area and brass disc area was then entered as 'spacer area' into the software. The capacitance of this spacer area was manually calculated using the formula of a parallel plate capacitor, using the sample thickness as thickness of the capacitor, this value was entered as 'spacer capacitance' into the software. The spectrometer measured the real and imaginary part of the total impedance of the setup, equivalent to the capacitance and resistance. By subtracting the spacer capacitance from this measured capacitance, the sample capacitance is obtained. Based on the active sample area and thickness, the dielectric permittivity is automatically calculated by the program. Real and imaginary part of the permittivity were measured in the frequency range from 1 Hz - 1 MHz with an ac field amplitude of 1 V/ms. Frequency was varied on a logarithmic scale, with a factor of 1.01 between the frequencies of adjacent data points, for a total of 1390 data points in each measurement.

3.6 Photovoltaic measurements

3.6.1 Bulk-photovoltaic measurements

A typical measurement set-up in order to obtain j_{sc} values under illumination is shown in Fig. 3.4.

A series of diode lasers from Changchun New Industries Optoelectronics Technology Co., PR China with wavelengths 450 nm, 473 nm and 532 nm were selected. In order to orient/filter the light electric polarization of the wave emitted by the laser, a polariser (GL10-A, with an anti-reflective coating: 350 - 700 nm from Thorlabs GmbH, Dachau, Germany) was used. This polariser was mounted over a stand to enable rotation. The rotation mount was chosen to achieve selected light electric polarisation with respect to the crystallographic axis. A half-wave plate (AHWP10M-600) was placed between

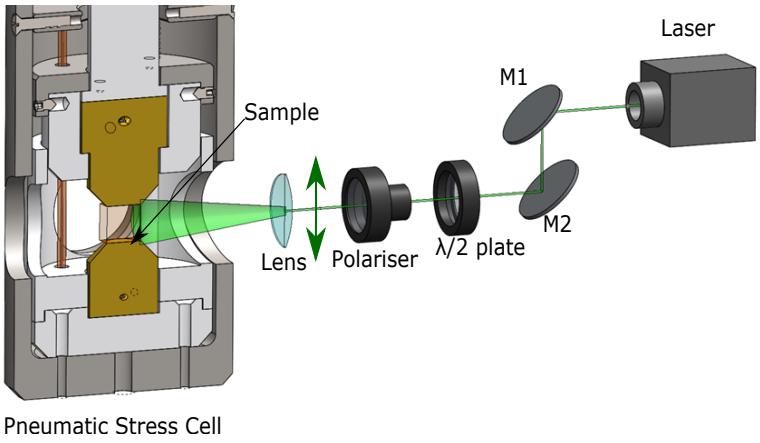

Figure 3.4: Schematic of the measurement set-up for stress modulated BPVE, with a cross-cut view of the pressure cell.

the polariser and the laser to enable control over light intensity. A plano-concave lens (N-BK7 from Thorlabs GmbH) is used to further expand the beam to homogeneously illuminate the surface of the crystal. A photo-diode is (S120C, Thorlabs GmbH) connected to a hand-held power sensor (PM100D, Thorlabs GmbH) was placed before the sample to measure the light power modulated by the half-wave plate. The modulated laser power was noted by switching the laser on before each measurement. An iris was attached to the Si photo-diode which had a fixed diameter. The intensity of illumination is given by dividing laser power by the area of the iris. LN crystals which were congruently melting and TM-doped were placed directly in the sample holder which had brass electrodes built into it. In order to measure the influence of work-function of an electrode over photovoltaic current, silver electrodes were pasted on opposite sides of the sample and gold electrodes were thermally evaporated on opposite sides of the crystal. Short-circuit current was then measured with a Keithley 6514 electrometer. The values of short-circuit current were recorded for an extended period of time in order to have a saturated value. The short-circuit current density was taken by dividing the recorded values of short circuit current by the area of the electroded surfaces.

3.6.2 Piezo-photovoltaic measurements

A pneumatic air-pressure operated stress cell designed and assembled in house was used to measure stress induced photovoltaic effect. A schematic of the measurement set-up is shown in the Fig. 3.4. The stress cell constitutes of an air pressure controller, a pressure actuator, a pressure reducer, a strain gauge and a display unit. A soft-start valve (Festo pressure HE D-Mini DD43) is connected to a filter regulator (LFR-D-Mini-DD43) which is then connected to the air valve to determine the initial input air pressure. A proportional pressure regulator (Festo VPPM) is used to apply suitable pressure to the

pressure actuator (EB-165-65) mounted horizontally on the system to enable direct load on to the brass cast ingot in contact with the sample. The air is pumped into the actuator through a power valve (Festo VL/0-3-1/4). The pressure actuator can apply stress up to 10 kN with an air pressure of 8 bar. The actuator is attached to a gauge (Sensy, alloy steel model 2965) which is connected to a display unit (Sensy DISP-PAXDP) programmed to display force in kN with 10^{-1} kN accuracy. A bottom electrode is a brass cast which is attached to a nut mount placed at the bottom, to enable sample positioning. The total stress depends on the air pressure and the dimensions of the sample. Stress is regulated by controlling the air pressure. The loading and unloading rates are of minor importance as measurements under constant static stresses are conducted.

LN crystals doped with TM ions, cleaned with ethanol or IPA and wiped with an optical tissue, were placed in between the brass electrodes. Since BPVE is orientation dependent, measurable components of the BPVE for 3m symmetry of LN were chosen. The faces which are in contact with the metal electrodes determined the direction of measured short-circuit current.

A static load was applied on the samples with pressure ranging from 0 - 10 MPa. Higher stress are avoided to prevent crushing or cracking of the single crystal samples. The same set-up used to measure the BPV current was arranged to illuminate the sample placed in the stress-cell. The BPV current at increasing intensities, for different wavelengths, were investigated at increasing stress levels. For components where the direction of uniaxial stress differed from the direction of short-circuit current, silver electrodes were pasted and the current was measured with aide of a metal clamp attached firmly with help of a copper tape(with a conductive adhesive) which was then connected to the Keithley 6514 electrometer.

In order to determine the contribution of leakage via edges of silver pasted electrodes to the metal casts of the stress cell, measurements of BPV components were taken (where stress = 0 MPa) and the sample was reoriented and attached to the metal clamp while the face perpendicular to it was in contact with the metal cast. The values were then compared, which were in the error margin of the measurement. This showed that there was little contribution of leakage current for the components measured.

3.7 Raman spectroscopy

The Raman measurements were performed on a Renishaw inVia Raman Microscope. A schematic of Raman microscope is given in the Fig. 3.5.

The following description of Raman spectrometer is based on a Thesis written by M C Weber at University of Luxembourg in 2017.

The Raman spectrometer used has a He-Cd laser source for wavelengths 325 and 442 nm and a frequency doubled Nd:YAG laser for 532nm. The monochromatic beam generated

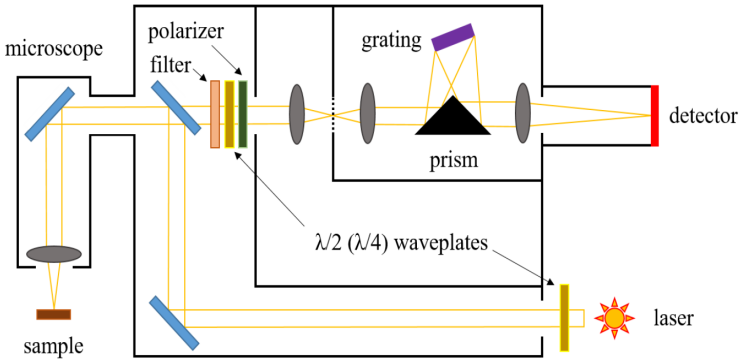

Figure 3.5: Schematic of the Renishaw in-Via confocal Raman microscope. (Taken from the thesis of M.C.Weber (2016)[92])

from this source is focussed on the sample through a optical Leica microscope attached with a camera. The optical microscope can be set at various magnifications and apertures by varying different lenses to attain the best setting to focus the beam on the surface of the sample. The sample surface and the focused beam can be visualised through a display attached to the output of the camera. The incident beam after hitting the surface of the sample is scattered back and takes the same path as the incident light. The polarization of the laser can be rotated to 90° such that the analysed or the scattered light is parallel or perpendicular to the direction of the incident laser beam. A built in Silicon sample is used for calibration. The Rayleigh peak is filtered with spectral cut-offs at 80 cm^{-1} (green) or 95 cm^{-1} (blue). After filtering, the scattered light is dispersed through a grating into a CCD (Charged Coupled Device) for spectral data processing and is displayed digitally for further analysis.[92]

A correct interpretation of the Raman spectra is provided by a Porto notation that depicts the orientation of the crystal axes with respect to the polarization and propagation direction of the incident and scattered laser light.

$$A(BC)D \tag{3.3}$$

where A and D are the directions of propagation, and B and C are the directions of polarization of the incident and the scattered beams respectively. In a backscattering geometry, an overline indicates that the incident and the analysed light propagate in opposite directions, example $A(BC)\bar{A}$. The directions A-D are usually given with respect to axes linked to the spectrometer. If the crystal orientation is known, they can be expressed in a suitable crystallographic system which can be used for application of the Raman selection rules and determination of the mode symmetries.

For R3c symmetry, in hexagonal axes system, the detectable Raman modes are A - fully

symmetric vibrations (modes that are symmetric with respect to rotation around the principle rotational axis which are 1D representations) and E - doubly degenerated vibrations (modes which are degenerate or 2D representations where there are two wavefunctions for every single energy state). According to the selection rules, four Raman-active A modes and eight Raman-active E modes exist for R3c symmetry.

Fe:LN0.03 and Fe:LN0.1 cubes were placed on the sample holder right below the optical microscope. The laser beam was focused on the sample with a chosen direction of polarization to achieve a specific Raman spectra. In order to measure the effect of stress on the phonon modes, a portable mechanical table top stress cell was used. The sample was placed in between the plates and a static uniaxial stress was applied on the crystal. The portable stress cell was placed below the microscope and the same technique was used to retrieve the Raman spectra for different stress levels.

Chapter 4

Investigation on lithium niobate - Results

4.1 Basic characterization

4.1.1 X-ray diffraction

In order to perform BPV measurements, it is essential to determine the orientation of the faces of the obtained crystal, which was confirmed by XRD. X-ray diffractograms of Fe:LN0.03 cube with dimensions 10 mm are shown in Fig. 4.1.

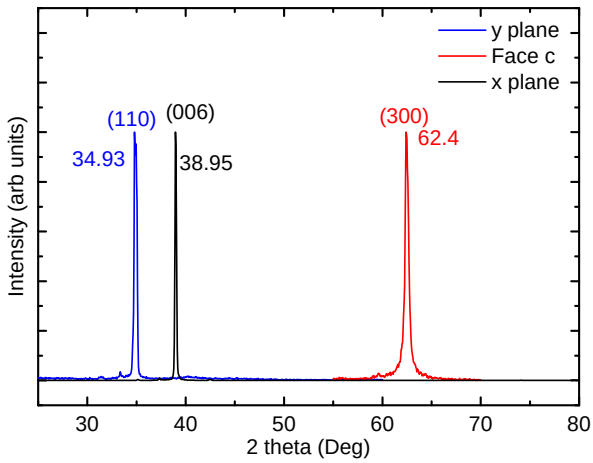

Figure 4.1: X-ray diffraction of single crystalline Fe-doped lithium niobate cube. The polar +c-axis of the crystals is represented by the peak (006). Peaks (110) and (300) represent faces orthogonal to the diffractogram obtained for face (006).

Figure 4.1 is a typical profile of a single crystal LN and matches the powder diffraction file data available for lithium niobate. The powder diffraction file number used to check the orientation of the sample is 04-009-8335, from ICDD PDF4+ v4.19 (2019) database. The samples provided were cuboid in shape and the polar c-axis of the crystal is parallel to the z coordinate axis of reference. The c face is the face perpendicular to the polar axis of the crystal.

It is essential to know the orientation of other faces of the sample. X-ray diffractograms of all the faces were taken to retrieve six diffractograms, where one intense peak for each face was obtained marking the orientation of the crystal. The faces which were opposite to each other gave the same peak.

Peak at 38.95° on the 2 theta x-axis in the diffractogram represents (006) the c face of LN. The peaks at 34.93° and 62.4° on the 2 theta x-axis represent b (110) and a (300) faces respectively. The sharp peaks in the diffractogram represent a homogeneous single crystalline material.

4.1.2 Secondary Ion Mass Spectrometry

Elemental analysis of TM dopant in LN was verified by conducting dynamic Secondary Ion Mass Spectrometry (SIMS) on LN crystals doped with Cobalt (Co), Manganese (Mn) and Nickel (Ni), with undoped cLN as a reference sample. Figure 4.2a shows the secondary ions generated from the samples as intensity in counts/seconds. The increase in dopant concentration of Co from 0.19 wt% to 0.25 wt% reflects as an increase in SIMS intensity as shown in Figure 4.2b.

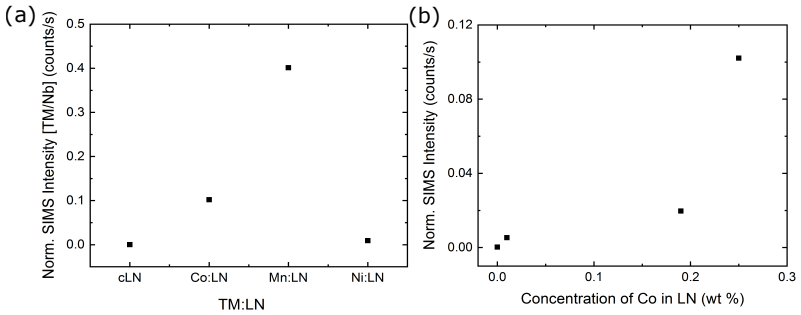

Figure 4.2: SIMS on lithium niobate doped with TM ions (a) Identification of TM ions and their inclusion measured in counts/s. The y-axis shows normalised values of the ratio of TM ions over niobium ions in the sample (b) SIMS intensity profile with increase in dopant concentration for Co:LN. The y-axis is represents normalised values of intensity of Co/Nb and the x axis represents the amount of Co in wt % in LN.

4.2 Spectroscopic techniques

4.2.1 Absorption spectroscopy

Congruently melting LN (cLN or undoped LN) is transparent in the visible wavelength range. It is the TM dopant elements in LN which induce colour into the crystal. The absorption spectra in Fig. 4.3 show the absorption coefficient α of cLN and Fe-doped LN measured in transmission for 300 nm $\leq \lambda \leq$ 750 nm. The absorption lines of Fe-doped LN samples differ from the spectra of cLN showing peaks in the visible region of the spectra.

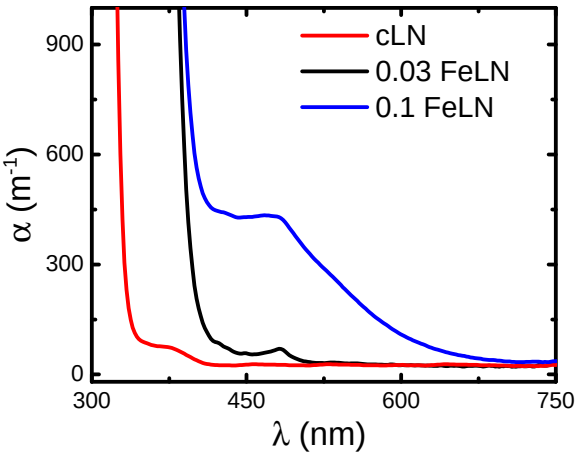

Figure 4.3: Absorption spectra of congruently melting lithium niobate (cLN), Fe:LN0.03 and Fe:LN0.1.

A wide absorption band appearing in the 450 nm -550 nm region for the samples doped with 0.03 mol% Fe is noticed which differ from the spectra of cLN. With increase in doping concentration of Fe from 0.03 mol% to 0.1 mol%, the absorption band widens in 450 nm - 550 nm region with enhanced absorption coefficients. The absorption in the doped samples peak at around 470 nm and α increases strongly at the fundamental band edge, corresponding to a wavelengths of approximately 370 nm for Fe doped LN and 315 nm for cLN. A slight shift in the fundamental band edge is observed with increasing doping concentration. The absorption coefficients of Fe:LN0.03 and Fe:LN0.1 at wavelengths λ = 450, 473 and 532 nm are given in the table 4.1.

Absorption spectra of LN with different dopant elements is given in Fig.4.4 and the corresponding dopant concentrations of TM in LN are given in the table 4.2.

Absorption peaks for different dopants in LN shown in table 4.2 indicates the energy at which an electron can be excited to eventually participate in charge transport. For Co:LN, a broad peak in the green region is evident with large absorption coefficient at

λ	α for Fe:LN0.03	α for Fe:LN0.1
nm	m^{-1}	m^{-1}
450	60	431
473	63	433
532	33	273

Table 4.1: Absorption coefficients of Fe:LN0.03 and Fe:LN0.1 at wavelengths λ = 450, 473 and 532 nm.

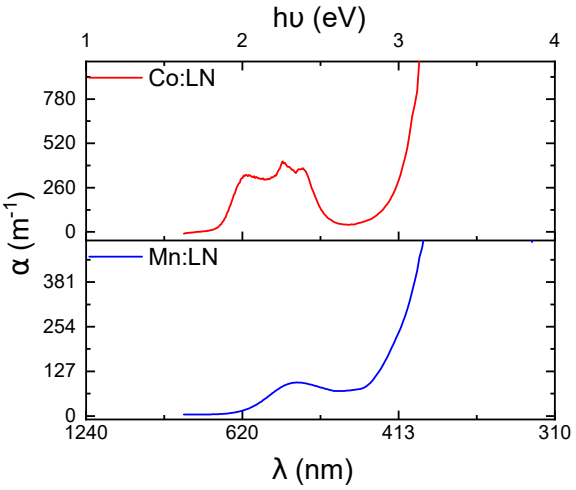

Figure 4.4: Absorption spectra of different TM-doped LN samples.Top: 0.19 mol% Co:LN and bottom: 0.5 mol% Mn:LN.

λ = 538 nm. Another TM dopant active in this region is Mn where a broad absorption with a peak at λ = 573 nm is observed.

4.2.2 Electron paramagnetic resonance

Fe occurs in two oxidation states in LN, Fe^{2+} and Fe^{3+}. EPR spectroscopy determines the concentration of Fe^{3+}, which would indirectly contribute to the charge generation under illumination. The contribution of Fe in LN is explained in section 2.4.2.

Absorption bands do not entirely indicate the concentration of defect centres in the crystal. The concentration of the defect centres and their valence state can be estimated via electron paramagnetic resonance (EPR) spectroscopy. Since EPR is an effective tool for probing ions with unpaired electrons such as Fe^{3+}, it is used to investigate the oxidation state and the site incorporation of Fe in LN.[93]

For Fe^{3+} ion having electron configuration $3d^5$ with electron spin S=5/2, the ground-state configuration can be written as ${}^6S_{5/2}$. When this ion is embedded in the crystal, it experiences an intense crystal field produced by the neighbouring ions.[94] Consequently,

TM ion	Dopant conc.	λ	E	α
	mol%	*nm*	*eV*	m^{-1}
Co	0.19	516	2.4	364
Co	0.19	538	2.3	402
Co	0.19	590	2.1	334
Mn	0.5	516	2.4	666

Table 4.2: Absorbance for various TM dopant elements in LN.

a fine structure arises in the EPR for the Fe^{3+} ion from the crystal field and spin-spin interactions. The lines of the EPR spectra observed in Fig. 4.5 are for Fe^{3+}_{Li} which are similar to the ones shown in literature.[94] The lines for the ion Fe^{2+} are spectroscopically not observable since the microwave frequency used here is low (9.8 GHz). Such paramagnetic high-spin states which are observable at higher frequencies are termed 'EPR-silent' states such as Fe^{2+} ($3d^6$, S=2) states.[95]

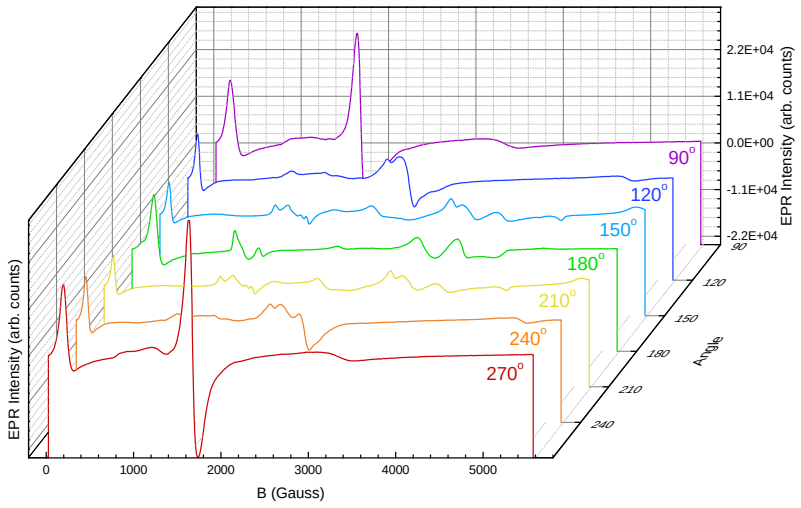

Figure 4.5: EPR spectra of Fe:LN0.01 at various angles.

Since Fe^{3+} centre is a cation site with C_3 symmetry replacing the Li^+ site, EPR spectra of Fe:LN show an orientation dependence of the axial EPR active transition metal centre, shown in Fig. 4.5 for Fe:LN0.01 sample. The orientation dependence of the TM centre is obtained by rotating the sample with 30° steps and measuring the EPR spectra. The crystal cut and polished to 1 mm^3 was placed in a quartz tube with its polar c axis coinciding with the z axis of the lab, and the a axis to the x axis of the lab. The rotation patterns of the resonance fields for Fe^{3+} ion in LN were obtained on zx - (crystallographic ca)

planes. Figure 4.5 shows the axial symmetry of the Fe^{3+} ions incorporated in the lattice confirming the C_3 site symmetry. The peak observed between 1000 - 2000 Gauss depicts the Fe^{3+} ions replacing the Li site. EPR studies have shown that the dominant Fe centres in LN have axial symmetry with a zero-field splitting about 1680 Gauss[94,96,97] which corroborates with the EPR lines which are observed here.

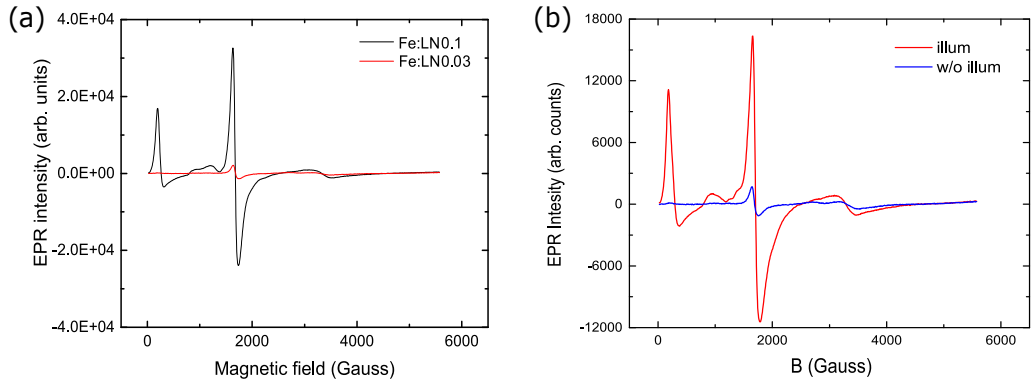

Figure 4.6: EPR spectra (a) EPR lines of Fe:LN0.03 and Fe:LN0.1 (b) EPR spectrum of Fe:LN0.03 without illumination compared to the spectrum under illumination.

The concentration of Fe^{3+} ions for two different dopant concentrations, 0.03 mol% and 0.1 mol% Fe in LN reflects in the EPR hyperfine lines. This is shown in Fig. 4.6(a). When compared, the intensity of EPR line for Fe:LN0.1 (LN with higher Fe concentration) dominates the EPR line intensity of Fe:LN0.03.

EPR spectra for Fe:LN0.03 with and without illumination at wavelength $\lambda = 532$ nm, with intensity in the range of 60 ± 5 Wm^{-2} is shown in Fig. 4.6(b). The increase in the intensity of the peak representing the Fe^{3+} ions is a visual evidence of increase in concentration of Fe^{3+} traps due to photo-excitation.

4.2.3 Dielectric spectroscopy

In the Fig. 4.7 the real part ϵ' and imaginary part ϵ'' of the permittivity, of Fe:LN with two different doping concentrations measured along the polar axis of the crystal at frequencies ranging from 1Hz - 1MHz are given. It is clear from the dispersion curve that ϵ' and ϵ'' increase with increasing dopant concentration. Constant values for ϵ' and ϵ'' starting from 1 Hz which ends at 10 kHz are observed. The peaks occurring at 10 kHz to 0.11 MHz represent piezo-resonances.

4.3 Bulk-photovoltaic measurements

With illumination, LN generates a current which is measured under short-circuit conditions.

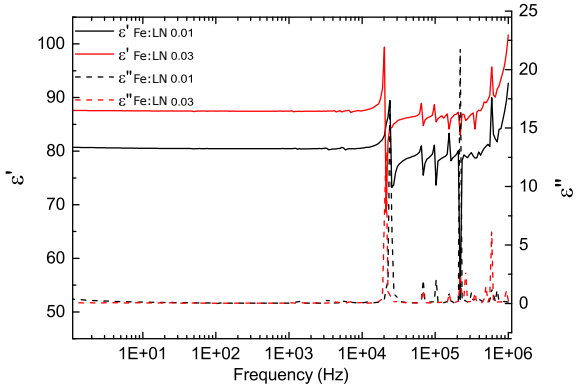

Figure 4.7: Dielectric spectroscopy on Fe:LN0.03 and Fe:LN0.1.

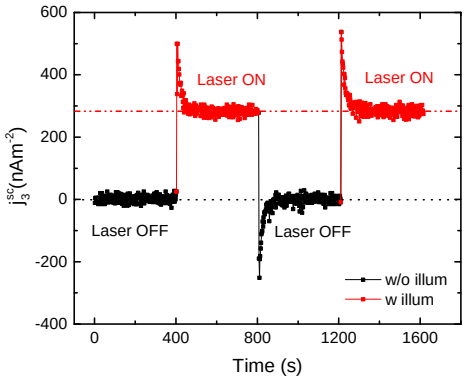

Figure 4.8: Short circuit current density in Fe:LN0.03 measured along the polar axis with and without illumination where light electric field is parallel to the polar axis of the crystal.

Short-circuit current measured along the polar axis by illuminating Fe:LN0.03 crystal at wavelength $\lambda = 450$ nm with 98 Wm^{-2} intensity with the light polarization direction parallel to the polar c-axis of the crystal is shown in Fig. 4.8. The measurement shows current generated with and without illumination. The y-axis in the Fig. 4.8 shows the current density measured along the polar c-axis. The peak in the positive direction of the y-axis in the measurement is due to the fact that the crystal, Fe:LN falling into the pyroelectric class, is heating when under illumination. The current eventually stabilises when the heat dissipates. This saturated value is taken as the photovoltaic current density. The peak in the negative direction of the y-axis of the crystal occurs due to sample being cooled when the laser is switched off. Similarly, the change in temperature stabilises giving a constant value for the current. This transient behaviour lasting approximately 1 min reasons less with the theory that illuminating LN causes transient

electronic behaviour. The stabilised value of light-induced current after illumination is represented by a horizontal line which is higher with respect to the line without illumination. The short raise in the current due to heating when under illumination is caused by change in the polarization caused by internal electric fields (the pyroelectric effect). The values of j_{sc} are taken after pyro-current stabilization which occurs due to thermal dissipation of the heat induced by optical absorption.

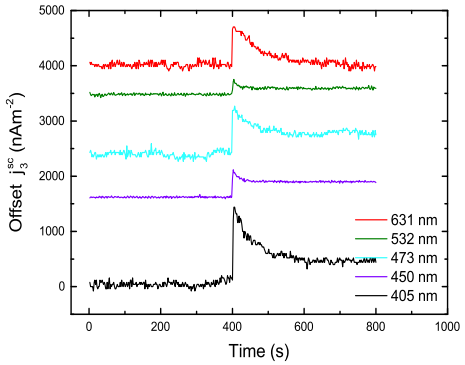

Figure 4.9: Observation of pyroelectric current density by illumination of Fe:LN0.03 doped LN at different wavelengths.

The pyro-current observed varies with energy of a photon being absorbed by the sample. Figure 4.9 shows the effect of illumination wavelength on the pyro-current. The pyro-current at different wavelengths measured at 98 Wm^{-2} for Fe:LN0.03 are given in the Fig. 4.9. The number of photons multiplied by the absorption coefficients ς is $\varsigma^{405\text{nm}} = 1.25 \times 10^{14}$, $\varsigma^{450\text{nm}} = 3.74 \times 10^{14}$, $\varsigma^{473\text{nm}} = 3.72 \times 10^{14}$, $\varsigma^{532\text{nm}} = 8.03 \times 10^{14}$ and $\varsigma^{631\text{nm}} = 1.30 \times 10^{15}$. The high pyro-current observed for 631 nm could be related to the value of $\varsigma^{631\text{nm}}$ which is higher when compared to other wavelengths.

Fe doping conc.	α.	Pyro-current
mol%	m^{-1}	*pA*
0	25	8
0.01	32	28
0.03	59	70
0.1	430	186

Table 4.3: Light induced pyroelectric current in Fe:LN at wavelength 450 nm.

Absorption is induced in the crystal at specific wavelengths due to the defect centre (Fe_{Li}^{2+} in this case). The increase in pyro-current with respect to the doping concentrations for undoped cLN, 0.01 mol%, 0.03 mol% and 0.1 mol% Fe:LN is shown in Fig.

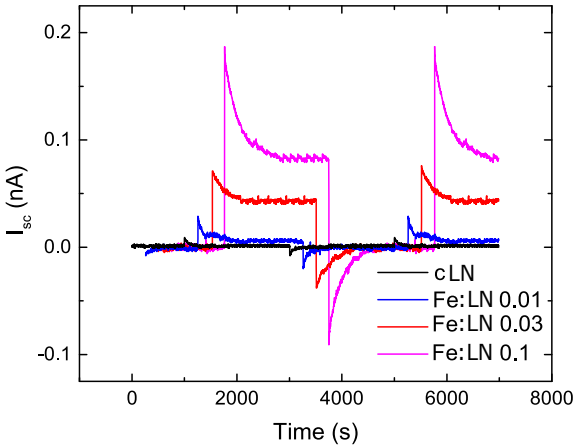

Figure 4.10: Influence of dopant concentration on short-circuit current with and without illumination.

4.10. This is a typical short-circuit measurement with and without illumination at wavelength 450 nm. Increase in the doping concentration increases the absorption coefficient, which reflects in the pyro-current generation. The values of the pyrocurrent which is, the sudden increase in short-circuit current with illumination before thermal stabilization for cLN, Fe:LN0.01, Fe:LN0.03 and Fe:LN0.1 are given in the table 4.3. Pyroelectric coefficient p_i for the LN crystals show an increase with doping concentration. The values of the pyroelectric coefficients are taken from the literature, p_3 at $50°C$ for cLN is 7.2×10^{-5} Cm^{-2} $°C^{-1}$ and that for 0.4 wt % Fe:LN is 33.8×10^{-5} Cm^{-2} $°C^{-1}$.[98] From the equation 1.9, the change in temperature with illumination is calculated. The change in temperature with illumination is 0.14 °C for cLN, 0.4 °C for Fe:LN0.01, 0.6 °C for Fe:LN0.03 and 2.9 °C for Fe:LN0.1. This shows that the absorption coefficient and the defect centre plays a role in the pyrocurrent generation. Heat is dissipated either through the metal electrodes or ambient air. Once the heat is dissipated in the crystal, a stable short-circuit current is observed in the measurement while under illumination which is the photovoltaic current.

Effect of wavelength on BPVE

Intensity dependence of the short-circuit current for Fe:LN0.03 for different excitation wavelengths is shown in Fig. 4.11.

The short-circuit current density increases linearly with intensity of illumination independent of wavelength. The slope between j_{sc} and I is the BPVE tensor/coefficient for each specific wavelength. It is observed that β_{333} doesn't linearly scale with α. The ratio $\zeta = \beta_{333}/\alpha$ for different wavelengths is given as $\zeta_{450nm} = 50 \pm 1.2$ $pAmW^{-1}$, $\zeta_{473nm} = 35 \pm 1.8$ $pAmW^{-1}$ and $\zeta_{532nm} = 32 \pm 0.3$ $pAmW^{-1}$.

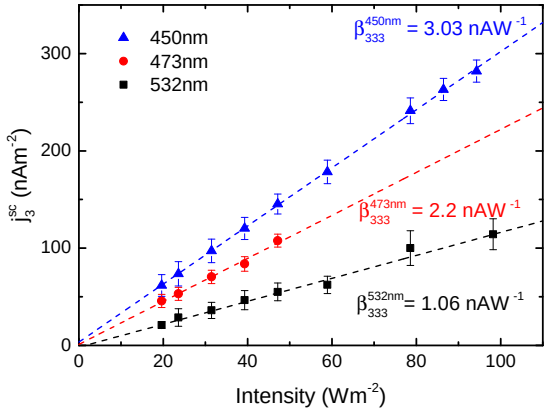

Figure 4.11: BPVE in Fe:LN0.03 at different wavelengths.

Effect of orientation on BPVE

Components other than β_{333} can be measured by changing the orientation of the sample in the sample holder. When the current is measured orthogonal to the polar c-axis, the first index of the BPVE tensor becomes 2. By changing the light polarization direction, the second and the third indices of the BPVE tensor become 22 for ordinary and 33 for extraordinary. BPVE components with different orientations can then be summarized as, for ordinary light polarization direction ($\varepsilon_2\varepsilon_2^*$) β_{322} & β_{222} and for extraordinary light polarization direction ($\varepsilon_3\varepsilon_3^*$) β_{333} & β_{233}. Fig. 4.12a, displays a schematic for such measurements. The BPVE third-rank tensors components which can be deduced are displayed above each schematic. The light polarization directions both ordinary and extraordinary are given with respect to the polar axis of the crystal. Depiction of light polarization directions for the components are drawn above the reference axis, where for each component, the light polarization direction is placed inside the crystal schematic in comparison to the polar c-axis of the crystal. The components β_{333}, β_{322} and β_{222} are shown in the Fig. 4.12b for Fe:LN0.03 for the excitation wavelength 450 nm.

The BPVE coefficient measured along the polar c-axis are higher in comparison to the coefficient measured orthogonal to it. Also, β_{333} with light polarization direction parallel to the polar c-axis is observed to be higher than the component β_{322} where the light polarization direction is orthogonal to the c-axis.

The zero and non-zero components for the third rank tensor β_{ikl} for 3m symmetry are given in the section 2.4.3. Effect of symmetry on BPVE tensor components is tested by measuring the component β_{233} and is compared to the component measured along the same axis with the light polarization direction perpendicular to the polar c-axis, which is component β_{222}. This is given in the Fig. 4.13. According to symmetry conditions, the component $\beta_{233} = 0$. However, a value for β_{233} is observed which can be attributed to a

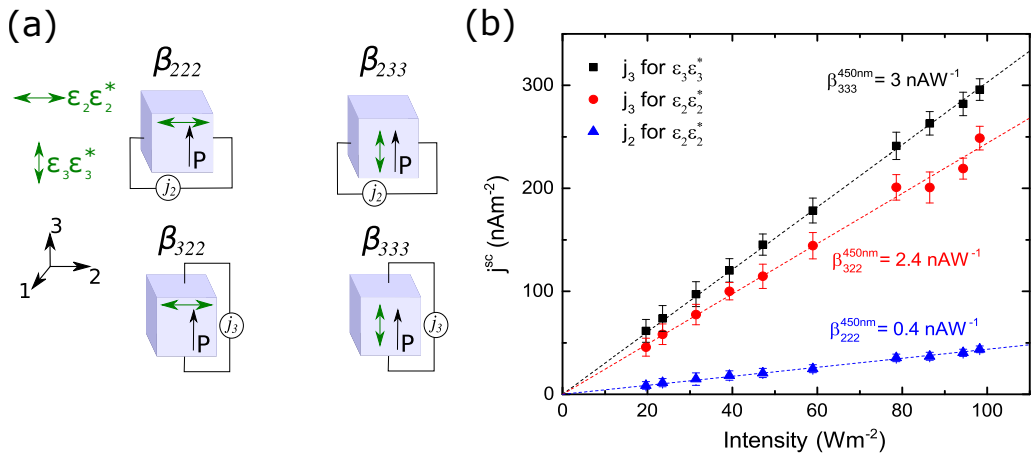

Figure 4.12: Effect of orientation on BPVE components for Fe:LN0.03. (a) A schematic showing extraction of different components of BPVE with respect to the polar c-axis of the crystal (b) Corresponding measurements of components β_{333}, β_{322} & β_{222} for Fe:LN0.03 at excitation wavelength λ= 450 nm.

mis-cut in the crystal or due to inhomogeneous light illumination.

The values for Fe:LN0.03 for different wavelengths and measurable orientations are given in the table 4.4.

β_{ikl}	i	kl	λ = 450 nm	λ = 473 nm	λ = 532 nm
β_{333}	3	33	3.03 ± 0.02	2.2 ± 0.12	1.06 ± 0.04
β_{322}	3	22	2.43 ± 0.01	1.64 ± 0.01	0.44 ± 0.03
β_{222}	2	22	0.43 ± 0.01	0.29 ± 0.01	0.14 ± 0.01
β_{233}	2	33	0.14 ± 0.01	0.17 ± 0.04	0.13 ± 0.04

Table 4.4: BPV components measured for Fe:LN0.03 at different wavelengths. The values of β are given in nAW^{-1}.

All the values of BPVE components given in table 4.4 are rounded off to the second decimal. The component β_{233} which theoretically equals zero for 3m symmetry, gives values for different wavelengths. The value observed for different wavelengths for this specific component might arise due to misalignment of the crystallographic axes with respect to the sample edges. Irrespective of wavelength of excitation, the values of the components are in the order $\beta_{333} > \beta_{322} > \beta_{222} > \beta_{233}$ for Fe:LN0.03 sample.

Effect of work-function of metal electrode on BPVE

To determine a possible influence of the electrode material on the measured short circuit current, measurements of BPVE were performed on Fe:LN0.03 at 532 nm illumination

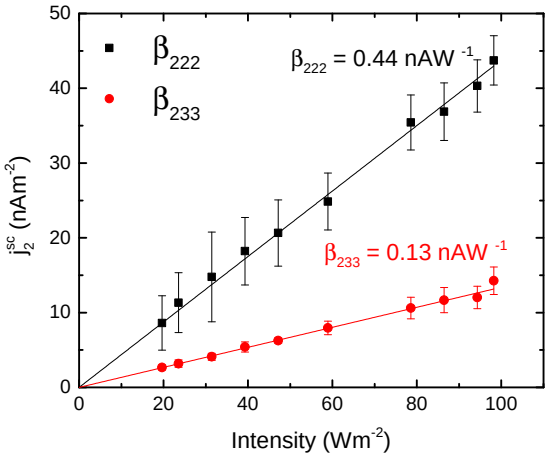

Figure 4.13: Comparison between component β_{233} which theoretically equals to zero and a non-zero component β_{222} measured at excitation wavelength λ= 532 nm.

wavelength coated with different metal electrodes. Figure 4.14 shows values for samples with Ag (Silver pasted), Au (Thermal evaporated) and brass. The work-function of Au is 5.1 eV, Ag = 4.3 eV and that for brass is 4.5 eV. The β_{333} values for these electrodes are ${}^{Brass}\beta_{333} = 1.06\pm0.04\,\mathrm{nAW}^{-1}$, ${}^{Ag}\beta_{333} = 1.18\pm0.09\,\mathrm{nAW}^{-1}$ and ${}^{Au}\beta_{333} = 1.25\pm0.12\,\mathrm{nAW}^{-1}$ with negligible difference considering that the short-circuit current density values with increasing intensities for all the electroded samples are in the range of the error margin. Also, the values of β_{333} for samples of different electrodes do not depend over the work-function of the metal electrodes. Hence this proves that BPVE is not an interface effect.

Effect of TM doping concentration on BPVE

The bulk photovoltaic current density, j_{phv} is proportional to $I/[N_{Fe^{2+}}]$. Here $[N_{Fe^{2+}}]$, is the concentration of Fe^{2+}.

To test the dependence of BPVE on the doping concentration of Fe, the BPV coefficients for Fe:LN0.03 and Fe:LN0.1 are measured along the polar axis of the crystal for extraordinarily polarized light $\varepsilon_3\varepsilon_3^*$ at wavelength λ = 532 nm. The coefficients are given in Fig. 4.15. The values for β_{333} for Fe:LN0.03 is 1.06 ± 0.04 nAW^{-1} whereas for β_{333} for Fe:LN0.1 is 18.7 ± 0.02 nAW^{-1}. This shows that doping concentration plays a role in BPVE.

BPV component β_{333} measured for Fe:LN0.1 at different wavelengths is shown in Fig. 4.16a. Increase in the doping concentration by a factor of 3 leads to an increase of β_{333} by 17 for excitation wavelength λ = 532 nm, 3 for λ = 473 nm and by 9 for λ = 450 nm. It is observed that when the doping concentration is increased by a factor of 3, the absorption coefficient (α) increases by a factor of 9 for λ = 532 nm, by 7 for λ = 473 nm and by 7.2 for λ = 450 nm.

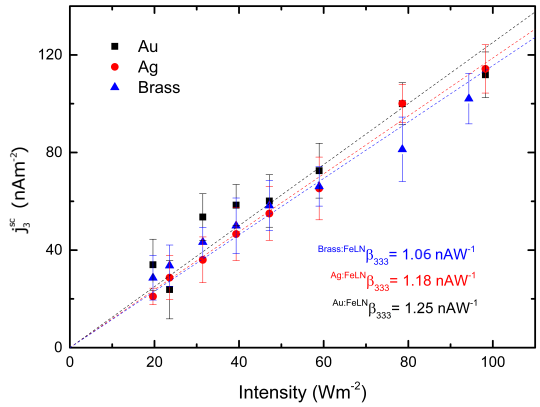

Figure 4.14: BPV measurements on Fe:LN0.03 with different metal electrodes at excitation wavelength λ= 532 nm.

Highest value of β_{333} = 27.3 nAW^{-1} for λ = 450 nm is observed for Fe:LN0.1 like in the case for Fe:LN0.03. The ratio $\zeta = \beta_{333}/\alpha$ for different wavelengths measured is given as ζ_{450nm} = 63 pAmW^{-1}, ζ_{473nm} = 19 pAmW^{-1} and ζ_{532nm} = 68 pAmW^{-1}. Different orientations of BPV components measured for Fe:LN0.1 with excitation wavelength λ = 532 nm are shown in the Fig. 4.16b follow the same trend as for Fe:LN0.03. The BPV component β_{333} as mentioned above increases by a factor of 17 for Fe:LN0.1 when compared to Fe:LN0.03, component β_{222} is increased by a factor of 15 and β_{322} by a factor 6.

The values of measurable components for Fe:LN0.1 for different wavelengths are given in table 4.5.

β_{ikl}	i	kl	450 nm	473 nm	532 nm
β_{333}	3	33	27.3 ± 0.08	8.4 ± 0.06	18.7 ± 0.02
β_{322}	3	22	2.6 ± 0.03	2.9 ± 0.02	2.52 ± 0.03
β_{222}	2	22	3.07 ± 0.02	1.86 ± 0.02	2.33 ± 0.04
β_{233}	2	33	0.44 ± 0.02	0.38 ± 0.03	0.34 ± 0.02

Table 4.5: BPV components measured for Fe:LN0.1 at different wavelengths. The values of β are given in nAW^{-1}.

All the values of BPVE components given in table 4.5 are rounded off to the second decimal. The increase in the current density and consequently the BPV coefficients with dopant concentrations can be attributed to an increase in the Fe^{2+} donor sites present in the crystal lattice. Change in the dopant concentration by a factor of 3 (from 0.03 mol% Fe to 0.1 mol% Fe in LN) reflects in the BPV coefficients. The ratio (R) of BPV components due to the change in doping concentration $R_{ikl} = \beta_{ikl}^{0.1}/\beta_{ikl}^{0.03}$ is given in the table 4.6 for different wavelengths.

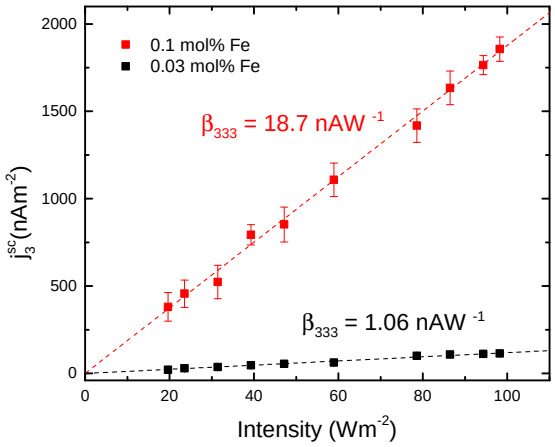

Figure 4.15: BPVE in Fe:LN0.03 in comparison to Fe:LN0.1 when short-circuit current density is measured along the polar axis at excitation wavelength λ = 532 nm.

λ (nm)	R_{333}	R_{322}	R_{222}	R_{233}	α
450	9	1.1	7	3.3	9
473	3.8	1.7	6.3	2.4	7
532	17.6	5.7	15.9	2.5	7.2

Table 4.6: Ratio of the BPV components for Fe:LN0.03 and Fe:LN0.1 at different wavelengths.

From the presented results, few observations could be concretely made:

1. β depends on λ differently for different samples.

2. BPVE coefficients measured along the polar axis increase with decrease in illumination energy. Whereas, BPVE coefficients measured perpendicular to the polar axis do not follow this trend.

3. when comparing the concentration of TM dopants in LN: α and β change differently for different samples.

However, it is necessary to evaluate the ratio of $[Fe^{2+}/Fe^{3+}]$ in the samples and the number of sites ready to become polarons to account for a much accurate understanding of the BPVE and its dependence on the doping concentrations.

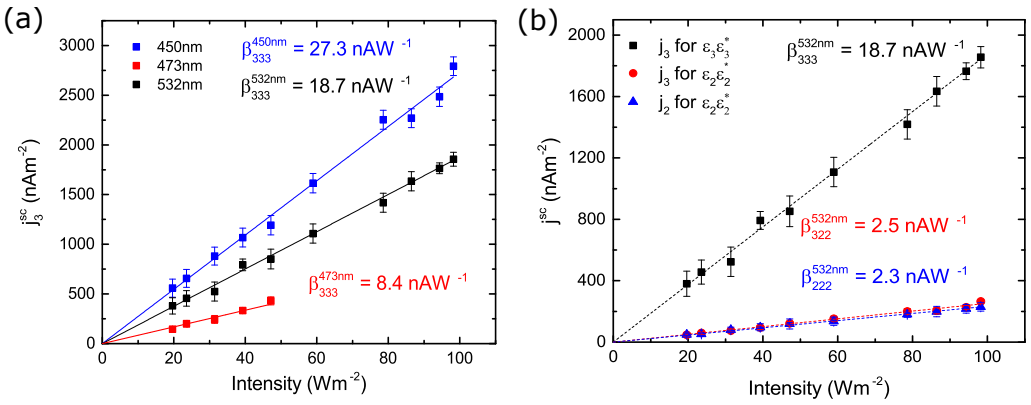

Figure 4.16: (a) BPV component β_{333} for Fe:LN0.1 for wavelengths λ = 450 nm, λ = 473 nm and λ = 532 nm (b) Short-circuit current density for different orientations in 0.1Fe:LN measured at 532 nm.

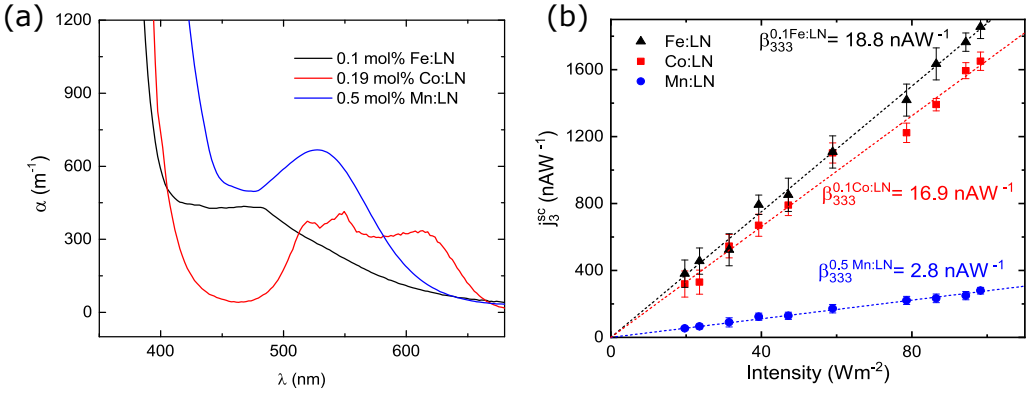

Figure 4.17: Effect of TM dopant element on BPVE (a) Shows the absorption spectra for cobalt, iron and manganese doped LN, (b) Shows measurement of short-circuit current density at increasing intensities to retrieve the component β_{333} at excitation wavelength λ= 532 nm for Co:LN, Fe:LN and Mn:LN.

Effect of transition metal dopant

To observe the effect of TM dopant element on the BPVE, short-circuit current for LN doped with 0.19 mol% cobalt (Co:LN), 0.1 mol% iron (Fe:LN) and 0.5 mol% manganese (Mn:LN) were measured at an excitation wavelength λ = 532 nm for the component β_{333}, shown in the Figure 4.17. Mn occurs in two oxidation states in LN, Mn^{3+} having the last orbital $3d^4$ and Mn^{4+} having $3d^3$. Whereas, Co occurs as Co^{2+} with $3d^7$ in the outer orbital and Co^{3+} having $3d^6$. The ratio $\zeta = \beta_{333}/\alpha$ for different dopants measured at wavelength λ = 532 nm are ζ_{532nm}^{Co} = 45 pAmW^{-1}, ζ_{532nm}^{Mn} = 4.2 pAmW^{-1} and ζ_{532nm}^{Fe} = 68 pAmW^{-1}.

The level of the TM defect centre(either shallow or deep with respect to the band gap) in the band structure, effects the photo-excitation processes which determines the value

of BPVE.

Mn and Fe ions act as deep and shallow centres respectively, because relative energy level of Mn^{2+} is deeper than that of Fe^{2+} in the forbidden gap of LN.[99] Co falls in the middle between the energy levels of Mn and Fe.

4.4 Piezo-photovoltaic measurements

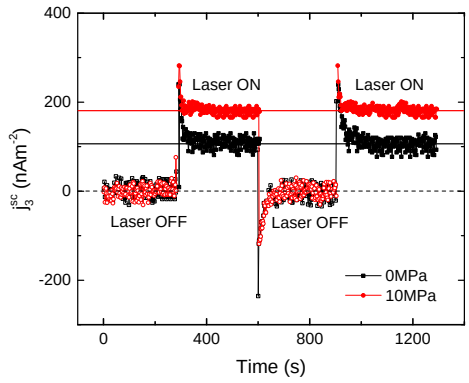

Figure 4.18: Increase in the short-circuit current for Fe:LN0.03 measured at λ = 532 nm due to uniaxial compressive stress applied along the polar axis of the crystal σ_{33}.

The effect of stress on BPVE is tested by applying uniaxial compressive stress σ_{mm}. Since the stress is uniaxial, the indices of the stress tensor σ_{mm} are σ_{33} when it is parallel to the polar c-axis and σ_{22} when the stress is applied perpendicular to the polar c-axis of the crystal. The short-circuit current density j_3 for Fe:LN0.03 as a function of time with and without illumination for the light polarization direction along the polar c-axis ($\varepsilon_3\varepsilon_3^*$), measured at wavelength 532 nm at light intensity $I = 98\ \mathrm{Wm}^{-2}$ is given in Fig. 4.18. There is an observed shift in the short-circuit current density for uniaxial compressive stress at $\sigma_{33} = 10$ MPa when compared to the current density without uniaxial compression. The measurement shows that uniaxial compressive stress notably increases the saturation value of the short-circuit current.

The value j_3^{sc} is 1.19 nAm^{-2} at zero stress. With 10 MPa uniaxial compressive stress, the value j_3^{sc} is 1.83 nAm^{-2}.

This is a visible and direct evidence that stress induces an increase in the photovoltaic current charge density in Fe:LN. 53% increase in the current density at 10 MPa uniaxial compressive stress. It is essential to determine the influence of uniaxial compressive stress on BPVE in different orientations and wavelengths, to understand the phenomenon of stress on factors that influence BPVE.

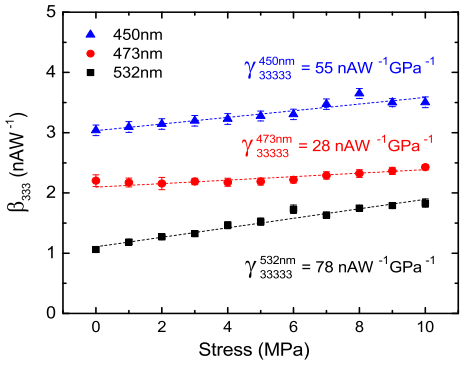

Figure 4.19: Increase in β_{333} under stress σ_{33}.

Relation between BPVE and PPVE: β_{333} values at increasing stress levels ranging from 0 MPa to 10 MPa were measured at different illumination wavelengths. Figure 4.19 shows the effect of stress on BPVE for wavelengths λ = 450 nm, 473 nm & 532 nm. A linear increase in the β_{333} values with stress for all wavelengths is observed. The y-intercept shows the value of β_{333} at zero stress and the slope represents the proportionality between the BPVE component and stress. This proportionality is termed the 'piezo-photovoltaic coefficient' represented as γ_{33333} for short-circuit current measured along the polar axis j_3 with light electric field positioned along the polar axis $\varepsilon_3\varepsilon_3^*$ and uniaxial compressive stress along the polar axis σ_{33}.

This linear relation between BPV coefficient and stress shows that stress increases BPVE as:

$$\beta_{ikl} = \gamma_{iklmn}\sigma_{mn} + \beta_{ikl}(\sigma = 0) \tag{4.1}$$

The increase in the BPV coefficients with uniaxial compressive stress is termed the piezo-photovoltaic effect (PPVE).

4.4.1 Effect of orientation and wavelength on PPVE

A schematic of all the measurable non-zero components of PPVE is shown in the Fig.4.20. The increase in the BPVE with increasing stress is measured for the components β_{333}, β_{322}, β_{233} and β_{222} under uniaxial compressive stress along σ_{33}, σ_{22}, σ_{33} and σ_{22} respectively for Fe:LN. The coefficients deduced from the measurements are shown in Fig. 4.21 for wavelengths 450 nm, 473 nm and 532 nm. A linear increase in BPVE is observed for all wavelengths and components with increase in uniaxial compressive stress. The values of the PPV coefficients with corresponding indices γ_{33333}, γ_{32233}, γ_{23322} and γ_{22222} matching the schematic presented in Fig. 4.20 are also presented.

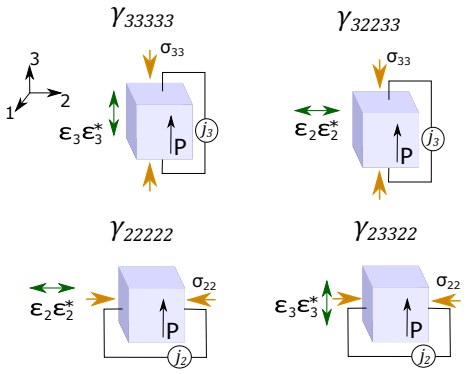

Figure 4.20: Schematic representing components of PPVE.

Influence of crystal orientation on PPVE From the values of the PPVE components shown in the Fig. 4.21, the highest values are observed for the components where the light polarisation direction is parallel to the +c axis of the crystal compared to the ones which had the light polarisation direction perpendicular to the +c axis.

Influence of wavelength on PPVE: It is observed from Fig. 4.21a, that the value for γ_{33333} for wavelength 532 nm is the highest when compared to the γ_{33333} for wavelengths 450 nm and 473 nm. The percentage increase in the BPVE at 10 MPa uniaxial stress along the polar axis of the crystal is 73% for 532 nm, 10% for 473 nm and 15% for 450 nm. The percentage increase in the BPV coefficients β_{ikl} for Fe:LN0.03 with 10 MPa uniaxial compressive stress at different wavelengths for each corresponding component σ_{mm} is given in the table 4.7.

λ (nm)	γ_{33333} %	γ_{32233} %	γ_{23322} %	γ_{22222} %
450	15	14	511	37
473	10	1	314	18
532	73	44	370	38

Table 4.7: Increase in BPV components with 10 MPa uniaxial compressive stress for Fe:LN0.03 for different wavelengths.

It is observed that the percentage increase of β_{ikl} for excitation wavelength 532 nm is highest under uniaxial compressive stress with an exception for the component β_{233} under stress σ_{22} for excitation wavelengths 450 nm.

4.4.2 Effect of dopant concentration on PPVE

Effect of dopant concentration on the piezo-photovoltaic effect is shown in the Fig. 4.22. γ_{33333} for Fe:LN0.03 is 78 $nAW^{-1}GPa^{-1}$ whereas for Fe:LN0.1 is 98 $nAW^{-1}GPa^{-1}$. Increase

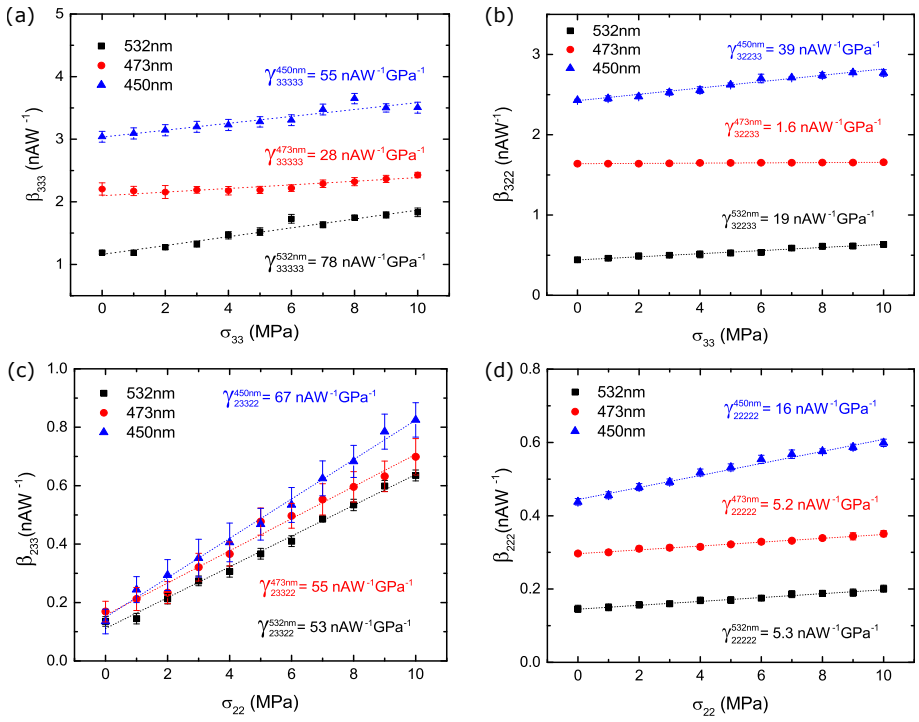

Figure 4.21: Stress modulated BPVE for Fe:LN0.03 at different wavelengths for the components β_{333}, β_{322}, β_{233} and β_{222} under uniaxial compressive stress. (a) PPVE component γ_{33333} from values of β_{333} under uniaxial compression σ_{33} (b) PPVE component γ_{32233} from values of β_{322} under uniaxial compression σ_{33} (c) PPVE component γ_{23322} from values of β_{233} under uniaxial compression σ_{22} and (d) PPVE component γ_{22222} from values of β_{222} under uniaxial compression σ_{22}.

in β_{333} for excitation wavelength λ = 532 nm under uniaxial compressive stress σ_{33} with an increase in dopant concentration by a factor of 3, results in only 25% increase in the PPV coefficients.

The PPVE in Fe:LN0.1 for all measurable orientations and excitation wavelengths λ = 450 nm, λ = 473 nm and λ = 532 nm is shown in Fig. 4.23.

The increase in β_{333} for Fe:LN0.1 measured for uniaxial compressive stress σ_{33} at excitation wavelength λ = 532 nm is higher than the components measured at other wavelengths. This deduction is similar with Fe:LN0.03 sample too. Components of PPVE for Fe:LN0.03 and Fe:LN0.1 measured at wavelengths 450 nm, 473nm and 532 nm for different light polarization directions at specific uniaxial compressive stress are summarized in the table 4.8.

The increase in the BPV coefficients for Fe:LN0.1 with 10 MPa uniaxial compressive stress at different wavelengths for each corresponding component $\beta_{ikl}\sigma_{mm}$ is given in the table 4.9.

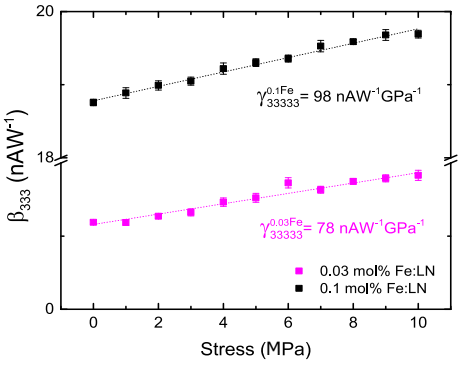

Figure 4.22: Comparison of PPVE coefficient γ_{33333} in Fe:LN0.03 and Fe:LN0.1 Fe in LN measured at wavelength λ= 532 nm.

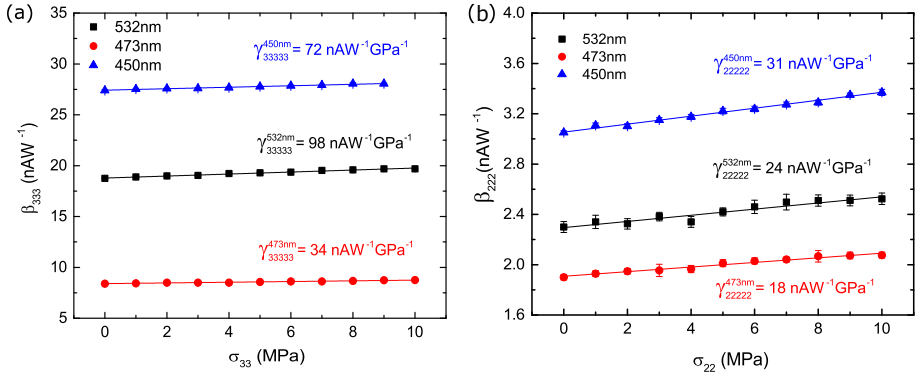

Figure 4.23: PPVE in Fe:LN0.1 at different excitation wavelengths showing (a) PPVE component γ_{33333} (b) PPVE component γ_{22222}.

The increase in the doping concentration from 0.03 to 0.1 increases the PPV coefficients approximately by a factor of 1.5 for all the components at all excitation wavelengths measured. The ratio $\xi = \gamma^{0.1}/\gamma^{0.03}$ (superscripts over γ represent the dopant concentration) at different excitation wavelengths for measured components are given in the table 4.10. The ratio $\xi_{33333}^{450nm} = 1.3$, $\xi_{33333}^{473nm} = 1.2$ and $\xi_{33333}^{532nm} = 1.3$. Similar is the case of the symmetry breaking component γ_{23322} where, $\xi_{23322}^{450nm} = 0.88$, $\xi_{23322}^{473nm} = 1.05$ and $\xi_{23322}^{532nm} = 1.4$.

4.4.3 Effect of dopant element on PPVE

Effect of uniaxial compression σ_{33} on the BPV components β_{333} for the dopant elements cobalt (Co), manganese(Mn) and iron(Fe) are shown in the Fig. 4.24 measured at excitation wavelength λ = 532 nm. The values of the PPVE for Co:LN, Mn:LN and Fe:LN are γ_{33333}^{Co} = 25 nAW^{-1}GPa^{-1}, γ_{33333}^{Mn} =10 nAW^{-1}GPa^{-1} and γ_{33333}^{Fe} = 98 nAW^{-1}GPa^{-1} respectively.

Fe conc. (mol%)	λ (nm)	γ_{33333} $nAW^{-1}GPa^{-1}$	γ_{32233} $nAW^{-1}GPa^{-1}$	γ_{23322} $nAW^{-1}GPa^{-1}$	γ_{22222} $nAW^{-1}GPa^{-1}$
0.03	450	55 ± 6.8	39 ± 1.4	67 ± 1.7	16 ± 0.6
0.03	473	28 ± 4.3	1.6 ± 0.1	55 ± 2.2	5.2 ± 0.2
0.03	532	78 ± 3.9	19 ± 0.9	52 ± 1.3	5.3 ± 0.2
0.1	450	72 ± 3.5	52 ± 2.3	59 ± 1.9	31 ± 1.1
0.1	473	34 ± 1.8	20 ± 1.4	58 ± 3.1	18 ± 0.9
0.1	532	98 ± 3.4	34 ± 1.3	73 ± 1.6	24 ± 2.4

Table 4.8: PPVE components for Fe:LN0.03 and Fe:LN0.1 measured at 450 nm, 473 nm and 532 nm for different orientations.

λ (nm)	γ_{33333} %	γ_{32233} %	γ_{23322} %	γ_{22222} %
450	2.7	20.2	164.6	9.8
473	4.1	6.9	145	11.3
532	4.8	14.7	169	8.2

Table 4.9: Increase in the BPV components under 10MPa uniaxial compressive stress for Fe:LN0.1 at different wavelengths.

4.5 Influence of phonons

4.5.1 Raman spectroscopy

A typical Raman spectrum of LN is given in Fig. 4.25 for configurations X(ZZ)$\bar{X}$ (A_1[TO]) and X(YZ)$\bar{X}$ (E[TO]). The sample was measured with a 442 nm laser and the back-scattered radiation was analysed. The radiation was polarised using two linear polarisers either parallel or perpendicular to the c-axis of the sample. Fig. 4.25 shows a clear assignment of Raman lines of LN.[100] The Raman lines recorded here are well resolved and narrow. Any deviation from the crystal structure and position of atoms should reflect in the Raman lines.

The X(ZZ)$\bar{X}$ Raman spectra shows four 1D - transverse optical modes represented as A with peaks at 252 cm^{-1}, 275 cm^{-1}, 330 cm^{-1} and 633.4 cm^{-1} which are designated as $A_1[TO_1]$, $A_1[TO_2]$, $A_1[TO_3]$ and $A_1[TO_4]$ respectively. Similarly the X(YZ)$\bar{X}$ Raman spectra shows eight 2D degenerate optical modes represented as E with peaks at 151 cm^{-1}, 237 cm^{-1}, 261 cm^{-1}, 321 cm^{-1}, 368 cm^{-1}, 432 cm^{-1}, 579 cm^{-1} and 631 cm^{-1} which are depicted as $E_1[TO_1]$, $E_1[TO_2]$, $E_1[TO_3]$, $E_1[TO_4]$, $E_1[TO_5]$, $E_1[TO_6]$, $E_1[TO_7]$ and $E_1[TO_8]$respectively.

$A_1[TO_n]$ modes represent vibrations/displacements along the polar c axis, where as the E[TO_n] modes represent vibrations/displacements orthogonal to the polar c-axis with

λ (nm)	ξ_{33333}	ξ_{32233}	ξ_{23322}	ξ_{22222}
450	1.3	1.3	0.9	1.9
473	1.2	12.5	1.1	3.5
532	1.3	1.7	1.4	4.5

Table 4.10: Increase in the PPV components due to dopant concentration of Fe in LN at different wavelengths.

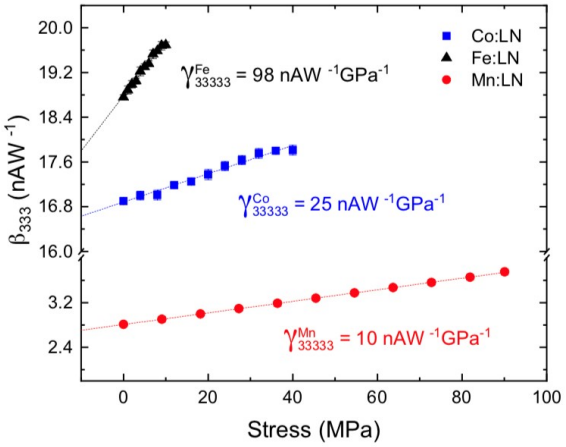

Figure 4.24: PPVE in LN doped with different elements for the component γ_{33333} measured at excitation wavelength λ = 532 nm.

alternative displacement directions of Li and Nb where the O atoms vibrate in the same direction of the Nb atoms. The vibration of the Nb-O-Nb is however a weak rocking when compared to the in-plane vibration of the Li atoms in this configuration.

Effect of external uniaxial compression on LN: The effect of uniaxial compressive stress σ_{33}, enhanced the current charge density. Raman spectroscopy is a technique which can show the influence of compressive stress on the phonon modes, with an assumption that the uniaxial compressive stress induces resistance to the inter-atomic vibrations/displacements. The effect of uniaxial compression on LN is shown in Fig. 4.26 and 4.27 for selected phonon modes.

Light induced strain in LN: The interest of looking at light induced strain with Raman spectroscopy is to detect the polarisation change attributed to photovoltaic mechanisms in Fe-doped crystals. By doping the crystal with Fe, photorefractive sensitivity is altered, which relates directly to the concentration of [Fe^{2+}]/ [Fe^{3+}].

The appearance of forbidden modes with illumination is shown in the Fig. 4.28. These are called forbidden modes because these Raman lines do not correspond to the selection

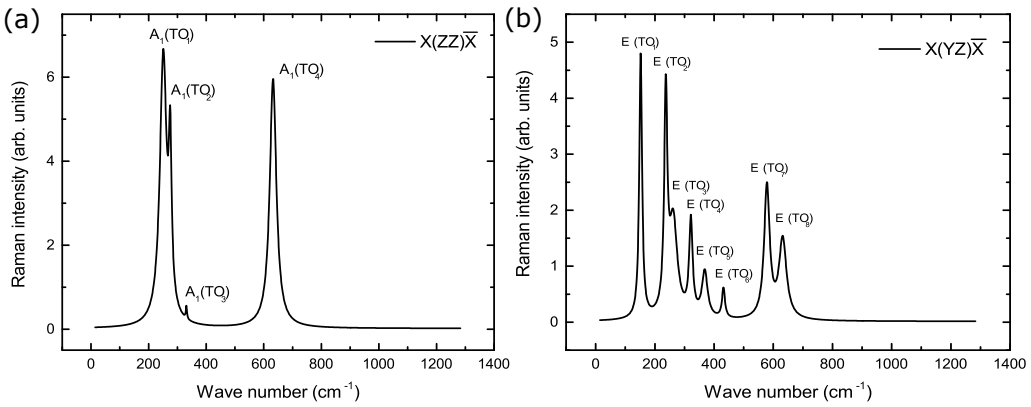

Figure 4.25: Raman spectra of Fe:LN0.03 in (a) X(ZZ)$\bar{X}$ orientation and (b) X(YZ)$\bar{X}$ orientation, recorded with incident wavelength at 442 nm showing A(TO) and E(TO) modes respectively.

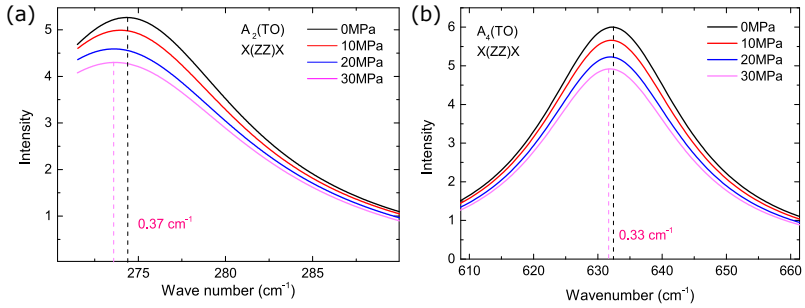

Figure 4.26: Effect of stress on the A(TO) phonon modes.

rules. Such Forbidden modes are observed when Fe:LN0.03 is illuminated with excitation wavelength 442 nm with 4 kWcm^{-2} power density, where scattering plane is perpendicular to the z-axis of the crystal.

This section should eventually describe the reason behind the appearance of forbidden lines with connection to the space charge field in Fe:LN when illuminated. These forbidden modes can be explained via two hypotheses:

1. Breaking of the selection rules due to defects.
2. Wavelength sensitivity of excited beam - photo-induced processes.

This anomaly in the (YZ) spectra in Fe:LN, is due to the activation of all four A1(TO) lines in the (YZ) spectrum, which normally exhibits E(TO)+E(LO) peaks that are completely hidden by the more intense A1 peaks. So the interpretation: the breaking of selection rules due to defects such as by Fe doping, which led to the appearance of the forbidden lines in the (YZ) spectrum, cannot be a possible explanation since it should hold true for all spectra of defect containing crystals. Also, when the same experiment is conducted by illuminating the crystal at 633 nm wavelength, Fe:LN spectra do not exhibit

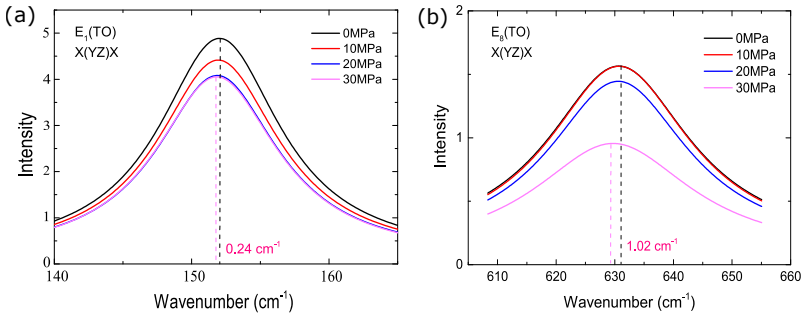

Figure 4.27: Effect of stress on the E(TO) phonon modes.

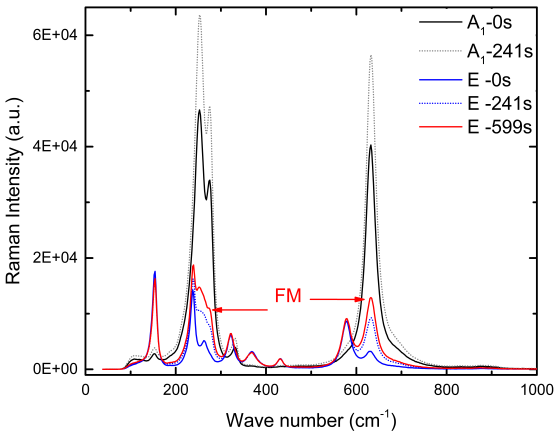

Figure 4.28: Time evolution and appearance of forbidden modes in Raman spectroscopy.

any anomaly and the Raman spectra follows the selection rules in all configurations like in the case of cLN crystals. This sensitivity over wavelength of excitation beam colluding with anomaly in the Fe:LN, possibly arise from a photo-induced process. So their origin must be related to the strong photovoltaic effects of the Fe:LN. This aspect needs to be further studied in order to obtain a better understanding of this phenomenon.

Chapter 5

Discussions on lithium niobate

5.1 Absorption and defect levels in LN

The absorption spectra of TM doped LN from Fig.4.3 and Fig.4.4 show an evident increase in absorption coefficients at light wavelength range 450 nm - 550 nm. This increase is effectuated from the TM centres. The band at 450 nm - 532 nm is attributed to the Fe^{2+}_{Li} to Nb^{5+}_{Nb} inter-valance charge transfer, and its intensity is proportional to the Fe^{2+}_{Li} concentration. In Fig.4.4 the effect of Co^{2+}_{Li} is indicated with a wide absorption around 538 nm and that of Mn^{2+}_{Li} around 516 nm. These inter-valance transfers $Co^{2+}_{Li} \rightarrow Nb^{5+}_{Nb}$, $Mn^{2+}_{Li} \rightarrow Nb^{5+}_{Nb}$ and $Fe^{2+}_{Li} \rightarrow Nb^{5+}_{Nb}$ involves a transfer of an electron from the ion to a nearest neighbour. An activation energy of E_a=0.25 eV is associated with the thermal re-trapping of this excited electron.[101]

In Fig. 4.3 a shift in the absorption edge towards longer wavelengths upon doping with Fe is observed. The shift towards longer wavelengths is greater with increasing Fe concentration which suggests a modification of a band structure of LN by the Fe impurities. Other evidences of the band-edge shift caused due to doping,[101] [102] reduction and annealing of LN,[103] [104] exist in the literature,[105] [53] however a qualitative understanding still remains unexplored.

Congruent LN has an oxygen 2pπ valence band and niobium dϵ conduction band with a band gap of 3.87 eV.[104] The observed absorption edge for Fe doped LN exhibits a broad diffusion tail, which in turn prohibits an exact determination of the band edge. Such absorption tails are referred to as "Urbach tails" which are intrinsic to ferroelectrics. Optical transitions that occur in LN, can be fitted by the equation:

$$\alpha(h\nu) \sim (h\nu - E_g)^n \tag{5.1}$$

where, α is the absorption coefficient, $h\nu$ is the photon energy, E_g is the band gap and n is the exponent determined by the nature of the electron transition during absorption

processes. The value of $n = 1/2$ is for direct band gap and $n = 2$ for indirect band gap.

By performing linear fits to the curves in $[\alpha(h\nu)]^{1/2}$ vs $h\nu$ would give indirect band gap energy. This visualisation is referred to as a Tauc plot. The intercepts of the straight fitting lines on the abscissa from the Fig. 5.1 gives the values of the optical band gap for different samples of TM: LN.

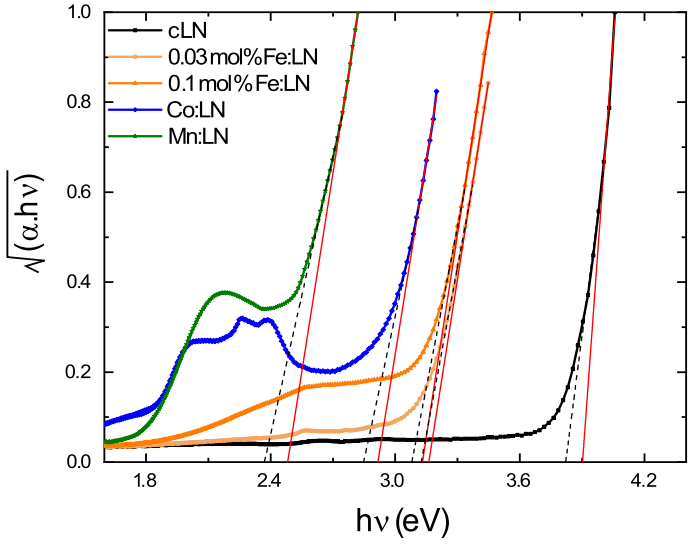

Figure 5.1: Indirect bandgap in TM:LN

In Fig. 5.1, two regions produce linear segments. These two adjoining linear segments near the band edge describe the phonon assisted fundamental absorption process corresponding to the absorption (+) or emission (-) of phonons. The red line showing a linear fit, marks the energy of the emitted phonons E_- on the energy axis, and the dashed black line gives the energy of the absorbed phonons E_+ on the energy axis. Estimated values of the indirect band gap are given in the table 5.1.

TM ion	Dopant conc.	E_g^{ind}	E_{phonons}
	mol%	*eV*	*meV*
–	0	3.87	65
Fe	0.03	3.15	48
Fe	0.1	3.11	45
Co	0.19	3.11	42
Mn	0.5	2.43	119

Table 5.1: Indirect band gap for TM defects in LN

Such calculations are notable in the optical band-gap calculations of LN. Shah *et al.* suggests that the red shift of the band edge is due to the excitation of electrons from the

oxygen 2pπ valence band to the shallow Fe_{Li}^{2+} states in the band gap.[103] This hypothesis could be verified by measuring the BPV coefficients at low wavelength regions. If the hypothesis holds viable, then photo-excitation of Fe:LN with a UV light should trigger excitation from the oxygen valence band to the Fe centre and a charge transfer to Nb_{Nb}^{5+} conduction band should not occur resulting in near zero values of the short-circuit current density. Due to an unavailability of a source in the UV range, this experiment could not be fulfilled. However, this theory suggests that Mn and Co are deeper traps when compared to a shallow Fe trap (schematically depicted in Fig.5.2). Buse et. al. confirms this statement in the study of optical excitations from Mn and Fe centres in doubly doped LN.[33]

Dhar *et al.*, Clark *et al.* and DiDominico *et al.* have suggested that the exponential increase with tailing around the low-frequency regions indicate a formation of an exciton.[53] [101] [104] It is suggested that doping LN with ions of high polarisation ability such as Fe, creates localised states in the forbidden region. Hence, the shift in the band gap could be due to the transitions from these localised states to the bands. DiDominico *et al.* show that the centres of the oxygen 2pπ and Nb dϵ bands are separated by 5 eV[104] which is close to the value calculated by Thierfelder *et al.* which is, 4.71 eV.[55] A band diagram shown in Fig.5.2 gives an idea of the d conduction orbitals. The conduction d band shown in Fig.5.2 is divided into two parts, dϵ and dγ sub bands (crystal field splitting). The band diagram is based on the electrostatic energy located at the Nb_{Nb}^{5+} inside a regular octahedron cage of oxygen ions.

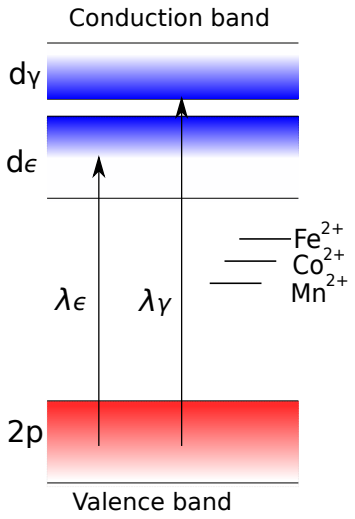

Figure 5.2: Schematic depicting splitting of the d-orbital into dϵ and dγ and probable energy levels of the impurity ions Fe, Co and Mn relative to one another. Redrawn from DiDominico Jr.M. (1969)[104] and Buse (1998)[33]

The dϵ orbitals are directed by overlapping of the oxygen ion p orbitals via the pdπ interaction. Whereas, the dγ are directed towards the oxygen ions resulting in a repulsive electrostatic interaction which positions the dγ band at a higher energetic position than

dϵ.[104]

Hence, the fundamental optical band edge observed for TM:LN due to an inter-band absorption of O pπ to Nb dϵ with a transfer of an electron between nearest neighbours. This transition is evidenced in the absorption lines tailing at the low wavelength range, resulting in a formation of an exciton.

5.2 Light induced charge transport

The wavelength dependence of BPVE coefficients, the ratios of BPVE and absorption, shows that the efficiency of photovoltaic conversion is comparable at the two longer wavelengths, which involve exclusively Fe^{2+} donor centres, but increases when band-band transitions start to become evident at shorter wavelengths.

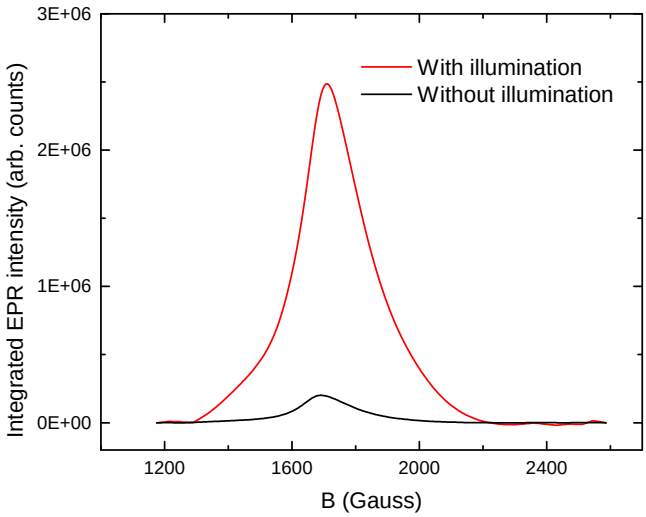

Figure 5.3: Change in the concentration of Fe^{3+} ions after photo-excitation.

The bulk photovoltaic effect in Fe:LN can be explained via the structural environment around the Fe donor defect centre and its surrounding niobium ions. The charge transport which is trigged by photo-exciting an electron from the Fe^{2+}_{Li} centres which eventually turn into traps Fe^{3+}_{Li} by transferring an electron to the Nb^{5+}_{Nb} ions were experimentally seen in the EPR spectra 4.6. The hyperfine line representing the Fe^{3+} ions[94,106] with illumination is a direct evidence of increase in the concentration of traps after photo-excitation. Since EPR spectra are conventionally displayed as a derivative of the absorption, the intensity of a signal is assessed by integration.[95] The area under the curve for these spectra gives an estimate of the increase in concentration of Fe^{3+} in the matrix, as shown in the Fig. 5.3. The concentration of Fe^{3+} ions without illumination was 5

$\times 10^7$ spins per mm^3 and under illumination the value increased to 7.3×10^8 spins per mm^3 which is an order higher. The calculated number of counts is an area linear to the amount of Fe^{3+} ions, and the presence of Fe^{2+} ions only indirectly manifests in terms of line broadening mechanism. This broad spectrum has to be integrated and baseline corrected. Owing to this procedure, the main error is due to the the base line correction. Further, when comparing two different samples, an additional error occurs owing to differences in sample position in the resonator. Hence, we need to concentrate only on the relative value increase which would reduce the above mentioned errors. So, Fe^{3+} ion concentration with illumination is increased by a factor of 14. At the same wavelength λ = 532 nm, for the same sample Fe:LN0.03, the short-circuit current density is increased by a factor of 26. This shows that the initial excitation plays a minor role in BPVE.

On the appearance of BPVE The appearance of BPVE is explained via the structural environment and the distances between the TM dopant site and the surrounding niobium sites.[1] The figure 5.4 presented in section 2.2 is repeated here for convenience.

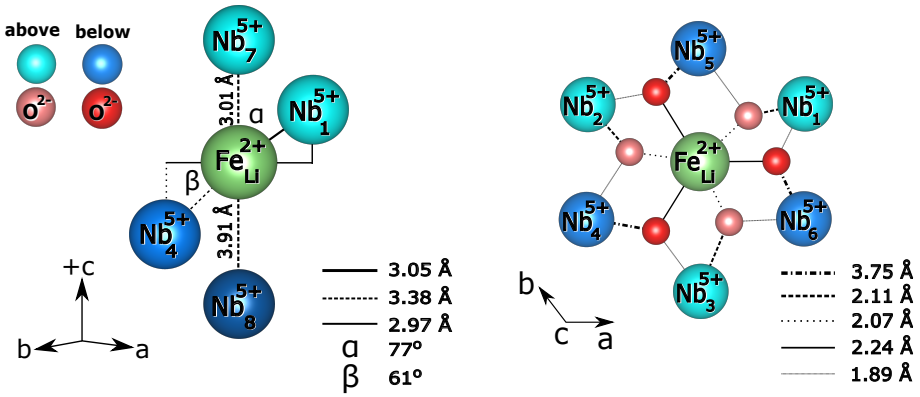

Figure 5.4: Structure of Fe:LN with interatomic distances where the arrangements of Fe^{2+}_{Li} and the neighbouring Nb^{5+}_{Nb} ions are depicted. Redrawn from Schirmer O.F (2011)[1]

The initial optical excitation, termed coherent charge transport can be explained for two cases. Case (i) where the short-circuit current is measured along the c- axis which is, $j \parallel c$ and case (ii) where the short-circuit current is measured perpendicular to the c-axis which is, $j \perp c$.

(i) Case $j \parallel c$ can be explained via inter-atomic distances elucidated in the Fig. 2.3. Optical excitation of an electron from Fe_{Li} to Nb_7 is feasible because of a shorter bond arm length $|r_7|$ = 3.01Å than the optical excitation from Fe_{Li} to Nb_8 where the bond arm length is $|r_8|$ = 3.91Å.

The current parallel to the c-axis, mentioned in the section 2.4.3, $j_z = j_+ - j_-$. Where j_+ is the current along the +ve direction of the c-axis and j_- is the current in the -ve c-axis. Here the positive and the negative directions are discussed taking Fe^{2+}_{Li} as the centre. Since the differences in the dipole changes along the negative and positive axis need to

be considered instead of their sums; (a) For extraordinarily polarised light, the sum of the dipoles along the bonds,

$$(Fe_{Li} - Nb_7) + (Fe_{Li} - Nb_1) + (Fe_{Li} - Nb_2) + (Fe_{Li} - Nb_3)$$

would dominate the dipoles along

$$(Fe_{Li} - Nb_8) + (Fe_{Li} - Nb_4) + (Fe_{Li} - Nb_5) + (Fe_{Li} - Nb_6)$$

with a positive value resulting in the highest $\beta_{333} = 3$ nAW^{-1} component. Also, the mean transport length given in the equation 2.15 would have a higher value for $j \parallel c$ case. The axial symmetry of the orbitals forming diffused coordination complexes (d_{z^2}) with the Nb_i ions are positioned along the polarization direction of the light electric field for extraordinary polarised light, which results in a higher probability of electron transfer in the specified direction.

(b) For ordinary polarised light, the value $\beta_{322} = 2.4$ nAW^{-1} is less than β_{333}. This could be explained via the orbital overlap between Fe_{Li} and neighbouring Nb_i where $i = 1, 2, 3, 4, 5, 7$ and 8 and when $j \parallel c$. The axial symmetry of the orbitals is lateral in this case, resulting in a lower value of β_{322}. The bond arms $|r_i|$, multiplied with the light electric polarization vector $\varepsilon_2\varepsilon_2^*$ would create a net field which would be less than in the case with light electric polarization vector $\varepsilon_3\varepsilon_3^*$. Hence this attributes to a less value for β_{322}.

(ii) For the case $j \perp c$, coherent charge transport phenomenon could be explained in a similar manner. The optical excitations from Fe_{Li} to Nb_i in this case, where $i = 1, 2, 3, 4, 5$ and 6 have indirect bonds with the O^{2-} ions. The bonds arm lengths for $Fe_{Li} - O^{2-} - Nb_{1,2,3}$ are projecting upward with indirect coupling via bond arm lengths 2.07 & 2.11 with the O^{2-} ions projecting above the plane and bond arm lengths 2.07 & 1.89 with the O^{2-} ions projecting below the plane. Where as, for $Fe_{Li} - O^{2-} - Nb_{4,5,6}$ the indirect coupling with O^{2-} ions projecting above the plane is 2.24 & 3.75 and to the O^{2-} ions projecting below the plane is 2.07 & 1.89. The former set of bond arm lengths would dominate the latter ones resulting in a positive value of β_{222}.

In the case of $\beta_{222} = 0.4$ nAW^{-1} the light electric field is polarized perpendicular to the polar axis of the crystal, which is ordinary polarised light. Hence the resultant value is lower than both the components β_{333} & β_{322}. According to the symmetry conditions, the component $\beta_{233} = 0$. This can be expected from the electric dipole transitions coupling with the direction of the light electric field. The difference in the dipole vectors multiplied to the light electric field $\varepsilon_3\varepsilon_3^*$ for the current measured perpendicular the polar axis j_2, cancel out each other resulting in a near zero value for the component $\beta_{233} = 0.13$ nAW^{-1}.

5.3 Piezo-Photovoltaic effect

Applying uniaxial compressive stress to Fe:LN noticeably increases the saturation value of the observed short-circuit current when the crystal is illuminated. This is the basis of

discovering the piezo-photovoltaic effect. This behaviour can be explained on the basis of a BPV charge transport model discussed in section 2.4.2 emphasizing the critical role played by polarons in LN.

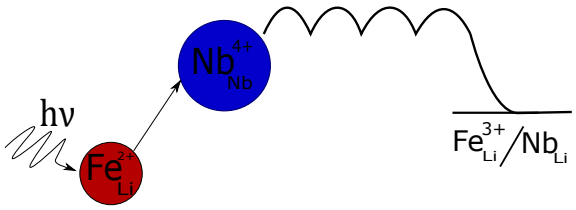

Figure 5.5: Initial optical excitations and subsequent non-thermalized and thermalized carrier motion in BPVE phenomenon.

Electrons once excited from the Fe^{2+}_{Li} to one of the preferred Nb^{5+}_{Nb} ions depending on the inter-atomic distances, before thermalization, travel in the direction of excitation by ballistic hopping, pictorially shown in the Figure 5.5. This happens within 10^{-13} s. After thermalization, the electrons form small free polarons and continue to move by thermally activated hopping until they are trapped by an Fe^{3+}_{Li} centre, which can take upto 1 s. This undirected movement does not contribute much to the charge transport. The ballistic hopping phenomenon is what contributes majorly to BPVE. BPVE arises directly from the non-centrosymmetric structure.

In order to better understand the influence and reality of piezo-photovoltaic effect, it is interesting to look at the effect of stress on a component which is theoretically equal to zero when no stress is applied. This component is β_{233}. The dependence on stress for β_{233} under uniaxial compressive stress parallel σ_{33} and perpendicular σ_{22} to the polar axis is shown in the Fig. 5.6.

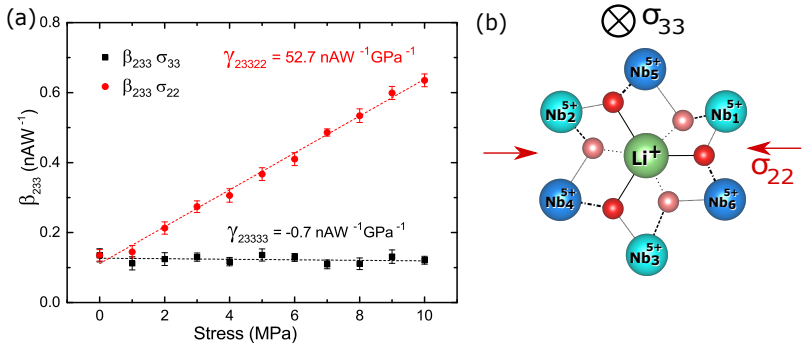

Figure 5.6: PPVE for the vanishing and non vanishing component measured at 532 nm for 0.03 mol% Fe:LN crystal.

A finite BPVE coefficient value is observed even at zero stress which is discussed before. This value increases drastically under stress σ_{22} but remains practically unchanged under stress σ_{33}. The relative increase in stress for the component β_{233} at σ_{22} = 10 MPa is 370%

which is drastic when compared to that of β_{333} under uniaxial compression σ_{33}, due to the low zero stress value. This can be explained via symmetry arrangement of ions in the lattice structure of LN, which is shown in 5.6(b). For stress parallel to the c-axis of the crystal, the system remains unchanged. However, when stress is applied perpendicular to the polar axis, it breaks the symmetry, lowering it to the monoclinic point group m, in which a non zero component β_{233} exists.

One of the possible explanations for the non-vanishing zero-stress value of β_{233} is a misalignment of the crystallographic axes with respect to the sample edges. If the crystal was misaligned, a stress σ_{33} along the polar axis should result in a non-vanishing component of the PPVE tensor γ_{23333}. But the component practically vanishes, conforming that the misalignment of the crystal is negligible. This provides as a tool to estimate the influence of interface effects on the BPVE measurements. Comparing it to the largest coefficient β_{333}, it can be estimated that 90% of the observed current is indeed due to the bulk effect.

The experiments on work-function of the electrodes and their effect on BPVE and the theory of piezo-phototronic effect are not congruent with the values observed in PPVE measurements. BPV coefficients of Fe:LN samples electroded with silver, gold and bare crystal with brass electrodes are compared. The values did not show a systematic dependence on the electrode material. If the values are effected by the metal electrode work-function, the short-circuit current should vary based on a variation in the Schottky barrier height which is not the case for LN. This concludes that PPVE is indeed an intrinsic effect.

Constructively from the observations made, and from the theory of BPVE in LN, the discussion on the appearance of PPVE can be described as follows:

Two aspects of the charge transport can be influenced by stress:

1. Initial excitation step.
2. The subsequent non-thermalized hopping, shown pictorially in Figure 5.5.

The BPVE at 10 MPa uniaxial compressive stress σ_{33} for components measured along the polar axis increases about 73% for β_{333} and by 44% for the component β_{322} for excitation wavelength λ = 532 nm. This increase can be at first be attributed to the change in interatomic distances with stress which would modify the ratio of excitation probabilities to each of the neighbouring Nb ions and/or increase in subsequent thermalized polaron hopping due to stress. Young's modulus of LN, parallel to the polar axis is 202 GPa. At 10 MPa, the deformation along the polar axis is 0.005%. This amount of macroscopic deformation plays little role in the probability of electron excitation. There is a possibility that uniaxial compressive stress reduces the macroscopic polarization consequently the asymmetry. This however, would result in a negative value of γ. Only positive values of the PPV coefficients are observed, ruling out the hypothesis that the observed effect is due to the asymmetry in photon excitation under stress. There is a possibility that

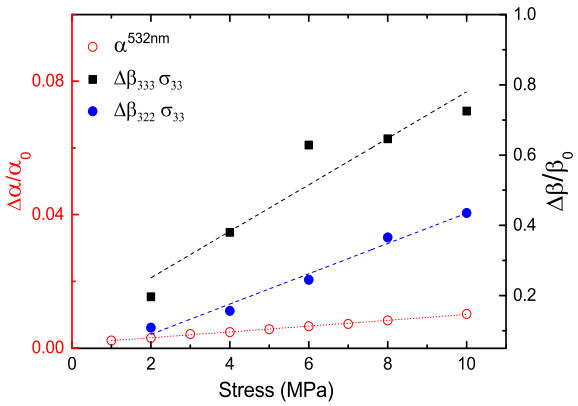

Figure 5.7: Increase in optical absorption under stress compared to β_{333} and β_{322}.

the initial excitation increases with stress. To clarify this hypothesis a comparison of the increase in absorption under stress σ_{33} with BPVE components parallel to the polar axis is given in the Fig. 5.7. It is evident that the increase in absorption under 10 MPa stress σ_{33} for λ = 532 nm is about 1%, which cannot account for the large increase in the bulk PV tensor components. Thus, the number of photo-excited charge carriers do not increase with stress. Hence, stress facilitates non-thermalized polaron hopping.

Influence of stress is direction dependent. This can be observed comparing the PPVE coefficients γ_{33333}, γ_{22222}. The increase in BPV coefficients under uniaxial compressive stress measured along the polar axis dominate the ones measured orthogonal to it. Component β_{333} under uniaxial compressive stress σ_{33} increases by 73% where as component β_{222} under uniaxial compressive stress σ_{22} increases by 38%.

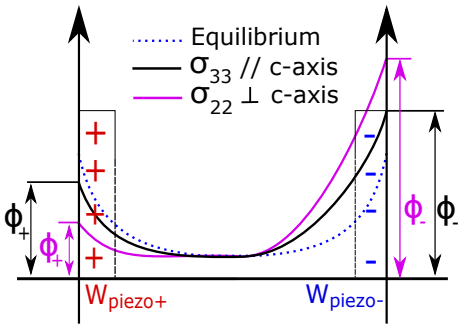

Figure 5.8: The piezotronic change in energy barriers at the metal electrodes for stress along the polar axis σ_{33} and perpendicular to the polar axis σ_{22}.

There is a possibility that the increase in BPV components with uniaxial stress, being attributed to a piezotronic or a piezo-phototronic effect, which is due to a change in the Schottky barrier at the interface between the electrode and the crystal. In the case of PPVE, the assumption that the increase in the BPV coefficients under stress is due to a piezo-phototronic effect, can be ruled out by comparing the PPVE components along

the polar axis and the ones orthogonal to it with their corresponding piezo-photovoltaic coefficients. The PPVE coefficient parallel to the z-axis γ_{33333} = 78 $nAW^{-1}GPa^{-1}$ and perpendicular to z-axis is γ_{22222} = 5 $nAW^{-1}GPa^{-1}$, corresponding piezoelectric coefficients along the polar axis are d_{333} = 6 pCN^{-1} and d_{222} = 20.8 pCN^{-1}.[25] The effect of stress for the component γ_{22222} should be more pronounced when compared to the component γ_{33333} with respect to the piezo-electric coefficients. A corresponding band diagram for stress applied along the polar axis σ_{33} and perpendicular to the polar axis σ_{22} is schematically represented in the Fig. 5.8. The energy barrier height for the component with stress applied perpendicular to the polar axis is higher than for the component with stress applied parallel to the polar axis. But the components behave contrary to this effect showing that the PPVE is indeed an intrinsic bulk phenomenon.

Doping LN causes narrowing of the band. The location of the defect level and the conduction band minimum dϵ in the band structure leads to a deduction that 532 nm light wavelength corresponds to excitations only from the defect centre whereas, the lower wavelength 450 nm corresponds to excitations from the oxygen valence band. Assuming the structural coordination of Nb and its oxygen octahedra does not influence the PPV coefficients, the values of PPV coefficient for extraordinary and ordinary polarised light for light excitation wavelength 450 nm should not differ like in the case with light excitation wavelength 532 nm, where the dipole interactions are influenced by light polarisation direction. The difference between the PPV coefficients for 0.03FeLN, γ_{33333} and γ_{32233} for excitation wavelength 450 nm is 16 $nAW^{-1}GPa^{-1}$ and the difference between PPV coefficients for 0.03FeLN, γ_{33333} and γ_{32233} for excitation wavelength 532 nm is 59 $nAW^{-1}GPa^{-1}$, which is a factor of 3 higher than the difference calculated for 450 nm. Similar comparison can be made for a higher doping concentration of iron. For 0.1FeLN, the difference between the PPV coefficients, γ_{33333} and γ_{32233} for excitation wavelength 450 nm is 20 $nAW^{-1}GPa^{-1}$ and the difference between PPV coefficients γ_{33333} and γ_{32233} for excitation wavelength 532 nm is 64 $nAW^{-1}GPa^{-1}$ which is also a factor of 3 higher than the difference calculated for 450 nm.

This can be explained by the structural environment of the centre of excitation. The oxygen octahedron surrounding Fe^{2+}_{Li} is larger than the oxygen octahedron surrounding Nb_{Nb} ion. The Nb_{Nb} ions are off centred from the centre of the oxygen octahedra by 26 - 27 pm. The asymmetry in dipole interaction and charge transfer from Fe^{2+}_{Li} to its neighbouring Nb_{Nb} is greater than the asymmetry caused due to the arrangement of the oxygen octahedra caging the Nb_{Nb} ion. The value of the PPV coefficient at 450 nm should be negative if the effect of stress is distorting the asymmetry of the Nb ions and the surrounding oxygen octahedron to a symmetric structure. However, positive values of PPV coefficients prove otherwise. Higher values of PPV coefficients for extraordinarily polarized light can be explained with the interaction and the overlap of the pdπ oxygen orbitals with the Nb_{Nb} d-orbitals under stress. DiDominico *et al.* calculated the influence of light polarisation direction on the EO coefficients (shifts in the oscillator energy in UV region termed polarisation induced Stark like energy band shifts) and have shown that the energy required to excite (in the UV region) an electron from the valence band

to the dϵ conduction band minimum is lesser for ordinary light polarization than for extraordinary light polarization direction.[104] So the increase in the BPV values in the lower wavelength 450 nm region with stress can be attributed to stress modulation of polarization induced pdπ overlap integral.

The comparison of the band narrowing caused by Fe, Co and Mn dopants and the values of BPV coefficients measured at light wavelength 532 nm show that β_{333}^{Fe} = 18.8 nAW^{-1} and β_{333}^{Co} = 16.9 nAW^{-1} have values which are closer to each other and for MnLN, β_{333}^{Mn} = 2.8 nAW^{-1}. Fig. 5.1 also shows that the shift in the indirect band for Mn is the highest whereas, the band edges for Fe and Co are closer. Hence it can be deducted that 532 nm light wavelength is exciting electrons from the dopant/defect centre in the case of FeLN and CoLN. For MnLN, band-band transitions occur at 532 nm. This deduction can be concurred with the similarity in the values of the PPV coefficients. γ_{33333}^{Fe} and γ_{33333}^{Co} are 98 nAW^{-1}GPa^{-1} and 25 nAW^{-1}GPa^{-1} respectively and that of γ_{33333}^{Mn} is 10 nAW^{-1}GPa^{-1} which can be compared to the values of PPV coefficients for FeLN measured at 532 nm (excitations from the defect centre) and those measured at 450 nm (band-band excitations).

Electromagnetic radiation frequency can couple with atomic movement involving a variation in the electric polarization of the crystal. The movements modify the dipole moment of the crystal. Any change in the atomic movements in the crystal caused due to uniaxial compression, change the dipole moment and this would reflect in the Raman lines attributed to specific vibrations or displacements of atoms in the crystal. This was observed in measurements shown in Fig. 4.26 and 4.27.

Stress induced Raman spectroscopy provides information about the shift in the phonon modes where a blue shift is observed under uniaxial compression. Hence, it is the non-thermalized polaron hoping which is effected under stress. The energy of the phonons involved in polaron formation decrease under stress, moving the polaron closer to the conduction band and increasing the hopping between neighbouring Nb-sites.

This study proves the existence of an intrinsic piezo-photovoltaic effect. It is evident from this study that moderate stress levels corresponding to 10 MPa can lead to about 75% increase in light induced current. It is the first time anyone reported the stress-dependence of BPVE.

The elastic modulus of LN is approximately 200 GPa. 10 MPa of stress corresponds to a strain level of 50 ppm. The amount of stress that can be applied on bulk samples cannot exceed a certain limit. Permanent physical damage like cracking or crushing of the samples might occur either due to inhomogeneity in the crystal of due to accumulation of dust particles on the surface on which mechanical stress is being applied. However, thin-films or ultra-thin films of non-centrosymmetric materials can achieve high stress levels. A thin non-centrosymmetric crystalline film can be applied on a substrate which has a varied symmetry, or layers of thin non-centrosymmetric crystals with varying symmetries can be stacked one over the other to reach high stress levels. It has to be

noted that PPVE cannot be extrapolated to extremely large stress levels, as this might lead to a change in the symmetry of the crystal or its phase. Before extrapolation, this phenomenon has to be theoretically studied and simulated for better understanding. The present study proves that PPVE has a positive impact on photovoltaics by increasing the charge transport significantly.

This study also provides a breakthrough in finding materials for efficient BPV charge transport. Stress modulation can indeed widen the window of materials that can be exploited for photovoltaics. For a material to exhibit PPVE, it does not need to have BPV properties. This can be proved by looking at the forbidden zero value component β_{233} which under uniaxial compressive stress σ_{22} results in a large PPV component γ_{23322}. So a material does not strictly have to be pyroelectric or ferroelectric to exhibit PPVE but any material which has non-centrosymmetric structure can be considered for efficient BPV charge transport. Also, Young *et al.* predicted that materials similar to lithium niobate which have a smaller band gap can result in higher conversion efficiencies.[107] This means the window of materials that can be exploited for BPV charge transport is not limited to wide band gap materials.

The results and conclusions from this work open doors for further investigations on topics such as, the effect of mechanical strain on carrier mobility via ab-initio calculations, the expectation of PPVE in materials with non-polaron based charge transport, the influence of high mechanical strain on BPV properties in thin film structures. It is expected that research in this direction would eventually lead to photovoltaic energy generation with efficiencies beating the Shockley-Queisser limit even at longer light wavelengths.

References

[1] OF Schirmer, M Imlau, and C Merschjann. Bulk photovoltaic effect of $LiNbO_3 : Fe$ and its small-polaron-based microscopic interpretation. *Physical Review B*, 83: 1651061–13, 2011.

[2] WO Borchardt. *Crystallography: An introduction*. Springer-Verlag, Berlin, Heidelberg, 2011.

[3] C Kittel and PM Euen. *Introduction to solid state physics*. Wiley, New York, 1976.

[4] E Hartmann and CA Taylor. *An introduction to crystal physics*. University College Cardiff Press, 1984.

[5] WD Callister and DG Rethwisch. *Materials science and engineering: An introduction*. Wiley, New York, 2005.

[6] SK Chatterjee. *Crystallography and the World of Symmetry*. Springer, Berlin, Heidelberg, 2008.

[7] RC Powell. *Symmetry, Group Theory, and the Physical Properties of Crystals*. Springer-Verlag, New York, 2010.

[8] JF Nye. *Physical properties of crystals: Their representation by tensors and matrices*. Clarendon Press, Oxford, 1985.

[9] J Kreisel, M Alexe, and PA Thomas. A photoferroelectric material is more than the sum of its parts. *Nature Materials*, 11:260, 2012.

[10] VK Wadhawan. *Introduction to Ferroic Materials*. Gordon and Breach Science Publishers, Amsterdam, 2000.

[11] VM Fridkin. *Photoferroelectrics*. Springer Verlag, Berlin, Heidelberg, New York, 1979.

[12] J Nelson. *The physics of solar cells*. World Scientific Publishing Company, London, 2003.

[13] AG Chynoweth. Surface space-charge layers in barium titanate. *Physical Review*, 102:705–714, 1956.

[14] BI Sturman, VM Fridkin, and PJ Sturman. *Photovoltaic and Photo-refractive Effects in Noncentrosymmetric Materials*. CRC Press, USA, 1992.

[15] VM Fridkin. Review of recent work on the bulk photovoltaic effect in ferro and piezoelectrics. *Ferroelectrics*, 53:169–187, 1984.

[16] G Dalba, Y Soldo, F Rocca, VM Fridkin, et al. Giant bulk photovoltaic effect under linearly polarized x-ray synchrotron radiation. *Physical Review Letters*, 74:988–991, 1995.

[17] W Ruppel, R Von Baltz, and P Wurfel. The origin of the photo-emf in ferroelectric and non-ferroelectric materials. *Ferroelectrics*, 43:109–123, 1982.

[18] VM Fridkin. Bulk photovoltaic effect in noncentrosymmetric crystals. *Crystallography Reports*, 46:654–658, 2001.

[19] VM Fridkin. The possible mechanism for the bulk photovoltaic effect and optical damage in ferroelectrics. *Applied Physics*, 13:357–359, 1977.

[20] ZL Wang. *Piezotronics and Piezo-Phototronics: Introduction of Piezotronics and Piezo-Phototronics*. Springer-Verlag, Berlin, Heidelberg, 2012.

[21] H Fujita. *Micromachines as tools for nanotechnology*. Springer-Verlag, Berlin, Heidelberg, 2003.

[22] Y Liu, Q Yang, Y Zhang, Z Yang, et al. Nanowire piezo-phototronic photodetector: Theory and experimental design. *Advanced Materials*, 24:1410–1417, 2012.

[23] BT Matthias and JP Remeika. Ferroelectricity in the ilmenite structure. *Physical Review*, 76:1886–1887, 1949.

[24] A Ashkin, CD Boyd, J M Dziedzic, RG Smith, et al. *Landmark Papers On Photorefractive Nonlinear Optics: Optically-Induced refractive index inhomogeneities in $LiNbO_3$, and $LiTaO_3$*. World Scientific, Singapore, 1995.

[25] T Volk and M Wöhlecke. *Lithium niobate: defects, photorefraction and ferroelectric switching*. Springer-Verlag, Berlin, Heidelberg, 2008.

[26] DN Nikogosyan. *Nonlinear optical crystals: A complete survey*. Springer-Verlag, New York, 2006.

[27] I Takanaga, J Hirohashi, and J Kushibiki. Homogeneity evaluation of $LiNbO_3$, and $LiTaO_3$ single crystals for determining acoustical physical constants. *Japanese Journal of Applied Physics*, 38:3201–3203, 1999.

[28] PK Gallagher, HM O'Bryan, EM Gyorgy, et al. Thermal expansion and transitions of single crystal lithium niobates from −60 to 250°C. *Ferroelectrics*, 75:71–77, 1987.

[29] M Nakamura, M Sekita, S Takekawa, and K Kitamura. Crystal growth and char-

acterization of Nd, Mg co-doped near-stoichiometric $LiNbO_3$. *Journal of Crystal Growth*, 290:144–148, 2006.

[30] K Kitamura, Y Furukawa, K Niwa, V Gopalan, et al. Crystal growth and low coercive field 180° domain switching characteristics of stoichiometric $LiTaO_3$. *Applied Physics Letters*, 73:3073–3075, 1998.

[31] SC Abrahams and P Marsh. Defect structure dependence on composition in lithium niobate. *Acta Crystallographica Section B: Structural Science*, 42:61–68, 1986.

[32] K Noguchi, O Mitomi, and H Miyazawa. Millimeter-wave Ti: $LiNbO_3$ optical modulators. *Journal of Lightwave Technology*, 16:615–619, 1998.

[33] K Buse, A Adibi, and D Psaltis. Non-volatile holographic storage in doubly doped lithium niobate crystals. *Nature*, 393:665–668, 1998.

[34] M Haw. Holographic data storage: The light fantastic. *Nature*, 422:556–558, 2003.

[35] H Kang, CX Yang, GG Mu, and ZK Wu. Real-time holographic associative memory using doped $LiNbO_3$ in a phase-conjugating resonator. *Optics Letters*, 15:637–639, 1990.

[36] MH Dunn and M Ebrahimzadeh. Parametric generation of tunable light from continuous-wave to femtosecond pulses. *Science*, 286:1513–1517, 1999.

[37] M Bayssie, JD Brownridge, N Kukhtarev, T Kukhtarev, et al. Generation of focused electron beam and x-rays by the doped $LiNbO_3$ crystals. *Nuclear Instruments and Methods in Physics Research Section B: Beam Interactions with Materials and Atoms*, 241:913–916, 2005.

[38] K Peithmann, A Wiebrock, and K Buse. Photorefractive properties of highly-doped lithium niobate crystals in the visible and near-infrared. *Applied Physics B*, 68:777–784, 1999.

[39] B Chmielak, M Waldow, C Matheisen, C Ripperda, et al. Pockels effect based fully integrated, strained silicon electro-optic modulator. *Optics Express*, 19:17212–17219, 2011.

[40] RS Jacobsen, KN Andersen, PI Borel, J Fage-Pedersen, et al. Strained silicon as a new electro-optic material. *Nature*, 441:199–202, 2006.

[41] S Fathpour. Emerging heterogeneous integrated photonic platforms on silicon. *Nanophotonics*, 4:143–164, 2015.

[42] K Holbert, S Sankaranarayanan, S McCready, D Spearing, et al. *Response of piezoelectric acoustic emission sensors to gamma radiation.* ESA Special Publication, 2004.

[43] P Ganguly, JC Biswas, SK Lahiri, ML Nandagoshami, et al. Effects of gamma irradiation on erbium indiffused lithium niobate substrate. *Journal of Optics*, 34: 145–152, 2005.

[44] AL Bajor, SM Kaczmarek, I Pracka, M Swirkowicz, et al. *International Conference on Solid State Crystals 2000: Growth, Characterization, and Applications of Single Crystals: Investigation of thermal annealing by gamma irradiation at room temperature in $LiNbO_3$ crystals*. International Society for Optics and Photonics, 2001.

[45] N Iyi, K Kitamura, F Izumi, JK Yamamoto, et al. Comparative study of defect structures in lithium niobate with different compositions. *Journal of Solid State Chemistry*, 101:340–352, 1992.

[46] AP Wilkinson, AK Cheetham, and RH Jarman. The defect structure of congruently melting lithium niobate. *Journal of Applied Physics*, 74:3080–3083, 1993.

[47] N Zotov, H Boysen, F Frey, Th Metzger, et al. Cation substitution models of congruent $LiNbO_3$ investigated by x-ray and neutron powder diffraction. *Journal of Physics and Chemistry of Solids*, 55:145–152, 1994.

[48] K Buse. Light-induced charge transport processes in photorefractive crystals I: Models and experimental methods. *Applied Physics B: Lasers and Optics*, 64:273–291, 1997.

[49] DJ Epstein, A Linz, and HP Jenssen. Photovoltaic effect in ferroelectric ceramics. *Technical Report NASA*, 1982.

[50] G Malovichko, V Grachev, and OF Schirmer. Interrelation of intrinsic and extrinsic defects - congruent, stoichiometric, and regularly ordered lithium niobate. *Applied Physics B: Lasers and Optics*, 68:785–793, 1999.

[51] OF Schirmer, O Thiemann, and M Wöhlecke. Defects in $LiNbO_3$–I: Experimental aspects. *Journal of Physics and Chemistry of Solids*, 52:185–200, 1991.

[52] RD Shannon. Revised effective ionic radii and systematic studies of interatomic distances in halides and chalcogenides. *Acta Crystallographica section A: crystal physics, diffraction, theoretical and general crystallography*, 32:751–767, 1976.

[53] A Dhar and A Mansingh. Optical properties of reduced lithium niobate single crystals. *Journal of Applied Physics*, 68:5804–5809, 1990.

[54] WG Schmidt, M Albrecht, S Wippermann, S Blankenburg, et al. $LiNbO_3$ ground- and excited-state properties from first-principles calculations. *Physical Review B*, 77:0351061–6, 2008.

[55] C Thierfelder, S Sanna, A Schindlmayr, and WG Schmidt. Do we know the band gap of lithium niobate? *physica status solidi (c)*, 7:362–365, 2010.

[56] Y Noguchi, R Inoue, and M Miyayama. Electronic origin of defect states in Fe-doped $LiNbO_3$ ferroelectrics. *Advances in Condensed Matter Physics*, 2016:1–10, 2016.

[57] SC Abrahams, JM Reddy, and JL Bernstein. Ferroelectric lithium niobate. Single crystal X-ray diffraction study at $24°C$. *Journal of Physics and Chemistry of Solids*, 27:997–1012, 1966.

[58] AP Levanyuk, AR Pogosyan, EM Uyukin, and NZ Sarkisyan. Photogalvanomagnetic phenomena in dielectric crystals. *Ferroelectrics*, 56:129–132, 1984.

[59] J Devreeese. *Nato Science Series B: Linear and Nonlinear Electron Transport in Solids*. Springer, US, 1976.

[60] OF Schirmer, M Imlau, C Merschjann, and B Schoke. Electron small polarons and bipolarons in $LiNbO_3$. *Journal of Physics: Condensed Matter*, 21:123201(1–29), 2009.

[61] A Goetzberger and C Hebling. Photovoltaic materials, past, present, future. *Solar energy materials and solar cells*, 62:1–19, 2000.

[62] Y Yuan, Z Xiao, B Yang, and J Huang. Arising applications of ferroelectric materials in photovoltaic devices. *Journal of Materials Chemistry A*, 2:6027–6041, 2014.

[63] NS Lewis. Toward cost-effective solar energy use. *Science*, 315:798–801, 2007.

[64] T Trupke, A Shalav, BS Richards, P Würfel, et al. Efficiency enhancement of solar cells by luminescent up-conversion of sunlight. *Solar energy materials and solar cells*, 90:3327–3338, 2006.

[65] MA Green. Thin-film solar cells: Review of materials, technologies and commercial status. *Journal of Materials Science: Materials in Electronics*, 18:15–19, 2007.

[66] A Shah, P Torres, R Tscharner, N Wyrsch, et al. Photovoltaic technology: The case for thin-film solar cells. *Science*, 285:692–698, 1999.

[67] BJ O'Sullivan, T Bearda, S Nadupalli, R Labie, et al. Process-induced degradation of SiO_2 and a-Si:H passivation layers for photovoltaic applications. *IEEE Journal of Photovoltaics*, 4:1197–1203, 2014.

[68] X Mathew, JP Enriquez, A Romeo, and AN Tiwari. $CdTe/CdS$ solar cells on flexible substrates. *Solar energy*, 77:831–838, 2004.

[69] SG Kumar and KSRK Rao. Physics and chemistry of $CdTe/CdS$ thin film heterojunction photovoltaic devices: fundamental and critical aspects. *Energy & Environmental Science*, 7:45–102, 2014.

[70] M Afzaal and P O'Brien. Recent developments in II–VI and III–VI semiconductors and their applications in solar cells. *Journal of Materials Chemistry*, 16:1597–1602, 2006.

[71] P Jackson, D Hariskos, R Wuerz, O Kiowski, et al. Properties of $Cu(In, Ga)Se_2$ solar cells with new record efficiencies up to 21.7%. *physica status solidi (RRL)-Rapid Research Letters*, 9:28–31, 2015.

[72] M Yoshimi, T Sasaki, T Sawada, T Suezaki, et al. *High efficiency thin film silicon hybrid solar cell module on 1 m/sup 2/-class large area substrate: Proceedings of 3rd world conference on Photovoltaic energy conversion*. IEEE, 2003.

[73] MA Jalaja and S Dutta. Ferroelectrics and multiferroics for next generation photovoltaics. *Advanced Materials Letter*, 6:568–584, 2015.

[74] GA Chamberlain. Organic solar cells: A review. *Solar cells*, 8:47–83, 1983.

[75] R Pode. On the problem of open circuit voltage in metal phthalocyanine/C_{60} organic solar cells. *Advanced Materials Letters*, 2:3–11, 2011.

[76] PV Kamat. Quantum dot solar cells: Semiconductor nanocrystals as light harvesters. *The Journal of Physical Chemistry C*, 112:18737–18753, 2008.

[77] A Mathew, G M Rao, and N Munichandraiah. Towards fabrication of stable dye sensitized solar cells based on acetonitrile as solvent for the redox couple. *Advanced Materials Letter*, 5:180–183, 2014.

[78] S Rühle, M Shalom, and A Zaban. Quantum-dot-sensitized solar cells. *ChemPhysChem*, 11:2290–2304, 2010.

[79] NG Park. Perovskite solar cells: An emerging photovoltaic technology. *Materials Today*, 18:65–72, 2015.

[80] H Hoppe and NS Sariciftci. Organic solar cells: An overview. *Journal of Materials Research*, 19:1924–1945, 2004.

[81] FS Chen. Optically induced change of refractive indices in $LiNbO_3$ and $LiTaO_3$. *Journal of Applied Physics*, 40:3389–3396, 1969.

[82] DVD Linde, AM Glass, and KF Rodgers. Multiphoton photorefractive processes for optical storage in $LiNbO_3$. *Applied Physics Letters*, 25:155–157, 1974.

[83] VM Fridkin and BN Popov. Anomalous photovoltaic effect in ferroelectrics. *Soviet Physics Uspekhi*, 21:981–991, 1978.

[84] SY Yang, J Seidel, SJ Byrnes, P Shafer, et al. Above-bandgap voltages from ferroelectric photovoltaic devices. *Nature Nanotechnology*, 5:143–147, 2010.

[85] K Tonooka, P Poosanaas, and K Uchino. *Smart Structures and Materials 1998: Smart Materials Technologies: Mechanism of the bulk photovoltaic effect of ferroelectrics*. International Society for Optics and Photonics, 1998.

[86] I Grinberg, DV West, M Torres, G Gou, et al. Perovskite oxides for visible-light-absorbing ferroelectric and photovoltaic materials. *Nature*, 503:509–512, 2013.

[87] MM Furchi, A Pospischil, F Libisch, J Burgdorfer, et al. Photovoltaic effect in an electrically tunable van der Waals heterojunction. *Nano Letters*, 14:4785–4791, 2014.

[88] A Bhatnagar, A R Chaudhuri, Y H Kim, D Hesse, et al. Role of domain walls in the abnormal photovoltaic effect in $BiFeO_3$. *Nature Communications*, 4:2835(1–8), 2013.

[89] SY Yang, LW Martin, SJ Byrnes, TE Conry, et al. Photovoltaic effects in $BiFeO_3$. *Applied Physics Letters*, 95:062909(1–3), 2009.

[90] M Alexe and D Hesse. Tip-enhanced photovoltaic effects in bismuth ferrite. *Nature Communications*, 2:256(1–5), 2011.

[91] GR Eaton, SS Eaton, DP Barr, and RT Weber. *Quantitative EPR*. Springer-Verlag, Wien, 2010.

[92] MC Weber. Electronic and structural properties of bismuth and rare earth ferrites. *Thesis – University of Luxembourg*, page 153, 2016.

[93] E Sapper, R Dittmer, D Damjanovic, E Erdem, et al. Aging in the relaxor and ferroelectric state of Fe-doped $(1-x)(Bi_{1/2}Na_{1/2})TiO_3 - xBaTiO_3$ piezoelectric ceramics. *Journal of Applied Physics*, 116:104102(1–12), 2014.

[94] TH Yeom, SH Lee, SH Choh, and D Choi. Electron paramagnetic resonance study of Fe^{3+} in $LiNbO_3 : Mg : Fe$ crystal. *Journal of the Korean Physical Society*, 32: S647–S649, 1998.

[95] MD Drahus, P Jakes, E Erdem, and RA Eichel. Defect structure of the mixed ionic–electronic conducting $Sr[Ti, Fe]O_x$ solid-solution system—change in iron oxidation states and defect complexation. *Solid State Ionics*, 184:47–51, 2011.

[96] M Loyo-Menoyo, DJ Keeble, Y Furukawa, and K Kitamura. Electron paramagnetic resonance of Fe^{3+} in $LiNbO_3$. *Physical Review B*, 71:9047–9057, 2005.

[97] RC Santana, MC Terrile, AC Hernandes, MRB Andreeta, et al. Electron spin resonance study of Fe^{3+} in $LiNbO_3$ single crystals: Bulk and fibres. *Solid State Communications*, 103:61–64, 1997.

[98] T Gebre, AK Batra, P Guggilla, MD Aggarwal, et al. Pyroelectric properties of pure and doped lithium niobate crystals for infrared sensors. *Ferroelectric Letters*, 31:131–139, 2004.

[99] L Hesselink, SS Orlov, A Liu, A Akella, et al. Photorefractive materials for nonvolatile volume holographic data storage. *Science*, 282:1089–1094, 1998.

[100] R Mouras, MD Fontana, M Mostefa, and P Bourson. Photorefractive properties probed by Raman spectroscopy in Fe-doped $LiNbO_3$. *Journal of the Optical Society of America B*, 23:1867–1871, 2006.

[101] MG Clark, FJ DiSalvo, AM Glass, and GE Peterson. Electronic structure and optical index damage of iron-doped lithium niobate. *The Journal of chemical physics*, 59: 6209–6219, 1973.

[102] NN Sirota and WP Yarunichev. On absorption spectra temperature dependence in lithium niobate doped with transition metal oxides. *Kristall und Technik*, 12: 411–416, 1977.

[103] RR Shah, DM Kim, TA Rabson, and FK Tittel. Characterization of iron-doped lithium niobate for holographic storage applications. *Journal of Applied Physics*, 47:5421–5431, 1976.

[104] M DiDomenico Jr and SH Wemple. Oxygen-octahedra ferroelectrics. (i) theory of electro-optical and nonlinear optical effects. *Journal of Applied Physics*, 40:720–734, 1969.

[105] YY Li, HL Chen, GJ Chen, CL Kuo, et al. Investigation of the defect structure of congruent and fe-doped $LiNbO_3$ powders synthesized by the combustion method. *Materials*, 10(4):380, 2017.

[106] GI Malovichko, VG Grachev, OF Schirmer, and B Faust. New axial Fe^{3+} centres in stoichiometric lithium niobate crystals. *Journal of Physics: Condensed Matter*, 5: 3971–3976, 1993.

[107] SM Young, F Zheng, and AM Rappe. First-principles materials design of high-performing bulk photovoltaics with the $LiNbO_3$ structure. *Physical Review Applied*, 4:054004(1–7), 2015.

[108] K Buse. Light-induced charge transport processes in photorefractive crystals II: Materials. *Applied Physics B*, 64:391–407, 1997.

[109] MI Aroyo, JM Perez Mato, C Capillas, E Kroumova, et al. Bilbao crystallographic server I: Databases and crystallographic computing programs. *Zeitschrift für Kristallographie*, 221:15–27, 2006.

Appendix A

Representation of tensors in matrix method

In anisotropic substances, often properties depend on symmetry or the structure of the material. Hence it is efficient to determine the properties with the help of vectors or tensors.

For example, if E denotes the strength of an electric field at a point. The magnitude and direction of the electric field over this point can be denoted by a vector with projections on three mutually perpendicular axes. They can be determined by components which are projections of vectors on these axes.

So if components of E are E_1, E_2 and E_3,

$$E = \begin{bmatrix} E_1 & E_2 & E_3 \end{bmatrix}$$

When the axis of reference has been chosen, the vector is specified by the values of the components along the axes, which is also a tensor of a first rank.

If an electric field E given by a vector acts on a conductor, an electric current flows. The current density is denoted by the vector j.

If the conductor is isotropic, it obeys ohm's law and $j//E$,

$$j = \sigma E \tag{A.1}$$

where, σ is the conductivity.

According to the vector notation and the reference axes,

$$j = \begin{bmatrix} j_1 & j_2 & j_3 \end{bmatrix}$$

and

$$E = \begin{bmatrix} E_1 & E_2 & E_3 \end{bmatrix}$$

,

it follows that $j_1 = \sigma E_1$, $j_2 = \sigma E_2$ *and* $j_3 = \sigma E_3$.

Now, if the conductor is a crystal, in an isotropic media, the relation between the components of j and E are replaced by:

$$\begin{aligned} j_1 &= \sigma_{11}E_1 + \sigma_{12}E_2 + \sigma_{13}E_3 \\ j_2 &= \sigma_{21}E_1 + \sigma_{22}E_2 + \sigma_{23}E_3 \\ j_3 &= \sigma_{31}E_1 + \sigma_{32}E_2 + \sigma_{33}E_3 \end{aligned} \tag{A.2}$$

Where σ_{11}, σ_{12},..... are constants. Due to the anisotropy, j is no longer in the same direction as E.

In order to specify the conductivity of a crystal, we have to specify the nine coefficients, which can be written as,

$$\begin{bmatrix} \sigma_{11} & \sigma_{12} & \sigma_{13} \\ \sigma_{21} & \sigma_{22} & \sigma_{23} \\ \sigma_{31} & \sigma_{32} & \sigma_{33} \end{bmatrix}$$

This array enclosed by square brackets is called the tensor of a second rank.

A.1 Transformation of tensors

In the section above, conductivity is taken as an example. Two properties of a crystal which are related to each other can be shown in the form of a tensor. It is convenient to shorten the the notation. Lets assume properties p and q are related to each other with the tensor T in a similar manner like the one shown in A.2, then the second rank tensor would be:

$$\begin{bmatrix} T_{11} & T_{12} & T_{13} \\ T_{21} & T_{22} & T_{23} \\ T_{31} & T_{32} & T_{33} \end{bmatrix}$$

$$\begin{aligned} p_1 &= \sum_{j=1}^{3} T_{1j} q_j \\ p_2 &= \sum_{j=1}^{3} T_{2j} q_j \\ p_3 &= \sum_{j=1}^{3} T_{3j} q_j \end{aligned} \tag{A.3}$$

Which can also be written as,

$$p_i = \sum_{j=1}^{3} T_{ij} q_j \ \ (i = 1, 2, 3) \tag{A.4}$$

which is,

$$p_i = T_{ij} q_j \ \ (i, j = 1, 2, 3) \tag{A.5}$$

In equation A.4, the coefficients of the tensor are given with respect to a particular axes which is mutually orthogonal to each other. However, if in a different axes, the vector projections and consequently the tensor components would also change.

To understand how the values of the nine components T_{ij} transform when the axes is changed, the components of the transformed vector values of p_i and q_i need to be considered.

Vector p whose components with respect to x_1, x_2, x_3 are p_1, p_2, p_3 and the components with respect to the new axes $x_1^{'}, x_2^{'}, x_3^{'}$ are $p_1^{'}, p_2^{'}, p_3^{'}$, The component $p_1^{'}$ is obtained by resolving p_1, p_2, p_3 along the new direction $x_1^{'}$.

$$p_1^{'} = p_1 cos\widehat{x_1 x_1^{'}} + p_2 cos\widehat{x_2 x_2^{'}} + p_2 cos\widehat{x_3 x_3^{'}} \tag{A.6}$$

So, the transformed tensor can be written as,

$$p_i^{'} = a_{ij} p_j \tag{A.7}$$

Similarly, if the second-rank tensors shown in equation (A.5), needs to be transformed with regards to the new set of axes $x_1^{'}, x_2^{'}, x_3^{'}$ the vectors p and q have new components $p_i^{'}$ and $q_i^{'}$

The relation between $p^{'}$ and $q^{'}$ is given below:

$$p^{'} \longrightarrow p \longrightarrow q \longrightarrow q^{'} \tag{A.8}$$

$$p_i^{'} = a_{ik} p_k \tag{A.9}$$

$$p_i = T_{il} q_l \tag{A.10}$$

$$q_l = a_{jl} q_j^{'} \tag{A.11}$$

Combining equations (A.9), (A.10) and (A.11),

$$p_i^{'} = a_{ik} a_{jl} T_{kl} q_j^{'} = T_{ij}^{'} q_j^{'} \tag{A.12}$$

The transformed tensor is given by:

$$T_{ij}^{'} = a_{ik} a_{jl} T_{kl} \tag{A.13}$$

Similarly, for the third-rank tensor,

$$T_{ijk}^{'} = a_{il} a_{jm} a_{kn} T_{lmn} \tag{A.14}$$

and for a fifth-rank tensor,

$$T_{ijklm}^{'} = a_{in} a_{jo} a_{kp} a_{lq} a_{mr} T_{nopqr} \tag{A.15}$$

Appendix B

Symmetry representation

Each point group symmetry representing the structure/arrangement of atoms in the crystal can be written in the form of a 3×3 matrix. For $LiNbO_3$ which belongs to 3m point group, below is the symmetry matrix which is required to deduce the zero and non-zero components of a n^{th} rank tensor.

Independent, dependent and non-zero components for a third-rank tensor (components representing BPVE tensor) are given in the table B.2. For the BPV tensor component, β_{123} the subscripts or the indices 1,2 and 3 are analogous to x,y and z respectively. Henceforth the indices 1,2 and 3 are used to expedite understanding of direction in measurement and determination of components.

No.	Symmetry function	Matrix representation
1	An identity or a 360° rotation	$\begin{bmatrix} 1 & 0 & 0 \\ 0 & 1 & 0 \\ 0 & 0 & 1 \end{bmatrix}$
2	A 120° rotation	$\begin{bmatrix} -\frac{1}{2} & \frac{\sqrt{3}}{2} & 0 \\ -\frac{\sqrt{3}}{2} & -\frac{1}{2} & 0 \\ 0 & 0 & 1 \end{bmatrix}$
3	A 240° rotation	$\begin{bmatrix} -\frac{1}{2} & -\frac{\sqrt{3}}{2} & 0 \\ \frac{\sqrt{3}}{2} & -\frac{1}{2} & 0 \\ 0 & 0 & 1 \end{bmatrix}$
3	A reflection of Identity along yz plane	$\begin{bmatrix} -1 & 0 & 0 \\ 0 & 1 & 0 \\ 0 & 0 & 1 \end{bmatrix}$
4	A reflection of 120° rotation along yz plane	$\begin{bmatrix} \frac{1}{2} & \frac{\sqrt{3}}{2} & 0 \\ \frac{\sqrt{3}}{2} & -\frac{1}{2} & 0 \\ 0 & 0 & 1 \end{bmatrix}$
5	A reflection of 240° rotation along yz plane	$\begin{bmatrix} \frac{1}{2} & -\frac{\sqrt{3}}{2} & 0 \\ -\frac{\sqrt{3}}{2} & -\frac{1}{2} & 0 \\ 0 & 0 & 1 \end{bmatrix}$

Table B.1: Symmetry tensors for point group 3m.

BPVE tensor components		
No.	Component	Property
1	β_{111}	0
2	β_{112}	$-\beta_{222}$
3	β_{113}	β_{223}
4	β_{121}	$-\beta_{222}$
5	β_{122}	0
6	β_{123}	0
7	β_{131}	β_{232}
8	β_{132}	0
9	β_{133}	0
10	β_{211}	$-\beta_{222}$
11	β_{212}	0
12	β_{213}	0
13	β_{221}	0
14	β_{222}	independent
15	β_{223}	independent
16	β_{231}	0
17	β_{232}	independent
18	β_{233}	0
19	β_{311}	β_{322}
20	β_{312}	0
21	β_{313}	0
22	β_{321}	0
23	β_{322}	independent
24	β_{323}	0
25	β_{331}	0
26	β_{332}	0
27	β_{333}	independent

Table B.2: Bulk photovoltaic tensor components for R3c symmetry.